Signal Processing Algorithms for MIMO Radar

Thesis by

Chun-Yang Chen

In Partial Fulfillment of the Requirements

for the Degree of

Doctor of Philosophy

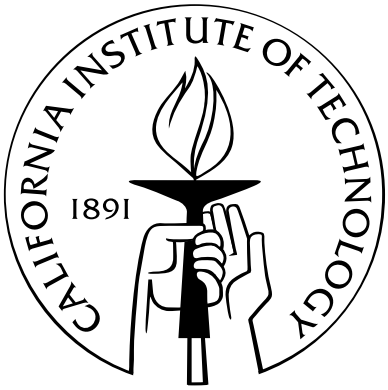

California Institute of Technology

Pasadena, California

2009

(Defended June 5, 2009)

Acknowledgments

First of all, I would like to thank my advisor, Professor P. P. Vaidyanathan, for his excellent guidance and support during my stay in Caltech. He has taught me everything I need to be a great researcher including being creative, thinking deeply, and the skills for presenting ideas and writing papers. He is also a perfect gentleman who is always nice, polite, and considerate. He is a perfect role model and I have learned so much from him.

I also like to thank the members of my defense and candidacy committees: Professor Abu-Mostafa, Professor Babak Hassibi, Professor Ho, Dr. Tkacenko , and Dr. van Zyl. I would also like to thank the National Science Foundation (NSF), and the Office of Naval Research (ONR) for their generous financial support during my graduate studies at Caltech.

I also like to thank my labmates Professor Byung-Jun Yoon, Dr. Borching Su, Ching-Chih Weng, Piya Pal, and Chih-Hao Liu. It was truly a great experience working with these smart people. I will deeply miss our discussions and conversations as well as the many conference trips that we made together. I also would like to thank Andrea Boyle, our wonderful secretary, for her kind assistance and professional support.

Also, I would like to thank my parents, Tien-Mu Chen and Shu-Fen Yang, for their love and support for my entire life. I also want to thank my brother Chun-Goo Chen for taking care of my parents for me in Taiwan. I would like to give a special thanks to my lovely wife Chia-Wen Chang for her accompany and love.

Last but not least, I would like to thank God, for creating this beautiful universe and giving me this wonderful life.

Abstract

Radar is a system that uses electromagnetic waves to detect, locate and measure the speed of reflecting objects such as aircraft, ships, spacecraft, vehicles, people, weather formations, and terrain. It transmits the electromagnetic waves into space and receives the echo signal reflected from objects. By applying signal processing algorithms on the reflected waveform, the reflecting objects can be detected. Furthermore, the location and the speed of the objects can also be estimated. Radar was originally an acronym for "RAdio Detection And Ranging". Today radar has become a standard English noun. Early radar development was mostly driven by military and military is still the dominant user and developer of radar technology. Military applications include surveillance, navigation, and weapon guidance. However, radar now has a broader range of applications including meteorological detection of precipitation, measuring ocean surface waves, air traffic control, police detection of speeding traffic, sports radar speed guns, and preventing car or ship collisions.

Recently, the concept of MIMO radar has been proposed. The MIMO radar is a multiple antenna radar system which is capable of transmitting arbitrary waveform from each antenna element. In the traditional phased array radar, the transmitting antennas are limited to transmit scaled versions of the same waveform. However the MIMO radar allows the multiple antennas to transmit arbitrary waveforms. Like MIMO communications, MIMO radar offers a new paradigm for signal processing research. MIMO radar possesses significant potentials for fading mitigation, resolution enhancement, and interference and jamming suppression. Fully exploiting these potentials can result in significantly improved target detection, parameter estimation, target tracking and recognition performance. The MIMO radar technology has rapidly drawn considerable attention from many researchers. Several advantages of MIMO radar have been discovered by many different researchers such as increased diversity of the target information, excellent interference rejection capability, improved parameter identifiability, and enhanced flexibility for transmit beampattern design. The degrees of freedom introduced by MIMO radar improves the performance of the radar

systems in many different aspects. However, it also generates some issues. It increases the number of dimensions of the received signals. Consequently, this increases the complexity of the receiver. Furthermore, the MIMO radar transmits an incoherent waveform on each of the transmitting antennas. This in general reduces the processing gain compared to the phased array radar. The multiple arbitrary waveforms also affects the range and Doppler resolution of the radar system.

The main contribution of this thesis is to study the signal processing issues in MIMO radar and propose novel algorithms for improving the MIMO radar system. In the first part of this thesis, we focus on the MIMO radar receiver algorithms. We first study the robustness of the beamformer used in MIMO radar receiver. It is known that the adaptive beamformer is very sensitive to the DOA (direction-of-arrival) mismatch. In MIMO radar, the aperture of the virtual array can be much larger than the physical receiving array in the SIMO radar. This makes the performance of the beamformer more sensitive to the DOA errors in the MIMO radar case. In this thesis, we propose an adaptive beamformer that is robust against the DOA mismatch. This method imposes constraints such that the magnitude responses of two angles exceed unity. Then a diagonal loading method is used to force the magnitude responses at the arrival angles between these two angles to exceed unity. Therefore the proposed method can always force the gains at a desired interval of angles to exceed a constant level while suppressing the interferences and noise. A closed form solution to the proposed minimization problem is introduced, and the diagonal loading factor can be computed systematically by a proposed algorithm. Numerical examples show that this method has an excellent SINR (signal to noise-plus-interference ratio) performance and a complexity comparable to the standard adaptive beamformer. We also study the space-time adaptive processing (STAP) for MIMO radar systems. With a slight modification, STAP methods developed originally for the single-input multiple-output (SIMO) radar (phased array radar) can also be used in MIMO radar. However, in the MIMO radar, the rank of the jammer-and-clutter subspace becomes very large, especially the jammer subspace. It affects both the complexity and the convergence of the STAP algorithm. In this thesis, we explore the clutter space and its rank in the MIMO radar. By using the geometry of the problem rather than data, the clutter subspace can be represented using prolate spheroidal wave functions (PSWF). Using this representation, a new STAP algorithm is developed. It computes the clutter space using the PSWF and utilizes the block diagonal property of the jammer covariance matrix. Because of fully utilizing the geometry and the structure of the covariance matrix, the method has very good SINR performance and low computational complexity.

The second half of the thesis focuses on the transmitted waveform design for MIMO radar systems. We first study the ambiguity function of the MIMO radar and the corresponding waveform design methods. In traditional (SIMO) radars, the ambiguity function of the transmitted pulse characterizes the compromise between range and Doppler resolutions. It is a major tool for studying and analyzing radar signals. The idea of ambiguity function has recently been extended to the case of MIMO radar. In this thesis, we derive several mathematical properties of the MIMO radar ambiguity function. These properties provide some insights into the MIMO radar waveform design. We also propose a new algorithm for designing the orthogonal frequency-hopping waveforms. This algorithm reduces the sidelobes in the corresponding MIMO radar ambiguity function and makes the energy of the ambiguity function spread evenly in the range and angular dimensions. Therefore the resolution of the MIMO radar system can be improved. In addition to designing the waveform for increasing the system resolution, we also consider the joint optimization of waveforms and receiving filters in the MIMO radar for the case of extended target in clutter. An extended target can be viewed as a collection of infinite number of point targets. The reflected waveform from a point target is just a delayed and scaled version of the transmitted waveform. However, the reflected waveform from an extended target is a convolved version of the transmitted waveform with a target spreading function. A novel iterative algorithm is proposed to optimize the waveforms and receiving filters such that the detection performance can be maximized. The corresponding iterative algorithms are also developed for the case where only the statistics or the uncertainty set of the target impulse response is available. These algorithms guarantee that the SINR performance improves in each iteration step. The numerical results show that the proposed iterative algorithms converge faster and also have significant better SINR performances than previously reported algorithms. [1]

[1]I would like to acknowledge the office of Naval Reasearch and the National Science Foundation for their support.

Contents

Acknowledgments **iii**

Abstract **iv**

1 Introduction **1**

1.1 Basic Review of Radar 1

1.1.1 Detection and Ranging 1

1.1.2 Estimation of the Velocity 5

1.1.3 Beamforming 8

1.2 Review of MIMO Radar 11

1.2.1 The Virtual Array Concept 12

1.3 Outline of the Thesis 17

1.3.1 Robust Beamforming — Chapter 2 18

1.3.2 Efficient Space-Time Adaptive Processing — Chapter 3 19

1.3.3 Ambiguity Function and Waveform Design — Chapter 4 19

1.3.4 Joint Transmitted Waveform and Receiver Design — Chapter 5 20

1.4 Notations 20

2 Robust Beamforming **22**

2.1 Introduction 22

2.2 MVDR Beamformer and the Steering Vector Mismatch 24

2.3 Previous Work On Robust Beamforming 26

2.3.1 Diagonal Loading Method 26

2.3.2 LCMV Method 27

2.3.3 Extended Diagonal Loading Method 27

2.3.4 General-Rank Method 28
2.4 New Robust Beamformer 28
2.4.1 Frequency Domain View of the Problem 29
2.4.2 Two-Point Quadratic Constraint 30
2.4.3 Two-Point Quadratic Constraint with Diagonal Loading 34
2.5 Numerical Examples 37
2.6 Conclusions 50

3 Space-Time Adpative Processing for MIMO Radar 51
3.1 Introduction 51
3.2 STAP in MIMO Radar 53
3.2.1 Signal Model 53
3.2.2 Fully Adaptive MIMO-STAP 56
3.2.3 Comparison with SIMO System 58
3.2.4 Virtual Array 59
3.3 Clutter Subspace in MIMO Radar 60
3.3.1 Clutter Rank in MIMO Radar 61
3.3.2 Data Independent Estimation of the Clutter Subspace with PSWF 64
3.4 New STAP Method for MIMO Radar 67
3.4.1 The Proposed Method 67
3.4.2 Complexity of the New Method 68
3.4.3 Estimation of the Covariance Matrices 69
3.4.4 Zero-Forcing Method 69
3.4.5 Comparison with Other Methods 70
3.5 Numerical Examples 71
3.6 Conclusions 75

4 Ambiguity Function of the MIMO Radar and the Waveform Optimization 76
4.1 Introduction 76
4.2 Review of MIMO Radar Ambiguity Function 78
4.3 Properties of The MIMO Radar Ambiguity Function for ULA 81
4.4 Pulse MIMO Radar Ambiguity Function 88

4.5 Frequency-Hopping Pulses 90
4.6 Optimization of the Frequency-Hopping Codes 92
4.7 Design Examples 94
4.8 Conclusions 97

5 Waveform Optimization of the MIMO Radar for Extended Target and Clutter 100
5.1 Introduction 100
5.2 Problem Formulation and Review 103
5.2.1 Problem Formulation 105
5.2.2 Review of Pillai's method [82] 107
5.3 Proposed Iterative Method 108
5.4 Iterative Method with Random and Uncertain Target Impulse Response 112
5.4.1 Random Target Impulse Response 112
5.4.2 Uncertain Target Impulse Response 115
5.5 Numerical Examples 121
5.6 Conclusions 127
5.7 Appendix 127

6 Conclusion 130
6.1 Future Work 131

Bibliography 133

List of Figures

1.1 Basic radar for detection and ranging 2

1.2 Matched filter in the radar receiver 3

1.3 The LFM signal: (a) real part of an LFM waveform and (b) Fourier transfrom magnitude of the LFM waveform 4

1.4 Illustration of the Doppler effect 6

1.5 The pulse train 6

1.6 Doppler processing 8

1.7 Range r, azimuth angle θ, and elevation angle ϕ 9

1.8 A uniform linear antenna array (ULA) 10

1.9 (a) A MIMO radar system with $M = 3$ and $N = 4$. (b) The corresponding virtual array 13

1.10 (a) A ULA MIMO radar system with $M = 3$ and $N = 4$. (b) The corresponding virtual array 16

1.11 (a) A MIMO radar system with $M = 3$, $N = 4$ and $d_T = d_R$. (b) The corresponding virtual array 17

2.1 Frequency domain view of the optimization problem 30

2.2 Example of a solution of the two-point quadratic constraint problem that does not satisfy $|\mathbf{s}^\dagger \mathbf{w}| \geq 1$ for $\theta_1 \leq \theta \leq \theta_2$ 34

2.3 The locations of zeros of the beamformer in Fig. 2.2 34

2.4 An illustration of Algorithm 2, where $\mathcal{A} = \{\mathbf{w} \big| \, |\mathbf{s}^\dagger(\theta)\mathbf{w}| \geq 1, \, \theta = \theta_1, \theta_2\}$ and $\mathcal{B} = \{\mathbf{w} \big| \, |\mathbf{s}^\dagger(\theta)\mathbf{w}| \geq 1, \, \theta_1 \leq \theta \leq \theta_2\}$ 37

2.5 Example 1: SINR versus γ for SNR = 10dB. 39

2.6 Example 1 continued: SINR versus γ for SNR = 20dB 39

2.7 Example 2: SINR versus SNR 41

2.8 Example 3: SINR versus mismatch angle for SNR = 0dB 43

2.9 Example 3 continued: SINR versus mismatch angle for SNR = 10dB 43
2.10 Example 4: SINR versus number of antennas for SNR = 0dB 44
2.11 Example 4 continued: SINR versus number of antennas for SNR = 10dB 45
2.12 Example 5: SINR versus number of snapshots for SNR = 10dB 47
2.13 Estimated SOI power versus number of snapshots for SNR = 10dB 48
2.14 Example 6: SINR versus SNR for general type mismatch 49

3.1 This figure illustrates a MIMO radar system with M transmitting antennas and N receiving antennas. The radar station is moving with speed v 54
3.2 The SINR at looking direction zero as a function of the Doppler frequencies for different SIMO and MIMO systems 60
3.3 Example of the signal $c(x; f_{s,i})$. (a) Real part. (b) Magnitude response of Fourier transform 63
3.4 Plot of the clutter power distributed in each of the orthogonal basis elements 66
3.5 The SINR performance of different STAP methods at looking direction zero as a function of the Doppler frequency 72
3.6 Spatial beampatterns for four STAP methods 73
3.7 Space-time beampatterns for four methods: (a) The proposed zero-forcing method, (b) Principal component (PC) method [44], (c) Separate jammer and clutter cancellation method (SJCC) [56] and (d) Sample matrix inversion (SMI) method [44] 74

4.1 Examples of ambiguity functions: (a) Rectangular pulse, and (b) Linear frequency modulation (LFM) pulse with time-bandwidth product 10, where T is the pulse duration 79
4.2 MIMO radar scheme: (a) Transmitter, and (b) Receiver 79
4.3 Illustration of the LFM shearing 87
4.4 Illustration of the pulse waveform 88
4.5 (a) Real parts and (b) spectrograms of the waveforms obtained by the proposed method 95
4.6 (a) Real parts and (b) spectrograms of the orthogonal LFM waveforms 96
4.7 Empirical cumulative distribution function of $|\Omega(\tau, f, f')|$ 96
4.8 Cross-correlation functions $r^{\phi}_{m,m'}(\tau)$ of the waveforms generated by the proposed method 97
4.9 Cross correlation functions $r^{\phi}_{m,m'}(\tau)$ of the LFM waveforms 98

5.1 Illustration of (a) the signal model, and (b) the discrete baseband equivalent model . . 103
5.2 The FIR equivalent model 106
5.3 Example 5.1: The parameters used in the matrix AR model (a) matrix $\mathbf{A}$ and (b) matrix $\mathbf{B}$ 122
5.4 Example 5.1: Comparison of the SINR versus number of iterations 122
5.5 Example 5.1: (a)–(d) real part of the initial transmitted waveforms, (e)–(h) real part of the transmitted four waveforms $\mathbf{f}$ obtained by Algorithm 1, (i)–(l) real part of the four receiving filters $\mathbf{h}$ obtained by Algorithm 1 123
5.6 Example 5.2: Comparison of the SINR versus CNR 124
5.7 Example 5.3: Comparison of the SINR versus CNR with random target impulse response 125
5.8 Example 5.4: Comparison of the worst SINR versus CNR with uncertain target impulse response 126

List of Tables

3.1 List of the parameters used in the signal model 55

Chapter 1

Introduction

In this chapter, we review basic concepts from radar and MIMO radar and briefly describe the major results of each chapter. The chapter is organized as follows: Section 1.1 gives the basic review of the radar system. Section 1.2 reviews the basic concept of MIMO radar. Section 1.3 gives an outline of this thesis. Section 1.4 defines the notations used in this thesis.

1.1 Basic Review of Radar

The radar systems can be categorized into *monostatic* and *bistatic*. The transmitter and the receiver of a monostatic radar are located in the same location while the transmitter and receiver of the bistatic radar are far apart relative to the wavelength used in the radar. According to the characteristics of the transmitted signals, the radar systems can be further categorized into *continuous waveform radar* and *pulse radar*. The continuous waveform radar transmits a single continuous waveform while the pulse radar transmits multiple short pulses. Most of the modern radars are monostatic pulse radars [87]. In this thesis, we will consider both continuous waveform and pulse radar. However, we will study only monostatic radar throughout this thesis.

1.1.1 Detection and Ranging

Detection is the most fundamental function of a radar system. After emitting the electromagnetic waveform, the radar receives the reflected signal. To detect the target, it is necessary to distinguish the signal reflected from the target, from the signal containing only noise. After detecting the target, one can further calculate the range. In the radar community the word *range* is used to indicate the distance between the radar system and the target.

Consider a monostatic radar system with one antenna as shown in Fig. 1.1. The radar emits a waveform $u(t)$ into the space. The waveform hits the target located in range r and comes back to the antenna. After demodulation, the received signal can be expressed as [87]

$$\alpha u(t - \frac{2r}{c}) + v(t),$$

where c is the speed of wave propagation, r is the range of the target, $v(t)$ is the additive noise, and α denotes the amplitude response of the target. The amplitude response α is determined by the radar cross section (RCS) of the target, the range r of the target, the beampattern of the antenna, and the angle of the target. In the receiver, a matched filter is usually applied to enhance the signal-

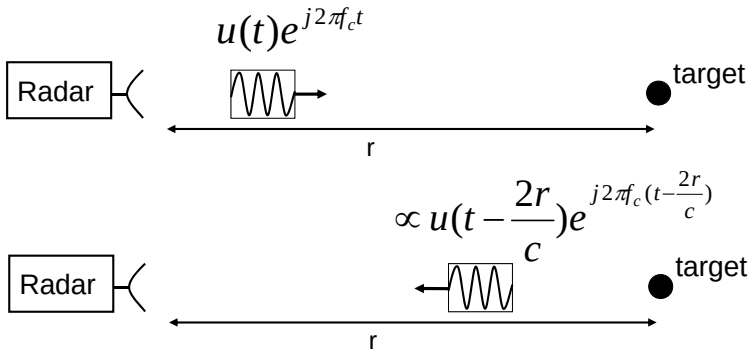

Figure 1.1: Basic radar for detection and ranging

to-noise ratio (SINR). The matched filter output can be expressed as

$$\begin{aligned} y(\tau) &= \int_{-\infty}^{\infty} \alpha u(t - \frac{2r}{c}) u^*(t - \tau) dt + \int_{-\infty}^{\infty} v(t) u^*(t - \tau) dt \\ &= \alpha r_{uu}(\tau - \frac{2r}{c}) + \int_{-\infty}^{\infty} v(t) u^*(t - \tau) dt, \end{aligned}$$

where $r_{uu}(\tau) = \int_{-\infty}^{\infty} u(t) u^*(t - \tau) d\tau$ is the autocorrelation function of $u(t)$. The input-output relation is illustrated in Fig. 1.2. To determine whether there is a target, the matched filter output signal is checked at a specific time instant τ_0. If $r_{uu}(\tau) > \eta$ for a predetermined threshold η, then the radar system reports that it has found a target. There is a trade-off between false alarm rate and detection rate when choosing the threshold η [100]. Small threshold η improves the detection rate but also increases the false alarm rate. On the other hand, large threshold reduces the false alarm rate but also decreases the detection rate. After detecting the target, one can further determines the

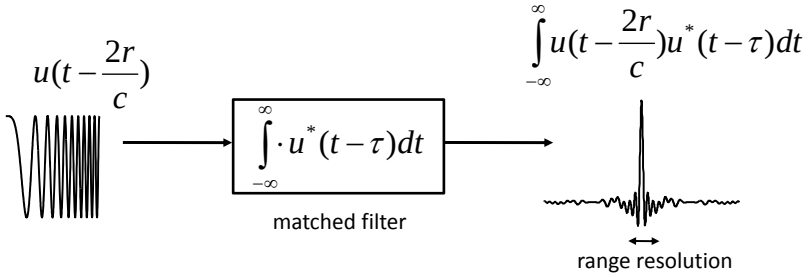

Figure 1.2: Matched filter in the radar receiver

range of the target. For a simple point target, the range of the target can be obtained by

$$r = \frac{1}{2}\tau_0 c,$$

where τ_0 is the time instant at which the matched filter output exceeds the threshold.

For the case of multiple targets, the matched filter output signal can be expressed as

$$y(\tau) = \sum_{i=0}^{N_t-1} \alpha_i r_{uu}(\tau - \frac{2r_i}{c}) + \int_{-\infty}^{\infty} v(t)u^*(t-\tau)dt,$$

where N_t is the number of targets, r_i is the range of the ith target, and α_i is the amplitude response of the ith target. To be able to distinguish these targets, the autocorrelation function $r_{uu}(\tau)$ has to be a narrow pulse in order to reduce the interferences coming from other targets. A narrow pulse in time-domain has a widely spread energy in its Fourer transform and vice versa. Therefore to obtain a narrow pulse $r_{uu}(\tau)$, one can choose the waveform $u(t)$ so that the energy of the Fourier transform of $r_{uu}(\tau)$ is widely spread. Fourier transform of the autocorrelation function $r_{uu}(\tau)$ is expressed as

$$S_{uu}(j\omega) = |U(j\omega)|^2,$$

where $U(j\omega)$ is the Fourier transform of the waveform $u(t)$. Therefore, one can choose $u(t)$ so that its energy is widely spread over different frequency components.

Another very important desirable property of the transmitted waveform is the constant modulus property. The constant modulus property allows the antenna to always work at the same power. This avoids the use of expensive amplifiers, and the nonlinear effect of the amplifiers. One good candidate that has widely spread energy in the frequency domain and also satisfies the constant

modulus property is the linear frequency modulated (LFM) waveform. It is also called the chirp waveform. The LFM waveform can be expressed as

$$u(t) \propto \begin{cases} e^{j2\pi f_c t} e^{j\pi k t^2}, & 0 \le t < T \\ 0, & \text{otherwise.} \end{cases}$$

where f_c is the carrier frequency, k is the parameter that determines the bandwidth of the signal, and T is the duration of the signal. The instantaneous frequency of the LFM waveform is the derivative of the phase function

$$\frac{1}{2\pi}\frac{d(2\pi f_c t + \pi k t^2)}{dt} = f_c + kt.$$

So the approximate bandwidth of the LFM signal is kT. The autocorrelation function of the LFM waveform can be approximated as [62]

$$r_{uu}(\tau) \approx \begin{cases} \left| \frac{\sin(\pi k T \tau (1 - \frac{|\tau|}{T})}{\pi k T \tau} \right|, & -T \le \tau < T. \\ 0, & \text{otherwise} \end{cases}$$

Fig. 1.3 shows the LFM waveform and the corresponding autocorrelation. The first zero-crossing

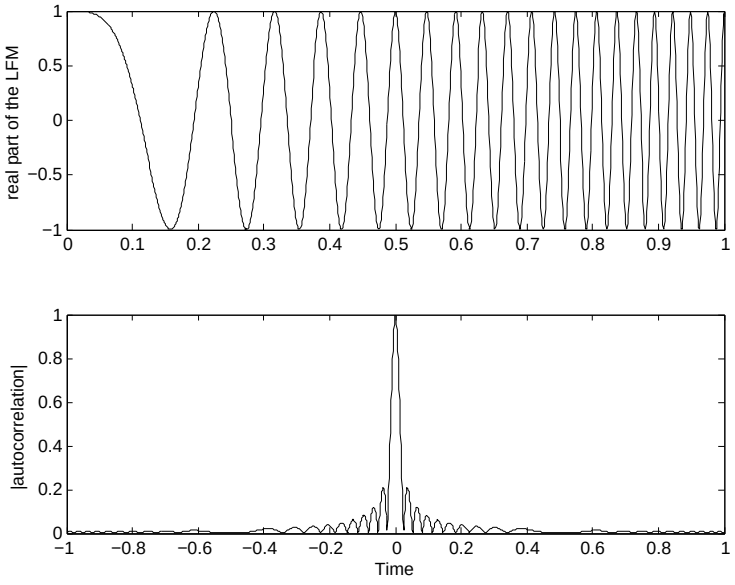

Figure 1.3: The LFM signal: (a) real part of an LFM waveform and (b) Fourier transfrom magnitude of the LFM waveform

of the autocorrelation function $r_{uu}(\tau)$ happens at the point $\frac{1}{kT}$. So we see that the waveform has

been "compressed" after the matched filtering from the original width T to $\frac{1}{kT}$. This effect is called *pulse compression*. The ratio between the original width and the compressed width is defined as the compression ratio. It can be expressed as

$$T/\frac{1}{kT} = kT^2.$$

We have previously mentioned that the bandwidth of the LFM signal is kT. So $kT^2 = (kT) \cdot T$ is the time-bandwidth product of the LFM signal. Thus the resolution of a radar system emitting LFM waveform is determined by the time-bandwidth product of the LFM waveform.

Another great benefit of the LFM signal is that it can be easily generated by circuits [92]. These advantages makes LFM signal the most widely used radar signal today [62,87]. In fact, LFM signal can even be found in some natural "radar system" such as the ultrasonic systems of bats and dolphins. We will talk more about the waveform design and introduce a useful tool called ambiguity function to analyze the waveforms in Chapter 4.

1.1.2 Estimation of the Velocity

Besides detection and ranging, radar system can be used to further measuring the velocity of an object. For example, police speed radar measures the velocity of moving vehicles. The radar systems can also use the velocity information to filter out the unwanted reflected signals. For example, for a radar system built to detect flying objects such as aircrafts or missiles, clouds will be the unwanted reflected signals. In radar community, this kind of unwanted signal is called *clutter*. In most of the case, the clutter can be very strong. Sometimes it may go up to 30 to 40 dB above the target signal. Fortunately, since the clutter objects are usually still or moving slowly, one can use the velocity information to filter it out. We will explain how radar systems obtain the velocity information.

Consider a monostatic radar system with one antenna and a moving target as shown in Fig. 1.4. The target moves with the speed v at an angle θ as shown in the figure. The radar system emits a narrowband waveform $u(t)e^{j2\pi f_c t}$. Here narrowband means the bandwidth of the signal is much smaller than the carrier frequency f_c. The waveform hits the moving target at range r and comes back to the antenna. After demodulation, the received waveform can be expressed as

$$\alpha u(t - \frac{2r}{c})e^{j2\pi f_D t} + v(t), \tag{1.1}$$

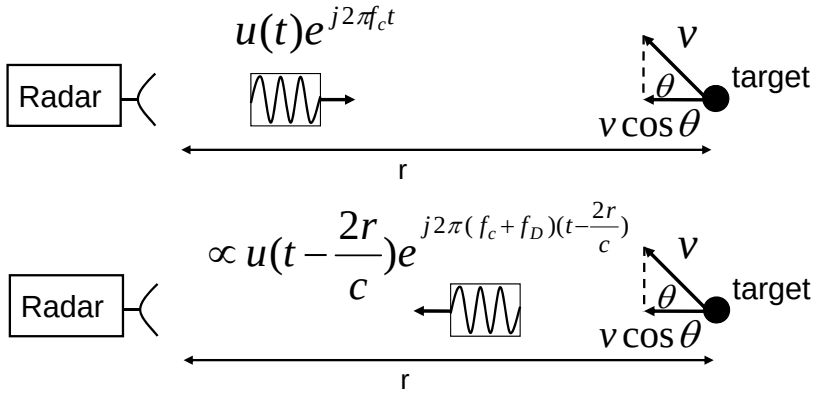

Figure 1.4: Illustration of the Doppler effect

where f_D is the Doppler frequency, α is the amplitude response of the target and $v(t)$ denotes the noise in the receiver. The Doppler frequency can be expressed as [62]

$$f_D = \frac{c + v\cos\theta}{c - v\cos\theta} f_c \approx \frac{2v\cos\theta}{c} f_c.$$

Note that f_D is much smaller than the carrier frequency f_c because the velocity of the object v is usually much smaller than the speed of light. Therefore, to effectively estimate the small Doppler frequency f_D, we will need a longer time window. One way to achieve this is to transmit multiple pulses. These pulses can occupy a longer time window as shown in Fig. 1.5. Therefore they provide better Doppler frequency resolution. Also, the computational complexity for processing pulses is

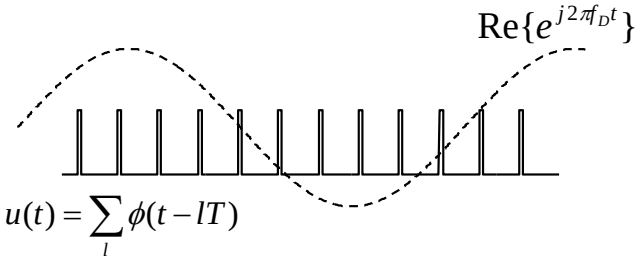

Figure 1.5: The pulse train

much smaller than processing a long continuous waveform. The radar systems which emit pulse trains are called *pulse radar*. Most modern radar systems are pulse radars. The transmitted signal

in pulse radar can be expressed as

$$u(t) = \sum_{l=0}^{L-1} \phi(t - lT), \tag{1.2}$$

where $\phi(t)$ is the basic shape pulse, l is the pulse index, T is the pulse repetition period, and L is the number of the total transmitted pulses. In radar community, l is often called *slow time* index and t is called *fast time*. The slow time is used to process the Doppler information while the fast time is used to process the range information. Fig. 1.5 illustrates a pulse train signal and the Doppler envelope. Using (1.2) and (1.1), the corresponding received signal becomes

$$\alpha \sum_{l=0}^{L-1} \phi(t - lT - \frac{2r}{c}) e^{j2\pi f_D t} + v(t).$$

Because the pulse $\phi(t)$ is narrow in time domain, one can approximate the Doppler term $e^{j2\pi f_D t}$ as a constant within the pulse. Thus the above equation can be approximated as

$$\alpha \sum_{l=0}^{L-1} \phi(t - lT - \frac{2r}{c}) e^{j2\pi f_D lT} + v(t).$$

Recall that the matched filter is used in the receiver to enhance the SNR and perform pulse compression. In the pulse radar case, it is sufficient to use the matched filter which matches to the pulse $\phi(t)$. The matched filter output can be expressed as

$$\begin{aligned} y(\tau) &= \alpha \sum_{l=0}^{L-1} \left(\int_{-\infty}^{\infty} \phi(t - lT - \frac{2r}{c}) \phi^*(t - \tau) dt \right) e^{j2\pi f_D lT} + \int_{-\infty}^{\infty} v(t) \phi^*(t - \tau) dt \\ &= \alpha \sum_{l=0}^{L-1} r_{\phi\phi}(\tau - lT + \frac{2r}{c}) e^{j2\pi f_D lT} + \int_{-\infty}^{\infty} v(t) \phi^*(t - \tau) dt. \end{aligned}$$

Using the above matched filter output, one can perform detection and ranging as described in the last section. To extract the Doppler information, after obtaining the range r, we can sample the matched filter output $y(\tau)$ associated with the range and obtain the peaks of the received signal as

$$\begin{aligned} y_q &= y(qT + \frac{2r}{c}) \\ &= \alpha \sum_{l=0}^{L-1} r_{\phi\phi}((q-l)T) e^{j2\pi f_D lT} + \int_{-\infty}^{\infty} v(t) \phi^*(t - qT + \frac{2r}{c}) dt \\ &\approx \alpha r_{\phi\phi}(0) e^{j2\pi f_D qT} + \int_{-\infty}^{\infty} v(t) \phi^*(t - qT + \frac{2r}{c}) dt, \end{aligned}$$

for $q = 0, 1, \cdots, L-1$. Computing the discrete Fourier transform $Y(f)$ of y_q, we obtain

$$\begin{aligned} |Y(f)| &= \left| \sum_{q=0}^{L-1} y_q e^{-j2\pi fq} \right| \\ &= \left| \alpha r_{\phi\phi}(t) \sum_{q=0}^{L-1} e^{-j2\pi fq} + \text{noise term} \right| \\ &= \left| \alpha r_{\phi\phi}(t) \frac{\sin(\pi L(f - F_D))}{\sin(\pi(f - f_D))} + \text{noise term} \right|. \end{aligned}$$

From the peak of the magnitude, we can estimate the Doppler frequency f_D. One can also use the Doppler processing to filter out the unwanted reflected signals. For example, suppose there are two targets at the same range r, but with different Doppler frequencies. Then the received signal associated with the range r can be expressed as

$$y_q \approx \alpha_1 r_{\phi\phi}(0) e^{j2\pi f_{D1} q} + \alpha_2 r_{\phi\phi}(0) e^{j2\pi f_{D_2} q} + \text{noise term},$$

where α_1 and α_2 are the amplitude responses of the targets and f_{D1} and f_{D2} are Doppler frequencies of the targets. The signal y_q has two frequency components. To separate them, one can put the signal y_q into a bandpass filter to extract the Doppler frequency of interest as shown in Fig. 1.6. For

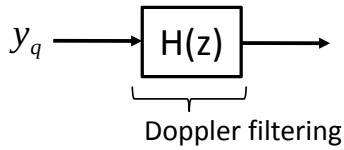

Figure 1.6: Doppler processing

example, when detecting the flying targets, the signal reflected by clouds is one major source of interference. However, the clouds usually move slowly compared to aircraft or missiles. One can use a filter to eliminate most of the unwanted reflected signals. We will talk more about Doppler processing in Chapter 3.

1.1.3 Beamforming

We have discussed about detection, ranging and measuring velocity using radar. We will talk about another important parameter, angle, in this subsection. The angle information along with the range information gives us the complete information about the target location. The target location can be

specified by three parameters (r, θ, ϕ), where θ is the azimuth angle and ϕ is the elevation angle. Fig. 1.7 illustrates these three parameters. In this thesis, we usually deal with only one angle because

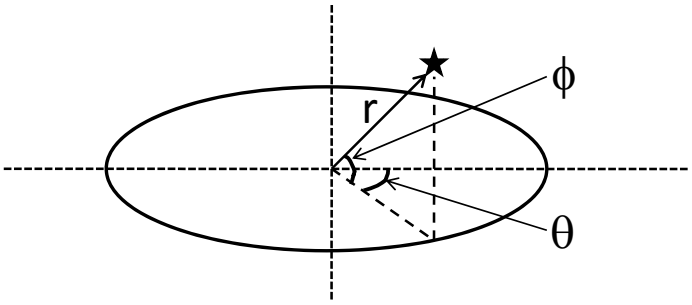

Figure 1.7: Range r, azimuth angle θ, and elevation angle ϕ

the two angles θ and ϕ can be processed independently. The one-dimensional results provided in this thesis can be easily generalized to two dimensions.

Antennas usually have different gain for signals transmitted to different angles and signals received from different angles. The antenna gain as a function of angles is called the beampattern $B(\theta)$. Consider an antenna with beampattern $B(\theta)$ which has a large gain around angle 0° but has small gains at other angles. We can use this antenna to detect a target at 0°. However, to detect targets at other angles, we need to mechanically rotate the antenna to the angle of interest. Rotating the antenna mechanically is costly and usually slow.

To avoid mechanically rotating the antenna, we can use a technology called *beamforming* which allowed us to change the beampattern electronically. This requires multiple antennas and usually these antennas have wider beampatterns. For convenience, we assume the antennas all have omnidirectional beampatterns. In other words, for every antenna, $B(\theta) = 1$ for all θ. The multiple antennas are placed uniformly on a straight line. This is called a uniform linear antenna array (ULA). Fig. 1.8 illustrates such an antenna array. Consider a narrowband plane wave with carrier frequency f_c impinging from angle θ. The received signal of the nth antenna can be expressed as

$$r_n(t) = \alpha s(t) e^{j\frac{2\pi}{\lambda} dn \sin\theta} + v(t),$$

for $n = 0, 1, \cdots, N-1$, where N is the number of antennas, $\lambda = \frac{c}{f_c}$ is the wavelength of the signal, $s(t)$ is the signal envelope, α is the amplitude response and $v(t)$ is the additive noise. The phase difference term $e^{j\frac{2\pi}{\lambda} dn \sin\theta}$ comes from different traveling distances to different antennas as shown

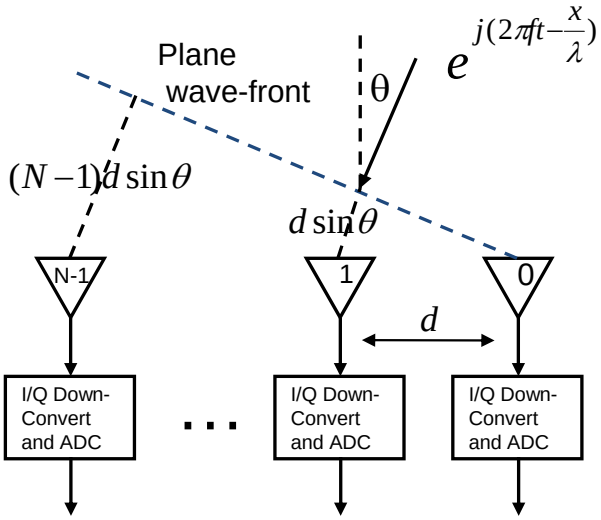

Figure 1.8: A uniform linear antenna array (ULA)

in Fig. 1.8. To extract signal from θ, one can linearly combine the received signals and obtain

$$\begin{aligned} y(t) &= \sum_{n=0}^{N-1} w_n r_n(t) \\ &= \alpha s(t) \underbrace{\sum_{n=0}^{N-1} w_n e^{j\frac{2\pi}{\lambda}dn\sin\theta}}_{B(\theta)} + \sum_{n=0}^{N-1} w_n v(t), \end{aligned} \tag{1.3}$$

where w_n is the weighting coefficient corresponding to the nth antenna. Observing the above equation, one can see that $y(t)$ has a different gain for signal coming from different angle θ. Therefore by linearly combining the signals, we can synthesize the beampattern $B(\theta)$ as shown in Eq. (1.3). Note that this beampattern $B(\theta)$ can be controlled by the weighting coefficients w_n.

To change the beampattern, we do not need to mechanically rotate the antenna. We can just change the weighting coefficients w_n and this can be done through using electronic devices. This technique is called electric beamforming and the weighting coefficients w_n are called *beamformer* coefficients. The beampattern can be expressed as

$$\begin{aligned} B(\theta) &= \sum_{n=0}^{N-1} w_n e^{j\frac{2\pi}{\lambda}dn\sin\theta} \\ &= \sum_{n=0}^{N-1} w_n e^{-j\omega n}\Big|_{\omega=\frac{2\pi}{\lambda}d\sin\theta} \\ &= W(e^{j\omega})\Big|_{\omega=\frac{2\pi}{\lambda}d\sin\theta} \end{aligned}$$

where $W(e^{j\omega})$ is the Fourier transform of the beamformer w_n. Therefore, the beamformer design problem can be treated as an FIR filter design problem. Typical FIR filter design algorithms such as Parks-McClellan algorithm can be applied to beamformer design. Note that in filter design problem, the frequency resolution of a filter depends on the filter order. Similarly, the spatial resolution of the beamformer depends on the number of antennas in the ULA array. Note that we have $\omega = \frac{2\pi}{\lambda} d \sin\theta$ in the above equation. If $d > \frac{\lambda}{2}$, there will be multiple values of θ mapping to the same ω. This is equivalent to the aliasing effect in sampling. To avoid this, one chooses $d \leq \frac{\lambda}{2}$. In practice, the spacing between antennas is about half of the wavelength. In this case,

$$-\pi \leq \omega = \frac{2\pi}{\lambda} d \sin\theta = \pi \sin\theta \leq \pi.$$

Then there will not be aliasing in the beampattern. Beamforming has long been used in many areas, such as radar, sonar, seismology, medical imaging, speech processing, and wireless communications. We will talk more about beamforming in Chapter 2.

1.2 Review of MIMO Radar

In the traditional phased array radar, the system can only transmit scaled versions of a single waveform. Because only a single waveform is used, the phased array radar is also called SIMO (single-input multiple-output) radar in contrast to the MIMO radar. We will use "SIMO radar" or "phased array radar" alternatively throughout the thesis.

The MIMO (multiple-input multiple-output) radar system allows transmitting orthogonal (or incoherent) waveforms in each of the transmitting antennas [7, 85]. These waveforms can be extracted by a set of matched filters in the receiver. Each of the extracted components contains the information of an individual transmitting path. There are two different kinds of approaches for using this information. First, the spatial diversity can be increased. In this scenario, the transmitting antenna elements are widely separated such that each views a different aspect of the target. Consequently the target radar cross sections (RCS) are independent random variables for different transmitting paths. Therefore, each of the components extracted by the matched filters in the receiver contains independent information about the target. Since we can obtain multiple independent measurements about the target, a better detection performance can be obtained [28–30]. Second, a better spatial resolution can be obtained. In this scenario, the transmitting antennas are

colocated such that the RCS observed by each transmitting path are identical. The components extracted by the matched filters in each receiving antenna contain the information of a transmitting path from one of the transmitting antenna elements to one of the receiving antenna elements. By using the information about all of the transmitting paths, a better spatial resolution can be obtained. The phase differences caused by different transmitting antennas along with the phase differences caused by different receiving antennas can form a new *virtual array* steering vector. With judiciously designed antenna positions, one can create a very long array steering vector with a small number of antennas. Thus the spatial resolution for clutter can be dramatically increased at a small cost [7,85]. We will soon introduce the virtual array concept. It has been shown that this kind of radar system has many advantages such as excellent clutter interference rejection capability [15, 75], improved parameter identifiability [67], and enhanced flexibility for transmitting beampattern design [37,94]. Some of the recent work on the colocated MIMO radar has been reviewed in [66]. In this chapter, we focus on the colocated MIMO radar.

1.2.1 The Virtual Array Concept

One of the main advantages of MIMO radar is that the degrees of freedom can be greatly increased by the concept of virtual array. In this section, we briefly review this concept. More detailed reviews can be found in [7, 32, 85, 88]. Consider an arbitrary transmitting array with M antenna elements and an arbitrary receiving array with N antenna elements. The mth transmitting antenna is located at $\mathbf{x}_{T,m} \in \mathbb{R}^3$ and the nth receiving antenna is located at $\mathbf{x}_{R,n} \in \mathbb{R}^3$. Fig. 1.9 (a) shows an example with $M = 3$ and $N = 4$. The mth transmitting antenna emits the waveform $\phi_m(t)$. The emitted waveforms are orthogonal, that is,

$$\int \phi_m(\tau)\phi_k^*(\tau)d\tau = \delta_{mk}.$$

In each receiving antenna, these orthogonal waveforms are extracted by M matched filters. Therefore, the total number of extracted signals equals NM. Consider a far-field point target. The target response in the mth matched filter output of the nth receiving antenna can be expressed as

$$y_{n,m}^{(t)} = \rho_t \exp(j\frac{2\pi}{\lambda}\mathbf{u}_t^T(\mathbf{x}_{T,m} + \mathbf{x}_{R,n})), \tag{1.4}$$

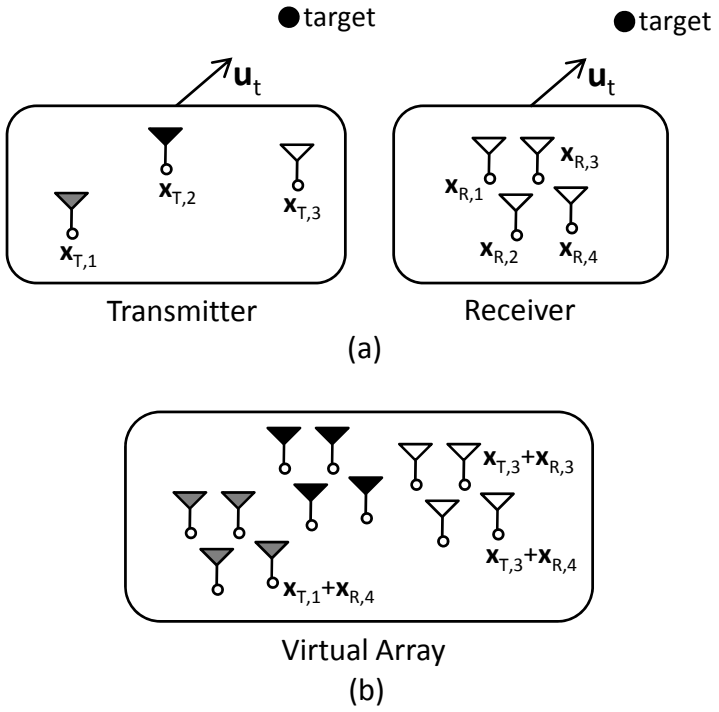

Figure 1.9: (a) A MIMO radar system with $M = 3$ and $N = 4$. (b) The corresponding virtual array

where $\mathbf{u}_t \in \mathbb{R}^3$ is a unit vector pointing toward the target from the radar station, and ρ_t is the amplitude of the signal reflected by the target. One can see that the phase differences are created by both the transmitting antenna locations and the receiving antenna locations. The target response in (1.4) is the same as the target response received by a receiving array with NM antenna elements located at

$$\{\mathbf{x}_{T,m} + \mathbf{x}_{R,n} |\ n = 0, 1, \cdots, N-1,\ m = 0, 1, \cdots, M-1\}.$$

We call this NM-element array a *virtual array*. Fig 1.9 (b) shows the corresponding virtual array of the MIMO radar system illustrated in (a). Thus, we can create an NM-element virtual array by using only $N + M$ physical antenna elements.

The relation between the transmitting array, receiving array, and the virtual array can be further characterized by a convolution [32]. Define

$$g_T(\mathbf{x}) \quad = \quad \sum_{m=0}^{M-1} \delta(\mathbf{x} - \mathbf{x}_{T,m}) \tag{1.5}$$

and

$$g_R(\mathbf{x}) \quad = \quad \sum_{n=0}^{N-1} \delta(\mathbf{x} - \mathbf{x}_{R,n}). \tag{1.6}$$

These functions characterize the antenna locations in the transmitter and receiver. Because the virtual array has NM virtual elements located at $\{x_{T,m} + x_{R,n}\}$, the corresponding function which characterizes the antenna location of the virtual array can be expressed as

$$g_V(\mathbf{x}) \quad = \quad \sum_{m=0}^{M-1} \sum_{n=0}^{N-1} \delta(\mathbf{x} - (\mathbf{x}_{T,m} + \mathbf{x}_{R,n})). \tag{1.7}$$

Comparing (1.5)–(1.7), one can see that

$$g_V(\mathbf{x}) = (g_T * g_R)(\mathbf{x}), \tag{1.8}$$

where $*$ denotes convolution. One can observe this relation from Fig. 1.9. The array in Fig. 1.9 (b) can be obtained by performing convolution of the arrays in Fig. 1.9 (a). This relation was observed in [32].

An idea somewhat related to the virtual array concept is called sum coarray [47, 58] . The main difference is that the sum coarray concept is applicable only to the SIMO system. In the SIMO

system, the overall beampattern is the product of the transmit and receive beampatterns. The overall beampattern is therefore related to a weight vector $\mathbf{w}_{tr}$ which equals the convolution of the transmit beamformer $\mathbf{w}_t$ and the receive beamformer $\mathbf{w}_r$. That is

$$\mathbf{w}_{tr} = \mathbf{w}_t * \mathbf{w}_r. \tag{1.9}$$

This new weight vector $\mathbf{w}_{tr}$ can be viewed as a beamformer of a longer array called coarray. In terms of the array geometry, this coarray is exactly the virtual array. However, these two approaches are completely different due to the difference between SIMO and MIMO systems. In the MIMO virtual array, the weight vector has a total of NM degrees of freedom. However, in coarray, the weight vector has only $N + M$ degrees of freedom because of (1.9). Also, the virtual array beamforming is performed in the receiver only, but the coarray beamforming is performed in the both sides of the transmitter and receiver.

■ **EXAMPLE 1.1: Uniform Linear Virtual Array.** Consider the a MIMO radar system with the uniform linear arrays (ULA) in both of the transmitter and the receiver. In this case, the antenna locations $x_{T,m}$ and $x_{R,n}$ reduce to scalars and

$$\begin{aligned} x_{R,n} &= nd_R, \quad n = 0, 1, \cdots, N-1 \\ x_{T,m} &= md_T, \quad m = 0, 1, \cdots, M-1, \end{aligned}$$

where d_R is the spacing between the receiving antennas, and d_T is the spacing between the transmitting antennas. Fig. 1.10 shows an example with $M = 3$ and $N = 4$. Similar to the arbitrary antenna case, the target response in the mth matched filter of the nth receiving antenna can be expressed as

$$\rho_t \exp(j\frac{2\pi}{\lambda}(nd_R \sin\theta + md_T \sin\theta)), \tag{1.10}$$

where θ is the looking direction of the target. The phase differences are created by both transmitting and receiving antenna locations. Define

$$f_s \triangleq \frac{d_R}{\lambda}\sin\theta, \text{ and } \gamma \triangleq \frac{d_T}{d_R}.$$

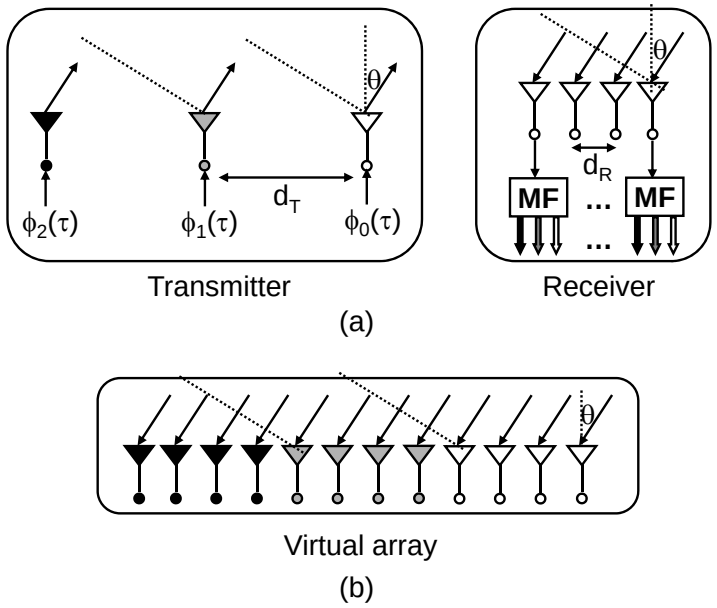

Figure 1.10: (a) A ULA MIMO radar system with $M = 3$ and $N = 4$. (b) The corresponding virtual array

Equation (1.10) can be further simplified as

$$\rho_t \exp(j2\pi f_s(n + \gamma m)).$$

If we choose

$$\gamma = N, \tag{1.11}$$

the set $\{n + \gamma m\}$ becomes $\{0, 1, \cdots, NM - 1\}$. Thus the NM signals in (1.10) can be viewed as the signals received by a *virtual array* with NM elements [7] as shown in Fig. 1.10 (b). It is as if we have a uniform linear receiving array with NM elements. Thus NM degrees of freedom can be obtained with only $N+M$ physical array elements. Similarly, we can obtain this result by using the convolution described in (1.8). From this point of view, one can see that the choice of $\gamma = N$ results in a uniform virtual array. One can view the antenna array as a way to sample the electromagnetic wave in the spatial domain. The MIMO radar idea allows "sampling" in both transmitter and receiver and creates a total of NM "samples". Taking advantage of these extra samples in spatial

domain, a better spatial resolution can be obtained.

■ **EXAMPLE 1.2: Overlapped Linear Virtual Array.** Instead of choosing $\gamma = N$ in (1.11), one can choose $\gamma = 1$. In this case, the target response in the mth antenna of the nth receiver can be expressed as

$$\rho_t \exp(j2\pi f_s(n+m)).$$

Fig. 1.11 shows an example of the transmitter, receiver and their corresponding virtual array. In

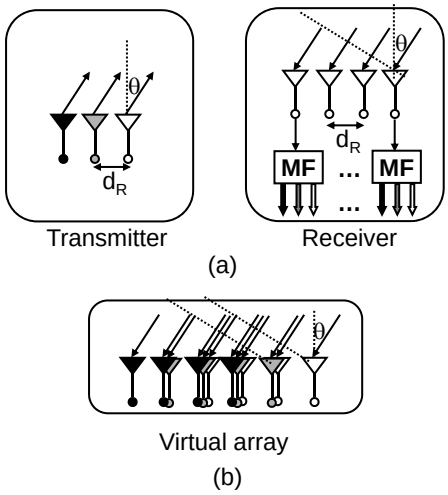

Figure 1.11: (a) A MIMO radar system with $M = 3$, $N = 4$ and $d_T = d_R$. (b) The corresponding virtual array

this case, the virtual array is more complicated: It has several virtual elements which are at the same locations. In some sense, we can regard this as a nonuniform virtual array. The advantage of choosing $\gamma = 1$ is that the radar station can form a focused beam by emitting correlated waveforms $\{\phi_m(t)\}$ [37]. The transmit beamforming can not be done in the case $\gamma = N$, because the sampling rate in the spatial domain is too low to prevent aliasing. However, the advantage of choosing $\gamma = N$ is that the virtual array is longer as shown in Fig. 1.10 (b) which results in a better spatial resolution.

1.3 Outline of the Thesis

This thesis covers many different aspect of the MIMO radar. Chapter 2 and Chapter 3 study the receiving algorithms in MIMO radar. In Chapter 2, a new algorithm for robust beamforming is proposed. The results in Chapter 2 have been published in [14]. Chapter 3 proposes a new efficient

algorithm for space-time adaptive processing in MIMO radar. The relevant results have been published in [15] and Chapter 6 of [70]. Chapter 4 and Chapter 5 study the transmitted waveform in MIMO radar. Chapter 4 introduces the MIMO ambiguity function and uses it to design the transmitted waveforms. The corresponding waveforms result in a good resolution for point targets. The result in Chapter 4 has been published in [16]. In Chapter 5, the waveform is optimized using the prior information about the target and clutter. Also, the corresponding receiving filter is jointly optimized to achieve better SINR performance. The result in Chapter 5 can be found in [18]. We will briefly explain the major results of each chapter in this section.

1.3.1 Robust Beamforming — Chapter 2

We have briefly explained the concept of beamforming in Sec. 1.1.3. The beamformer is used to extract the information from some angle of interest while suppressing the unwanted signal impinging from other angles. An adaptive beamformer uses the second order statistics of the received signal to maximize the SINR (signal to noise plus interference ratio) at the receiver. To maximize the SINR, one can minimize the total variance while maintaining the signal response to be unity. This beamformer is called minimum-variance distortionless response (MVDR) beamformer. The MVDR beamformer has the highest SINR among all the beamformers. However, it is very sensitive to the direction of arrival (DOA) mismatch. If there is a mismatch in DOA, the MVDR beamformer misinterprets the signal of interest as a source of interference and suppresses it. This effect is called self-cancelation and it greatly reduces the SINR. The virtual array formed in MIMO radar can be much larger than the physical receiving array in SIMO radar. A longer receiving array is more prone to suffer from the self-cancelation effect. Therefore the robustness of the beamformer is very important in MIMO radar. To improve the robustness of the beamformer, many approaches have been proposed, including diagonal loading methods [1, 13], linear constraint based methods [4, 8, 11, 26, 31, 96, 98, 103], quadratic constraint methods [84, 99], Bayesian methods [6], and convex set methods [27, 60, 63, 73, 102]. In Chapter 2, we propose an algorithm based on quadratic inequality constraints. The complexity of the proposed algorithm is the same as the MVDR beamformer but the proposed algorithm is much more robust against DOA mismatch.

1.3.2 Efficient Space-Time Adaptive Processing — Chapter 3

We have explained Doppler processing in Section 1.1.2 and beamforming in Section 1.1.3. Space-time adaptive processing (STAP) is the combination of both Doppler processing and beamforming. It linearly combines all the antenna outputs from different slow time indexes. The STAP is usually used in airborne radar. This is because the Doppler frequency of the ground clutter depends on the looking angle. Therefore in airborne radar the Doppler and angle information has to be jointly processed. Joint processing signals of two dimensions requires much more computational complexity. There have been many algorithms proposed in [35, 40, 43–45, 57, 105] and the references therein for improving the complexity and convergence of the STAP in the SIMO radar.

Using MIMO radar improves the angle resolution of the STAP. However, MIMO radar also increases the signal dimension by adding the new waveform-dimension. Therefore it requires more computational complexity. Furthermore, it requires more signal samples to estimate the second order statistics when the dimension of the signal is large. In Chapter 3, we propose an algorithm which fully uses the geometry of the problem and the characteristics of the covariance matrices. The proposed method has a significantly lower computational complexity and requires fewer training signal samples.

1.3.3 Ambiguity Function and Waveform Design — Chapter 4

We have discussed range resolution and pulse compression in Section 1.1.1. In fact the overall radar resolution combines range resolution, Doppler resolution and angle resolution. The overall resolution can be characterized by the radar ambiguity function. The radar ambiguity function is defined as the system response to a point target. A sharp radar ambiguity function implies the system has a good resolution to point targets. The ambiguity function is determined by the radar transmitted waveform. It is the major tool for analyzing the radar waveform. The radar ambiguity function has been extended to the MIMO case in [89].

It is known that there are several properties of the radar ambiguity function [62]. For example, the total energy of the SIMO radar ambiguity function is a constant. In Chapter 4, we propose and prove similar properties for the MIMO radar ambiguity function. These properties provide some insights for designing MIMO radar transmitted waveforms. In Chapter 4, we also propose a new waveform design method based on MIMO radar ambiguity function and simulated annealing. Numerical results show that the proposed waveforms have better resolutions than the orthogonal

linear frequency modulation waveforms.

1.3.4 Joint Transmitted Waveform and Receiver Design — Chapter 5

In Chapter 5, we consider joint transmitted waveform and receiver design with some prior information of the extended target and clutter. While the waveform design problem in Chapter 4 is optimal for point targets, the waveform design problem in Chapter 5 is for the extended target. An extended target can be viewed as a collection of infinite number of point targets. It can be characterized with a certain impulse response. The single-input single-output (SISO) version of this problem has been studied by DeLong and Hofstetter in 1967 [22–24] and more recently by Pillai et al. [82]. Different iterative methods have been proposed. In Chapter 5, we consider the MIMO extension of this problem. In the MIMO case, the method proposed in [22] cannot be applied because it is based on the symmetry property of the SISO radar ambiguity function. The method in [82] can still be applied to the MIMO case. However, this method does not guarantee the SINR to be nondecreasing in each iteration step. We propose a new iterative algorithm which can be applied to the MIMO case while guaranteeing the SINR to be nondecreasing in each iteration step. The corresponding iterative algorithms are also developed for the case where only the statistics or the uncertainty set of the target impulse response is available. These algorithms guarantee that the SINR performance improves in each iteration step. Numerical results show that the proposed methods have better SINR performance than existing design methods.

1.4 Notations

In this section, we define the notations used in this thesis. Matrices and vectors are denoted by capital letters in boldface (e.g., $\mathbf{A}$). Superscript ^{T} and † denote transpose and transpose conjugation respectively. The expression $(\mathbf{A})_{k,l}$ represents the element of matrix $\mathbf{A}$ located at the kth row and the lth column. The notation $\text{diag}(\mathbf{A}, \mathbf{A}, \cdots, \mathbf{A})$ denotes a block diagonal matrix whose diagonal blocks are $\mathbf{A}$. The notation $\text{tr}(\mathbf{A})$ denotes the trace of matrix $\mathbf{A}$. The notation $\|\mathbf{A}\|_F$ denotes the Frobenius norm of the matrix $\mathbf{A}$. The notation $\measuredangle a$ denotes the angle of the complex number a. The notation $\lfloor a \rfloor$ is defined as the largest integer smaller than a. The notation $\lceil a \rceil$ is defined as the smallest integer larger than a. The notation $(n \mod m)$ represents the remainder of division of n by m. The notation $\text{vec}(\mathbf{A})$ denotes a vector formed by reshaping the matrix $\mathbf{A}$. For example, for a

matrix $\mathbf{A} \in \mathcal{C}^{N \times M}$, the kth element of the vector $\mathbf{x} = \text{vec}(\mathbf{A}) \in \mathcal{C}^{NM \times 1}$ can be expressed as

$$(\mathbf{x})_k = (\mathbf{A})_{(k \mod N), \lfloor k \rfloor}.$$

Notation $E[x]$ denotes the expectation of the random variable x.

Chapter 2

Robust Beamforming

This chapter focuses on robust beamforming algorithms. We have briefly talked about beamforming in Chapter 1. Beamformers can be designed according to the statistics of the received signals to optimize for the system SINR (signal to interference plus noise ratio). It is well known that the performance of such a beamformer is very sensitive to direction-of-arrival (DOA) errors. In MIMO radar, the virtual array can be much larger than the physical receiving array in the SIMO radar. Therefore the robustness of the beamformer becomes even more important in the MIMO radar case.

In this chapter, an adaptive beamformer that is robust against the DOA mismatch is proposed. This method imposes two quadratic constraints such that the magnitude responses of two steering vectors exceed unity. Then a diagonal loading method is used to force the magnitude responses at the arrival angles between these two steering vectors to exceed unity. Therefore this method can always force the gains at a desired range of angles to exceed a constant level while suppressing the interferences and noise. A closed form solution to the proposed minimization problem is introduced, and the diagonal loading factor can be computed systematically by a proposed algorithm. Numerical examples show that this method has an excellent SINR performance and a complexity comparable to the standard adaptive beamformer. Most of the results of this chapter have been reported in our recent journal paper [14].

2.1 Introduction

A data-dependent beamformer was proposed by Capon in [12]. By exploiting the second order statistics of the array output, the method constrains the response of the SOI (signal of interest) to be

unity and minimizes the variance of the beamformer output. This method is called minimum variance distortionless response (MVDR) beamformer in the literature. The MVDR beamformer has very good resolution, and the SINR (signal-to-interference-plus-noise ratio) performance is much better than traditional data-independent beamformers. However, when the steering vector of the SOI is imprecise, the response of the SOI is no longer constrained to be unity and is thus attenuated by the MVDR beamformer while minimizing the total variance of the beamformer output [20]. The effect is called signal cancellation. It dramatically degrades the output SINR. A good introduction to this topic can be found in [64]. The steering vector of the SOI can be imprecise because of various reasons such as direction-of-arrival (DOA) errors, local scattering, near-far spatial signature mismatch, waveform distortion, source spreading, imperfectly calibrated arrays and distorted antenna shape [64], [44]. In this chapter, we focus on DOA uncertainty.

There are many methods developed for solving the DOA mismatch problem. In [4, 8, 11, 26, 31, 96, 98, 103], linear constraints have been imposed when minimizing the output variance. The linear constraints can be designed to broaden the main beam of the beampattern. These beamformers are called linearly constrained minimum variance (LCMV) beamformers. In [84] and [99], convex quadratic constraints have been used. In [6], a Bayesian approach has been used. For other types of mismatches, diagonal loading [1, 13] is known to provide robustness. However, the drawback of the diagonal loading method is that it is not clear how to choose a diagonal loading factor. In [27], the steering vector has been projected onto the signal-plus-interference subspace to reduce the mismatch. In [107], the magnitude responses of the steering vectors in a polyhedron set are constrained to exceed unity while the output variance is minimized. This method avoids the signal cancellation when the actual steering vector is in the designed polyhedron set. In [102], Vorobyov et al. have used a non-convex constraint which forces the magnitude responses of the steering vectors in a sphere set to exceed unity. This non-convex optimization problem has been reformulated in a convex form as a second order cone programming (SOCP) problem. It has been also proven in [102] that this beamformer belongs to the family of diagonal loading beamformers. In [63, 73], the sphere uncertainty set has been generalized to an ellipsoid set and the SOCP has been avoided by the proposed algorithms which efficiently calculate the corresponding diagonal loading level. In [91], a general rank case has been considered using similar idea as in [102] and an elegant closed form solution has been obtained.

In [63, 73, 91, 102, 107], the magnitude responses of steering vectors in an uncertainty set have

been forced to exceed unity while minimizing the output variance. The uncertainty set has been selected as polyhedron, sphere, or ellipsoid in order to be robust against general types of steering vector mismatches. In this chapter, we consider only the DOA mismatch. Inspired by these uncertainty based methods, we consider a simplified uncertainty set which contains only the steering vectors with a desired uncertainty range of DOA. To find a suboptimal solution for this problem, the constraint is first loosened to two non-convex quadratic constraints such that the magnitude responses of two steering vectors exceed unity. Then a diagonal loading method is used to force the magnitude responses at the arrival angles between these two steering vectors to exceed unity. Therefore this method can always force the gains at a desired range of angles to exceed a constant level while suppressing the interferences and noise. A closed form solution to the proposed minimization problem is introduced, and the diagonal loading factor can be computed systematically by a proposed iterative algorithm. Numerical examples show that this method has an excellent SINR performance and a complexity comparable to the standard MVDR beamformer.

The rest of the chapter is organized as follows: The MVDR beamformer and the analysis of steering vector mismatch are presented in Section 2.2. Some previous work on robust beamforming is reviewed in Section 2.3. In Section 2.4, we develop the theory and the algorithm of our new robust beamformer. Numerical examples are presented in Section 2.5. Finally, the conclusions are presented in Section 2.6.

2.2 MVDR Beamformer and the Steering Vector Mismatch

Consider a uniform linear array (ULA) of N omnidirectional sensors with interelement spacing d. The signal of interest (SOI) is a narrowband plane wave impinging from angle θ. The baseband array output $\mathbf{y}(t)$ can be expressed as

$$\mathbf{y}(t) \quad = \quad x(t)\mathbf{s}(\theta) + \mathbf{v}(t),$$

where $\mathbf{v}(t)$ denotes the sum of the interferences and the noises, $x(t)$ is the signal of interest (SOI), and $\mathbf{s}(\theta)$ represents the baseband array response of the SOI. It is called steering vector and can be expressed as

$$\mathbf{s}(\theta) \quad \triangleq \quad \left(\begin{array}{cccc} 1 & e^{j\frac{2\pi}{\lambda}d\sin\theta} & \cdots & e^{j(N-1)\frac{2\pi}{\lambda}d\sin\theta} \end{array} \right)^T, \tag{2.1}$$

where λ is the operating wavelength. The output of the beamformer can be expressed as $\mathbf{w}^\dagger \mathbf{y}(t)$, where $\mathbf{w}$ is the complex weighting vector. The output SINR (signal-to-interferences-plus-noise ratio) of the beamformer is defined as

$$\text{SINR} \triangleq \frac{E|x(t)\mathbf{w}^\dagger \mathbf{s}(\theta)|^2}{E|\mathbf{w}^\dagger \mathbf{v}(t)|^2} = \frac{\sigma_x^2 |\mathbf{w}^\dagger \mathbf{s}(\theta)|^2}{\mathbf{w}^\dagger \mathbf{R_v} \mathbf{w}}, \tag{2.2}$$

where $\mathbf{R_v} \triangleq E[\mathbf{v}(t)\mathbf{v}^\dagger(t)]$, and $\sigma_x^2 \triangleq E[|x(t)|^2]$. By varying the weighting factors the output SINR can be maximized by minimizing the total output variance while constraining the SOI response to be unity. This can be written as the following optimization problem:

$$\begin{aligned} &\min_{\mathbf{w}} \mathbf{w}^\dagger \mathbf{R_y} \mathbf{w} \\ &\text{subject to } \mathbf{s}^\dagger(\theta)\mathbf{w} = 1, \end{aligned} \tag{2.3}$$

where $\mathbf{R_y} \triangleq E[\mathbf{y}(t)\mathbf{y}^\dagger(t)]$. This is equivalent to minimizing $\mathbf{w}^\dagger \mathbf{R_v} \mathbf{w}$ subject to $|\mathbf{s}^\dagger(\theta)\mathbf{w}| = 1$ because

$$\begin{aligned} \mathbf{w}^\dagger \mathbf{R_y} \mathbf{w} &= \mathbf{w}^\dagger \mathbf{R_v} \mathbf{w} + \sigma_x^2 |\mathbf{s}^\dagger(\theta)\mathbf{w}|^2 \\ &= \mathbf{w}^\dagger \mathbf{R_v} \mathbf{w} + \sigma_x^2 \cdot 1. \end{aligned}$$

The solution to this problem is well-known and was first given by Capon in [12] as

$$\mathbf{w}_c = \frac{{\mathbf{R_y}}^{-1}\mathbf{s}(\theta)}{\mathbf{s}^\dagger(\theta){\mathbf{R_y}}^{-1}\mathbf{s}(\theta)}. \tag{2.4}$$

This beamformer is called minimum variance distortionless response (MVDR) beamformer in the literature. When there is a mismatch between the actual arrival angle θ and the assumed arrival angle θ_m, this beamformer becomes

$$\mathbf{w}_m = \frac{{\mathbf{R_y}}^{-1}\mathbf{s}(\theta_m)}{\mathbf{s}^\dagger(\theta_m){\mathbf{R_y}}^{-1}\mathbf{s}(\theta_m)}. \tag{2.5}$$

It can be viewed as the solution to the minimization problem

$$\begin{aligned} &\min_{\mathbf{w}} \mathbf{w}^\dagger \mathbf{R_y} \mathbf{w} \\ &\text{subject to } \mathbf{s}^\dagger(\theta_m)\mathbf{w} = 1. \end{aligned} \tag{2.6}$$

Because $\mathbf{w}^\dagger \mathbf{R_y} \mathbf{w} = \mathbf{w}^\dagger \mathbf{R_v} \mathbf{w} + \sigma_x^2 |\mathbf{s}^\dagger(\theta)\mathbf{w}|^2$, and $\mathbf{s}^\dagger(\theta)\mathbf{w} = 1$ is no longer valid due to the mismatch, the SOI magnitude response might be attenuated as a part of the objective function. This suppression leads to severe degradation in SINR, because the SOI is treated as a interference in this case. The phenomenon is called signal cancellation. A small mismatch can lead to a severe degradation in the SINR.

2.3 Previous Work On Robust Beamforming

Many approaches have been proposed for improving the robustness of the standard MVDR beamformer. In this section, we briefly mention some of them related to our work.

2.3.1 Diagonal Loading Method

In [1, 13], the optimization problem in Eq. (2.3) is modified as

$$\begin{aligned} &\min_{\mathbf{w}} \mathbf{w}^\dagger (\mathbf{R_y} + \gamma \mathbf{I_N}) \mathbf{w} \\ &\text{subject to } \mathbf{s}^\dagger(\theta)\mathbf{w} = 1, \end{aligned}$$

This approach is called diagonal loading in the literature. It increases the variance of the artificial white noise by the amount γ. This modification forces the beamformer to put more effort in suppressing white noise rather than interferences. As before, when the SOI steering vector is mismatched, the SOI is attenuated as one of the interferences. As the beamformer puts less effort in suppressing the interferences and noise, the signal cancellation problem addressed in Section 2.2 is reduced. However, when γ is too large, the beamformer fails to suppress strong interferences because it puts most effort to suppress the white noise. Hence there is a trade-off between reducing signal cancellation and effectively suppressing interferences. For that reason, it is not clear how to choose a good diagonal loading factor γ in the traditional MVDR beamformer.

2.3.2 LCMV Method

In [4, 8, 11, 26, 31, 96, 98, 103], the linear constraint of the MVDR in Eq. (2.3) has been generalized to a set of linear constraints as

$$\begin{aligned} &\min_{\mathbf{w}} \mathbf{w}^{\dagger}\mathbf{R}_{\mathbf{y}}\mathbf{w} \\ &\text{subject to } \mathbf{C}^{\dagger}\mathbf{w} = \mathbf{f}, \end{aligned} \tag{2.7}$$

where $\mathbf{C}^{\dagger}$ is an $L \times N$ matrix and $\mathbf{f}$ is an $L \times 1$ vector. The solution can be found by using Lagrange multiplication method as

$$\mathbf{w_l} = {\mathbf{R}_{\mathbf{y}}}^{-1}\mathbf{C}(\mathbf{C}^{\dagger}{\mathbf{R}_{\mathbf{y}}}^{-1}\mathbf{C})^{-1}f.$$

This is called the linearly constrained minimum variance (LCMV) beamformer. These linear constraints can be directional constraints [96, 103] or derivative constraints [4, 11, 26]. The directional constraints force the responses of multiple neighbor steering vectors to be unity. The derivative constraints force not only the response to be unity but also several orders of the derivatives of the beampattern in the assumed DOA to be zero. These constraints broaden the main beam of the beampattern so that it is more robust against the DOA mismatch. In [98], linear constraints have further been used to allow an arbitrary specification of the quiescent response.

2.3.3 Extended Diagonal Loading Method

In [102], the following optimization problem is considered.

$$\begin{aligned} &\min_{\mathbf{w}} \mathbf{w}^{\dagger}\mathbf{R}_{\mathbf{y}}\mathbf{w} \\ &\text{subject to } |\mathbf{w}^{\dagger}\mathbf{s}| \geq 1, \forall\, \mathbf{s} \in \mathcal{E}, \end{aligned} \tag{2.8}$$

where $\mathcal{E}$ is a sphere defined as

$$\mathcal{E} = \{\bar{\mathbf{s}} + \mathbf{e} \;\big|\; \|\mathbf{e}\| \leq \epsilon\}, \tag{2.9}$$

where $\bar{\mathbf{s}}$ is the assumed steering vector. The constraint forces the magnitude responses of an uncertainty set of steering vectors to exceed unity. The constraint is actually non-convex. However,

in [102], it is reformulated to a second order cone programming (SOCP) problem which can be solved by using some existing tools such as SeDuMi in MATLAB. It has also been proven in [102] that the solution to Eq. (2.8) has the form $c(\mathbf{R_y} + \gamma\mathbf{I_N})^{-1}\bar{\mathbf{s}}$ for some appropriate c and γ. Therefore this method can be viewed as an extended diagonal loading method [63]. In [63,73], the uncertainty set in Eq. (2.9) has been generalized to an ellipsoid and the SOCP has been avoided by the proposed algorithms which directly calculate the corresponding diagonal loading level γ as a function of $\mathbf{R_y}$, $\bar{\mathbf{s}}$ and ϵ.

2.3.4 General-Rank Method

In [91], a general-rank signal model is considered. The steering vector $\mathbf{s}$ is assumed to be a random vector that has a covariance $\mathbf{R_s}$. The mismatch is therefore modeled as an error matrix $\mathbf{\Delta}_1 \in \mathbf{C}^{N\times N}$ in the signal covariance matrix $\mathbf{R_s}$ and an error matrix $\mathbf{\Delta}_2 \in \mathbf{C}^{N\times N}$ in the output covariance matrix $\mathbf{R_y}$. The following optimization problem is considered:

$$\begin{aligned}&\min_{\mathbf{w}} \max_{\|\mathbf{\Delta}_2\|_F \le \gamma} \mathbf{w}^\dagger(\mathbf{R_y} + \mathbf{\Delta}_2)\mathbf{w} \\ &\text{subject to } \mathbf{w}^\dagger(\mathbf{R_s} + \mathbf{\Delta}_1)\mathbf{w} \ge 1 \;\forall\; \|\mathbf{\Delta}_1\|_F \le \epsilon,\end{aligned}$$

where $\|\mathbf{\Delta}\|_F$ denotes the Frobenius norm of the matrix $\mathbf{\Delta}$, and ϵ and γ are the upper bounds of the Frobenius norms of the error matrices Δ_1 and Δ_2, respectively. This optimization problem has an elegant closed form solution as shown by Shahbazpanahi et al. in [91], namely,

$$\mathbf{w_n} = P\{(\mathbf{R_y} + \gamma\mathbf{I_N})^{-1}(\mathbf{R_s} - \epsilon\mathbf{I_N})\}, \tag{2.10}$$

where $P\{\mathbf{A}\}$ denotes the principal eigenvector of the matrix $\mathbf{A}$. The principal eigenvector is defined as the eigenvector corresponding to the largest eigenvalue.

2.4 New Robust Beamformer

In this chapter, we consider the DOA mismatch. When there is a mismatch, the minimization in Eq. (2.6) suppresses the magnitude response of the SOI. To avoid this, we should force the magnitude responses at a range of arrival angles to exceed unity while minimizing the total output variance.

This optimal robust beamformer problem can be expressed as

$$\begin{aligned} &\mathbf{w}_d = \arg\min_{\mathbf{w}} \mathbf{w}^\dagger \mathbf{R}_\mathbf{y} \mathbf{w} \\ &\text{subject to } |\mathbf{s}^\dagger(\theta)\mathbf{w}|^2 \geq 1 \text{ for } \theta_1 \leq \theta \leq \theta_2, \end{aligned} \tag{2.11}$$

where θ_1 and θ_2 are the lower and upper bounds of the uncertainty of SOI arrival angle respectively, and $\mathbf{s}(\theta)$ is the steering vector defined in Eq. (2.1) with the arrival angle θ. The following uncertainty set of steering vectors is considered:

$$\{\mathbf{s} = \begin{pmatrix} 1 & e^{j\omega} & \cdots & e^{j(N-1)\omega} \end{pmatrix}^T \mid \omega_1 \leq \omega \leq \omega_2\}, \tag{2.12}$$

where $\omega_1 \triangleq 2\pi \sin\theta_1/\lambda$, and $\omega_2 \triangleq 2\pi \sin\theta_2/\lambda$. This uncertainty set is a curve. This constraint protects the signals in the range of angles $\theta_1 \leq \theta \leq \theta_2$ from being suppressed.

2.4.1 Frequency Domain View of the Problem

Substituting Eq. (2.12) into the constraint in Eq. (2.11), the constraint can be rewritten as

$$\left| \sum_{n=0}^{N-1} w_n e^{-j\omega n} \right| = |W(e^{j\omega})| \geq 1 \text{ for } \omega_1 \leq \omega \leq \omega_2,$$

where $W(e^{j\omega})$ is the Fourier transform of the weight vector $\mathbf{w}$. The objective function $\mathbf{w}^\dagger \mathbf{R}_\mathbf{y} \mathbf{w}$ can also be rewritten in the frequency domain as

$$\begin{aligned} \mathbf{w}^\dagger \mathbf{R}_\mathbf{y} \mathbf{w} &= \sum_{n=0}^{N-1} \sum_{m=0}^{N-1} w_n^* R_{y,n,m} w_m \\ &= \sum_{n=0}^{N-1} \sum_{m=0}^{N-1} w_n^* r_y(n-m) w_m \\ &= \frac{1}{2\pi} \int_0^{2\pi} |W(e^{j\omega})|^2 S_y(e^{j\omega}) d\omega, \end{aligned}$$

where $S_y(e^{j\omega})$ is the power spectral density (PSD) of the array output $\mathbf{y}$. Therefore, the optimization problem can be rewritten in the frequency domain as

$$\begin{aligned} &\min_{\mathbf{w}} \int_0^{2\pi} |W(e^{j\omega})|^2 S_y(e^{j\omega}) d\omega \\ &\text{subject to } |W(e^{j\omega})| \geq 1 \text{ for } \omega_1 \leq \omega \leq \omega_2. \end{aligned}$$

Note that $S_y(e^{j\omega})$ is a weighting function in the above integral. The frequency domain view of this optimization problem is illustrated in Fig. 2.1. The integral of $|W(e^{j\omega})|^2 S_y(e^{jw})$ is minimized

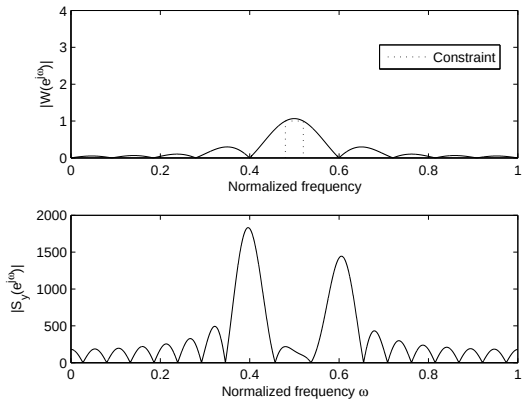

Figure 2.1: Frequency domain view of the optimization problem

while $|W(e^{j\omega})| \geq 1$ for $\omega_1 \leq \omega \leq \omega_2$ is satisfied. Even though we will not solve the problem in the frequency domain, it is insightful to look at it this way.

2.4.2 Two-Point Quadratic Constraint

It is not clear how to solve the optimal beamformer $\mathbf{w}_d$ in Eq. (2.11) because the constraint does not fit into any of the existing standard optimization methods. The constraint $|\mathbf{s}^\dagger(\theta)\mathbf{w}|^2 \geq 1$ for $\theta_1 \leq \theta \leq \theta_2$ can be viewed as infinite number of non-convex quadratic constraints. To find a suboptimal solution, we start looking for the solution by loosening the constraint. We first loosen the constraint by choosing only two constraints $|\mathbf{s}^\dagger(\theta_1)\mathbf{w}|^2 \geq 1$ and $|\mathbf{s}^\dagger(\theta_2)\mathbf{w}|^2 \geq 1$ from the infinite constraints $|\mathbf{s}^\dagger(\theta)\mathbf{w}|^2 \geq 1$ for $\theta_1 \leq \theta \leq \theta_2$. The corresponding optimization problem can be written as

$$\begin{aligned} &\min_{\mathbf{w}} \mathbf{w}^\dagger \mathbf{R}_\mathbf{y} \mathbf{w} \\ &\text{subject to } |\mathbf{s}^\dagger(\theta_1)\mathbf{w}|^2 \geq 1, \text{ and } |\mathbf{s}^\dagger(\theta_2)\mathbf{w}|^2 \geq 1. \end{aligned} \tag{2.13}$$

Because of the fact that the constraint is loosened, the minimum to this problem is a lower bound of the original problem in Eq. (2.11). Note that the constraint in Eq (2.13) is a non-convex quadratic constraint. In order to obtain an analytic solution, we reformulate the problem in the following

equivalent form:

$$\min_{\mathbf{w},\phi,\rho_0\geq 1,\rho_1\geq 1} \mathbf{w}^\dagger \mathbf{R_y} \mathbf{w}$$
$$\text{subject to } \mathbf{S}^\dagger \mathbf{w} = \begin{pmatrix} \rho_0 \\ \rho_1 e^{j\phi} \end{pmatrix},$$

where

$$\mathbf{S} = \begin{pmatrix} \mathbf{s}(\theta_1) & \mathbf{s}(\theta_2) \end{pmatrix},$$

and ρ_0, ρ_1, and ϕ are real numbers.

To solve this problem, we divide it into two parts. We first assume ϕ, ρ_0, and ρ_1 are constants and solve $\mathbf{w}$. The solution $\mathbf{w}$ will be a function of ϕ, ρ_0, and ρ_1. Then the solution $\mathbf{w}$ can be substituted back into the objective function so that the objective function becomes a function of ϕ, ρ_0, and ρ_1. Finally, we minimize the new objective function by choosing ϕ, ρ_0, and ρ_1. Define the function

$$L(\mathbf{w}, \mathbf{b}) = \mathbf{w}^\dagger \mathbf{R_y} \mathbf{w} - \mathbf{b}^\dagger \mathbf{S}^\dagger \mathbf{w}, \tag{2.14}$$

where $\mathbf{b} \in \mathbf{C}^2$ is the Lagrange multiplier. Taking the gradient of Eq. (2.14) and equating it to zero, we obtain the solution

$$\mathbf{w}_0 = {\mathbf{R_y}}^{-1} \mathbf{S} \mathbf{b}.$$

Substituting the above equation into the constraint, the Lagrange multiplier can be expressed as

$$\mathbf{b} = (\mathbf{S}^\dagger {\mathbf{R_y}}^{-1} \mathbf{S})^{-1} \begin{pmatrix} \rho_0 \\ \rho_1 e^{j\phi} \end{pmatrix}.$$

Substituting $\mathbf{b}$ back into $\mathbf{w}_0$, we obtain

$$\mathbf{w}_0 = {\mathbf{R_y}}^{-1} \mathbf{S} (\mathbf{S}^\dagger {\mathbf{R_y}}^{-1} \mathbf{S})^{-1} \begin{pmatrix} \rho_0 \\ \rho_1 e^{j\phi} \end{pmatrix}. \tag{2.15}$$

Given ϕ, ρ_0, and ρ_1, $\mathbf{w}_0$ can be found from the above equation. Note that it is exactly the solution to the LCMV beamformer mentioned in Sec. 2.3.2 with two directional constraints. Therefore, this approach can be viewed as an LCMV beamformer with a further optimized $\mathbf{f}$ in Eq. (2.7).

However, this approach is reformulated from the non-convex quadratic problem in Eq. (2.13). It is intrinsically different from a linearly constrained problem. The task now is to solve for ϕ, ρ_0, and ρ_1. Write

$$(\mathbf{S}^\dagger {\mathbf{R}_\mathbf{y}}^{-1} \mathbf{S})^{-1} = \begin{pmatrix} r_0 & r_2 e^{j\beta} \\ r_2 e^{-j\beta} & r_1 \end{pmatrix},$$

where r_0, r_1, and r_2 are real nonnegative numbers. Substituting $\mathbf{w}_0$ in Eq. (2.15) into the objective function, it becomes

$$\begin{aligned} \mathbf{w}_0^\dagger \mathbf{R}_\mathbf{y} \mathbf{w}_0 &= \begin{pmatrix} \rho_0 & \rho_1 e^{-j\phi} \end{pmatrix} (\mathbf{S}^\dagger {\mathbf{R}_\mathbf{y}}^{-1} \mathbf{S})^{-1} \begin{pmatrix} \rho_0 \\ \rho_1 e^{j\phi} \end{pmatrix} \\ &= r_0\rho_0^2 + r_1\rho_1^2 + 2\mathrm{Re}\{r_2\rho_0\rho_1 e^{j(\beta+\phi)}\} \\ &\geq r_0\rho_0^2 + r_1\rho_1^2 - 2r_2\rho_0\rho_1. \end{aligned} \tag{2.16}$$

To minimize the objective function, ϕ can be chosen as

$$\phi = -\beta + \pi \tag{2.17}$$

so that the last equality in Eq. (2.16) holds. Now ϕ and $\mathbf{w}_0$ are obtained by Eq. (2.17) and Eq. (2.15), and the objective function becomes Eq. (2.16). To further minimize the objective function, ρ_0, and ρ_1 can be found by solving the following optimization problem:

$$\min_{\rho_0 \geq 1,\ \rho_1 \geq 1} r_0\rho_0^2 + r_1\rho_1^2 - 2r_2\rho_0\rho_1.$$

This can be solved by using the Karush-Kuhn-Tucker (KKT) condition. The following solution can be obtained:

$$\begin{aligned} \rho_0 &= \begin{cases} 1, & r_2/r_0 \leq 1 \\ r_2/r_0, & r_2/r_0 > 1 \end{cases}, \\ \rho_1 &= \begin{cases} 1, & r_2/r_1 \leq 1 \\ r_2/r_1, & r_2/r_1 > 1 \end{cases}. \end{aligned} \tag{2.18}$$

Summarizing Eq. (2.17), Eq. (2.18), and Eq. (2.15), the following algorithm for solving the beamformer with the two-point quadratic constraint in Eq. (2.13) is obtained.

Algorithm 1 *Given θ_1, θ_2, and $\mathbf{R_y}$, compute $\mathbf{w}_0$ by the following steps:*

1. $\mathbf{S} \leftarrow \begin{pmatrix} \mathbf{s}(\theta_1) & \mathbf{s}(\theta_2) \end{pmatrix}$.
2. $\mathbf{V} \leftarrow (\mathbf{R_y})^{-1}\mathbf{S}$.
3. $\mathbf{R} \triangleq \begin{pmatrix} r_0 & r_2 e^{j\beta} \\ r_2 e^{-j\beta} & r_1 \end{pmatrix} \leftarrow (\mathbf{S}^\dagger \mathbf{V})^{-1}$.
4. $\phi \leftarrow -\beta + \pi$.
   $$\rho_0 \leftarrow \begin{cases} 1, & r_2/r_0 \le 1 \\ r_2/r_0, & r_2/r_0 > 1 \end{cases}.$$
   $$\rho_1 \leftarrow \begin{cases} 1, & r_2/r_1 \le 1 \\ r_2/r_1, & r_2/r_1 > 1 \end{cases}.$$
5. $\mathbf{w}_0 \leftarrow \mathbf{VR} \begin{pmatrix} \rho_0 \\ \rho_1 e^{j\phi} \end{pmatrix}$.

The matrix inversion in Step 2 contains most of the complexity of the algorithm. Therefore the algorithm has the same order of complexity as the MVDR beamformer. Because the constraint is loosened, the feasible set of the two-point quadratic constraint problem in Eq. (2.13) is a superset of the feasible set of the original problem in Eq. (2.11). The minimum found in this problem is a lower bound of the minimum of the original problem. If the solution $\mathbf{w}_0$ in the two-point quadratic constraint problem in Eq. (2.13) happens to satisfy the original constraint $|\mathbf{s}^\dagger(\theta)\mathbf{w}_0|^2 \ge 1$ for $\theta_1 \le \theta \le \theta_2$, then $\mathbf{w}_0$ is exactly the solution to the original problem in Eq. (2.11). The example provided in Fig. 2.1 is actually found by using the two-point quadratic constraint instead of the original constraint, but it also satisfies the original constraint. This makes it exactly the solution to the original problem in Eq. (2.11).

Unfortunately, in general the original constraint $|\mathbf{s}^\dagger(\theta)\mathbf{w}| \ge 1$ for $\theta_1 \le \theta \le \theta_2$ is not guaranteed to be satisfied by the solution of the two-point quadratic constraint problem in Eq. (2.13). Fig. 2.2 shows an example where the original constraint is not satisfied. This example is obtained by increasing the power of the SOI in the example in Fig. 2.1. One can compare $|S_y(e^{j\omega})|$ in Fig. 2.1 and Fig. 2.2 and find that the SOI power is much stronger in Fig. 2.2. In this case, the beamformer tends to put a zero between θ_1 and θ_2 to suppress the strong SOI. This makes $|W(e^{j\omega})| \le 1$ for some ω between ω_1 and ω_2. The original constraint is thus not satisfied. This problem will be overcome by a method provided in the next section.

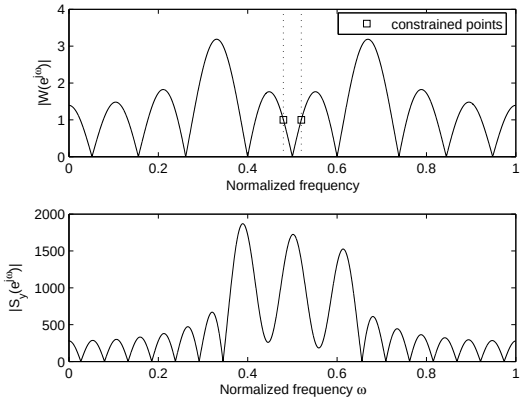

Figure 2.2: Example of a solution of the two-point quadratic constraint problem that does not satisfy $|\mathbf{s}^\dagger \mathbf{w}| \geq 1$ for $\theta_1 \leq \theta \leq \theta_2$

2.4.3 Two-Point Quadratic Constraint with Diagonal Loading

In Fig. 2.2, we observe that the energy of $\mathbf{w}$, $\|\mathbf{w}\|^2 = \int_0^{2\pi} |W(e^{j\omega})|^2 d\omega/(2\pi)$ is quite large compared to that in Fig. 2.1. Fig. 2.3 shows the locations of the zeros of the z-transform $W(z)$ of the beamformer in Fig. 2.2. One can observe that there is a zero between θ_1 and θ_2. This zero causes

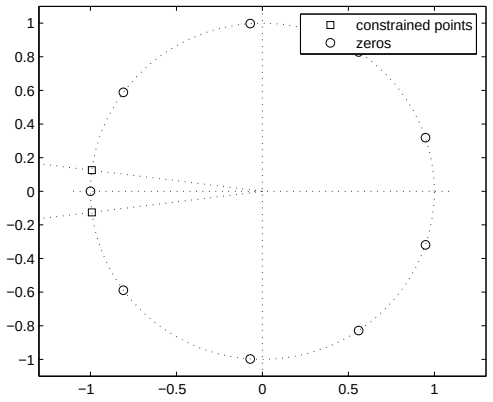

Figure 2.3: The locations of zeros of the beamformer in Fig. 2.2

the signal cancellation in Fig. 2.2. It can be observed that the zero is very close to those two points which are constrained to have magnitudes greater than unity. When a zero is close to these quadratically constrained points, it attenuates the gain at these points. However, the magnitude responses at these points are constrained to exceed unity. To satisfy the constraints, the overall energy of $\mathbf{w}$ must be adjusted to a certain high level. Therefore, if a zero is between θ_1 and θ_2 as happened in

Fig. 2.3, the norm of the weighting vector $\|\mathbf{w}\|$ will become very large. By using this fact, we can impose some penalty on $\|\mathbf{w}\|^2$ to force the zeros between θ_1 and θ_2 to go away. This can be done by the diagonal loading approach mentioned in Sec. 2.3.1. The corresponding optimization problem can be written as

$$\begin{aligned} &\mathbf{w}_\gamma = \arg\min_{\mathbf{w}} \mathbf{w}^\dagger \mathbf{R}_\mathbf{y} \mathbf{w} + \gamma \|\mathbf{w}\|^2 \\ &\text{subject to } |\mathbf{s}^\dagger(\theta_1)\mathbf{w}| \geq 1, \text{ and } |\mathbf{s}^\dagger(\theta_2)\mathbf{w}| \geq 1, \end{aligned} \tag{2.19}$$

where γ is the diagonal loading factor which represents the amount of the penalty put on $\|\mathbf{w}\|^2$. The solution $\mathbf{w}_\gamma$ can be found by performing the following modification on the output covariance matrix:

$$\mathbf{R}_\mathbf{y} \leftarrow \mathbf{R}_\mathbf{y} + \gamma \mathbf{I}_N$$

and then applying Algorithm 1. When $\gamma \to \infty$, the solution converges to

$$\begin{aligned} &\mathbf{w}_\infty = \arg\min_{\mathbf{w}} \|\mathbf{w}\|^2 \\ &\text{subject to } |\mathbf{s}^\dagger(\theta_1)\mathbf{w}| \geq 1, \text{ and } |\mathbf{s}^\dagger(\theta_2)\mathbf{w}| \geq 1. \end{aligned} \tag{2.20}$$

The following lemma gives the condition for which $\mathbf{w}_\infty$ satisfies the constraint $|\mathbf{s}(\theta)^\dagger \mathbf{w}_\infty| \geq 1$ for all θ in $\theta_1 \leq \theta \leq \theta_2$.

Lemma 1 $|\mathbf{s}^\dagger(\theta)\mathbf{w}_\infty| \geq 1$ *for* $\theta_1 \leq \theta \leq \theta_2$ *if and only if* $|\sin\theta_2 - \sin\theta_1| \leq \lambda/(dN)$.

Proof: According to Eq. (2.20), substituting $\mathbf{R}_\mathbf{y} = \mathbf{I}_N$ and applying Algorithm 1, one can obtain

$$\mathbf{w}_\infty = \frac{1}{N + |\text{sincd}(\frac{\omega_2 - \omega_1}{2})|} (\mathbf{s}(\theta_1) + \mathbf{s}(\theta_2) e^{j\frac{(\omega_2-\omega_1)(N-1)}{2}}),$$

where

$$\begin{aligned} &\omega_1 \triangleq \frac{2\pi}{\lambda} d \sin\theta_1, \ \omega_2 \triangleq \frac{2\pi}{\lambda} d \sin\theta_2, \text{ and} \\ &\text{sincd}(\omega) \triangleq \frac{\sin(\omega N)}{\sin\omega}. \end{aligned}$$

By direct substitution, one can obtain

$$|\mathbf{s}^{\dagger}(\theta)\mathbf{w}_{\infty}| = \left| \frac{\text{sincd}(\frac{\omega_1-\omega}{2}) + a \cdot \text{sincd}(\frac{\omega_2-\omega}{2})}{N + |\text{sincd}(\frac{\omega_2-\omega_1}{2})|} \right|, \tag{2.21}$$

where $\omega \triangleq \frac{2\pi}{\lambda} d \sin\theta$ and

$$a = \begin{cases} 1 & \text{, if sincd}(\frac{\omega_2-\omega_1}{2}) > 0 \\ -1 & \text{, otherwise.} \end{cases}$$

By Eq. (2.21), it can be verified that

$$|\mathbf{s}^{\dagger}(\theta)\mathbf{w}_{\infty}| \geq 1 \text{ for } \omega_1 \leq \omega \leq \omega_2$$

if and only if

$$|\omega_2 - \omega_1| \leq \frac{2\pi}{N}$$

which can also be expressed as $|\sin\theta_2 - \sin\theta_1| \leq \lambda/(dN)$.

If the condition $|\sin\theta_1 - \sin\theta_2| \leq \lambda/(dN)$ is satisfied, there exists a $\gamma > 0$ such that the condition $|\mathbf{s}^{\dagger}(\theta)\mathbf{w}_{\gamma}| \geq 1$ for $\theta_1 \leq \theta \leq \theta_2$ is satisfied. For example, if $d = \lambda/2$, $N = 10$, $\theta_1 = 35^{\circ}$ and $\theta_2 = 55^{\circ}$ then we have

$$|\sin(55^{\circ}) - \sin(35^{\circ})| \approx 0.1824 \leq \frac{\lambda}{dN} = 0.2.$$

In this case, there exists a $\gamma > 0$ so that the robust condition $|\mathbf{s}^{\dagger}(\theta)\mathbf{w}_{\gamma}| \geq 1$ for $35^{\circ} \leq \theta \leq 55^{\circ}$ is satisfied. However, introducing the diagonal loading changes the objective function $\mathbf{w}^{\dagger}\mathbf{R}_{\mathbf{y}}\mathbf{w}$ to $\mathbf{w}^{\dagger}(\mathbf{R}_{\mathbf{y}} + \gamma\mathbf{I}_N)\mathbf{w}$. The modification of the objective function affects the suppression of the interferences. To keep the objective function correct, γ should be chosen as small as possible while the condition $|\mathbf{s}^{\dagger}(\theta)\mathbf{w}| \geq 1$ for $\theta_1 \leq \theta \leq \theta_2$ is satisfied. For finding such a γ, we propose the following algorithm:

Algorithm 2 *Given θ_1, θ_2, $\mathbf{R}_{\mathbf{y}}$, an initial value of γ, a search step size $\alpha > 1$ and a set of angles, ζ_i, $i =$*

$1, 2, \cdots, n$ *which satisfies* $\theta_1 < \zeta_i < \theta_2$ *for all* i, $\mathbf{w}_\gamma$ *can be computed by the following steps:*

1. $\mathbf{R_y} \leftarrow \mathbf{R_y} + \gamma \mathbf{I}_N$.
2. *Compute* $\mathbf{w}_\gamma$ *by Algorithm 1.*
3. *If* $|\mathbf{s}^\dagger(\zeta_i)\mathbf{w}_\gamma| \geq 1$ *for all* $i = 1, 2, \cdots, n$

   then stop.

   else $\gamma \leftarrow \alpha\gamma$, *and go to 1.*

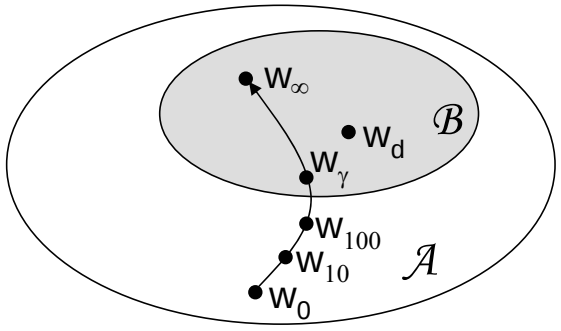

Figure 2.4: An illustration of Algorithm 2, where $\mathcal{A} = \{\mathbf{w} \big| \, |\mathbf{s}^\dagger(\theta)\mathbf{w}| \geq 1, \, \theta = \theta_1, \theta_2\}$ and $\mathcal{B} = \{\mathbf{w} \big| \, |\mathbf{s}^\dagger(\theta)\mathbf{w}| \geq 1, \, \theta_1 \leq \theta \leq \theta_2\}$

Fig. 2.4 illustrates how Algorithm 2 works. In this figure, the set $\mathcal{A} = \{\mathbf{w} \big| \, |\mathbf{s}^\dagger(\theta)\mathbf{w}| \geq 1, \, \theta = \theta_1, \theta_2\}$ is the feasible set of the two-point quadratic constraint problem in Eq. (2.13). The set $\mathcal{B} = \{\mathbf{w} \big| \, |\mathbf{s}^\dagger(\theta)\mathbf{w}| \geq 1, \, \theta_1 \leq \theta \leq \theta_2\}$ is the feasible set of the mismatched steering vector problem in Eq. (2.11). If the condition $|\sin\theta_1 - \sin\theta_2| \leq \lambda/(dN)$ is satisfied, Lemma 1 shows that $\mathbf{w}_\infty \in \mathcal{B}$. In this case, there exists a $\gamma > 0$ so that $\mathbf{w}_\gamma \in \mathcal{B}$. Algorithm 2 keeps increasing γ by multiplying α until $|\mathbf{s}^\dagger(\zeta_i)\mathbf{w}_\gamma| \geq 1$ for all $i = 1, 2, \cdots, n$ is satisfied. This is an approximation for $\mathbf{w}_\gamma \in \mathcal{B}$. The number n can be very small. In the next section, $n = 3$ works well for all the cases. Also the SINR is not sensitive to the choice of α, as we will see later.

2.5 Numerical Examples

For the purpose of design examples, the same parameters used in [73] are used in this section. An uniform linear array (ULA) of $N = 10$ omnidirectional sensors spaced half-wavelength apart (i.e., $d = \lambda/2$) is considered. There are three signals impinging upon this array:

1. the signal of interest (SOI) $x(t)$ with angle of arrival θ,

2. an interference signal $x_{int1}(t)$ with angle of arrival $\theta_{int1} = 30°$, and

3. another interference signal $x_{int2}(t)$ with angle of arrival $\theta_{int2} = 75°$.

The received narrowband array output can be modeled as

$$\mathbf{y}(t) = x(t)\mathbf{s}(\theta) + x_{int1}(t)\mathbf{s}(\theta_{int1}) + x_{int2}(t)\mathbf{s}(\theta_{int2}) + \mathbf{n}(t),$$

where $\mathbf{s}(\theta)$ is the steering vector defined in Eq. (2.1) and $\mathbf{n}(t)$ is the noise. We assume $x(t)$, $x_{int1}(t)$, $x_{int2}(t)$ and $\mathbf{n}(t)$ are zero-mean wide-sense stationary random process satisfying

$$\begin{aligned} E[\mathbf{n}(t)\mathbf{n}^\dagger(t)] &= \mathbf{I}_N \\ E[|x(t)|^2] &= \sigma_x^2 = \text{SNR} \cdot 1 \\ E[|x_{int1}(t)|^2] &= \sigma_{int1}^2 = 10^4 \text{ (40dB above noise)} \\ E[|x_{int2}(t)|^2] &= \sigma_{int2}^2 = 10^2 \text{ (20dB above noise).} \end{aligned}$$

Thus the covariance matrix of the narrowband array output $\mathbf{y}(t)$ can be expressed as

$$\begin{aligned} \mathbf{R}_\mathbf{y} &\triangleq E[\mathbf{y}(t)\mathbf{y}^\dagger(t)] \\ &= \sigma_x^2\mathbf{s}(\theta)\mathbf{s}^\dagger(\theta) + \sum_{i=1}^{2} \sigma_{int,i}^2 \mathbf{s}(\theta_{int,i})\mathbf{s}^\dagger(\theta_{int,i}) + \mathbf{I}_N. \end{aligned}$$

Example 1: SINR versus diagonal loading factor γ

In this example, the actual arrival angle θ is $43°$, but the assumed arrival angle θ_m is $45°$. The SINR defined in Eq. (2.2) is compared for different diagonal loading factor γ. The following three methods involving diagonal loading are considered:

1. *Algorithm 1* in the new method with $\theta_1 = 42°$ and $\theta_2 = 48°$.

2. *General-rank method* [91] in Eq. (2.10) with the parameter

$$\epsilon = \max_{48° \geq \theta \geq 42°} \|\mathbf{s}(\theta)\mathbf{s}^\dagger(\theta) - \mathbf{s}(45°)\mathbf{s}^\dagger(45°)\|_F \approx 4.73.$$

3. *Diagonal loading method* [1, 13] in Sec. 2.3.1.

4. *Directional LCMV* [96, 103] with two linear constraints which forces the responses of the signals from 42° and 48° to be unity.

5. *Derivative LCMV* [4, 11, 26] with two linear constraints which forces the responses of the signals from 45° to be unity and the derivative of the beampattern on 45° to be zero.

The SINR of the MVDR beamformer without mismatch is also plotted. This is an upper bound on the SINR. Fig. 2.5 shows the result for SNR = 10dB. One can observe that there is a huge jump in

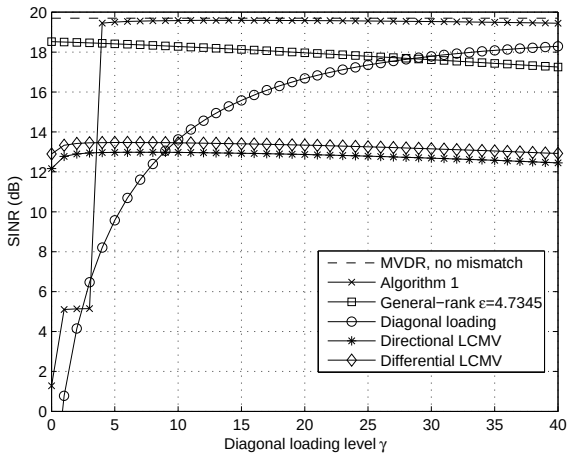

Figure 2.5: Example 1: SINR versus γ for SNR = 10dB.

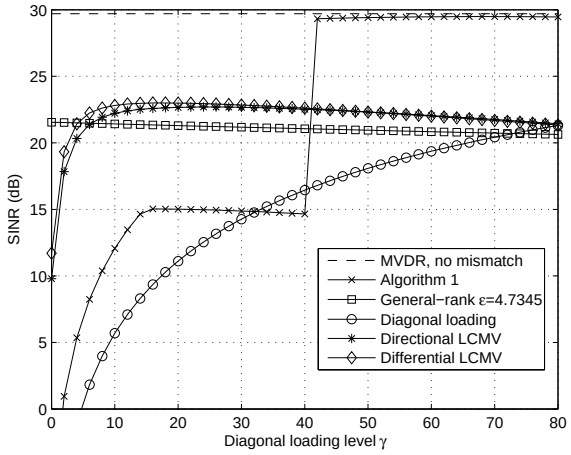

Figure 2.6: Example 1 continued: SINR versus γ for SNR = 20dB

the SINR of Algorithm 1 around $\gamma = 3$. When this happens, the SINR of Algorithm 1 increases significantly and becomes very close to the upper bound provided by the MVDR beamformer without

mismatch. This jump happens when the beampattern is changing from Fig. 2.2 to Fig. 2.1. Once the beamformer enters the set $\mathcal{B}$ as illustrated in Fig. 2.4, the SINR increases dramatically. After that, the SINR decays slowly as γ increases because of the over-suppression of white noise. Fig. 2.6 shows the case of SNR = 20dB. For large SNR, larger γ is needed for the beamformer to be in set $\mathcal{B}$. Observing Fig. 2.5 and Fig. 2.6, we can see why Algorithm 2 works so well. Algorithm 2 increases γ by repeatedly multiplying α until $\mathbf{w}_\gamma$ satisfies $|\mathbf{w}_\gamma^\dagger \mathbf{s}(\zeta_i)| \geq 1$ for $i = 1, 2, \cdots, n$. This happens as γ crosses the jump in SINR. Also, the SINR is not sensitive to the choice of α because the SINR decays very slowly after the jump. By Algorithm 2, we can find a suitable γ with only a few iterations. For other approaches involving diagonal loading, it is not clear how to find a good diagonal loading factor γ. One can observe that Algorithm 1 has a very different SINR performance than the two-point directional LCMV with diagonal loading. This shows that further optimization of the parameters ϕ, ρ_0, and ρ_1 in Sec. 2.4.2 is very crucial.

Example 2: SINR versus SNR

In this example, the actual arrival angle θ is 43°, but the assumed arrival angle θ_m is 45°. The SINR in Eq. (2.2) are compared for different SNRs ranging from -20dB to 30dB. The following methods are considered:

1. *Algorithm 2* with $\theta_1 = 42^\circ$, $\theta_2 = 48^\circ$, $\zeta_1 = 43.5^\circ$, $\zeta_2 = 45^\circ$, $\zeta_3 = 46.5^\circ$, initial $\gamma = 1$ and step size $\alpha = 2$.

2. *General-rank method*. Same as in Example 1.

3. *Extended diagonal loading method* [63,73,102] in Eq. (2.8) with the parameter

$$\epsilon = \max_{48^\circ \geq \theta \geq 42^\circ} \|\mathbf{s}(\theta) - \mathbf{s}(45^\circ)\| \approx 1.95.$$

   The algorithm in [63] is used to compute the diagonal loading level.

4. *Directional LCMV [96,103] with two linear constraints* which force the responses of the signals from 42°, 48° to be unity.

5. *Directional LCMV with three linear constraints* at the angles 42°, 45°, and 48°.

6. *Derivative LCMV with two linear constraints* which force the responses of the signals from 45° to be unity and the derivative of the beampattern on 45° to be zero.

7. *Derivative LCMV with three linear constraints* which force the responses of the signals from 45° to be unity and both the first and second derivatives of the beampattern on 45° to be zero.

8. *The standard MVDR beamformer* in Eq. (2.5).

Due to the fact that no finite-sample effect is considered, except in Algorithm 2 and extended diagonal loading method, no diagonal loading has been used in these methods. Again, the SINR of the MVDR beamformer without mismatch is also plotted as a benchmark. The results are shown in Fig. 2.7. The SINR of the standard MVDR beamformer is seriously degraded with only 2° of

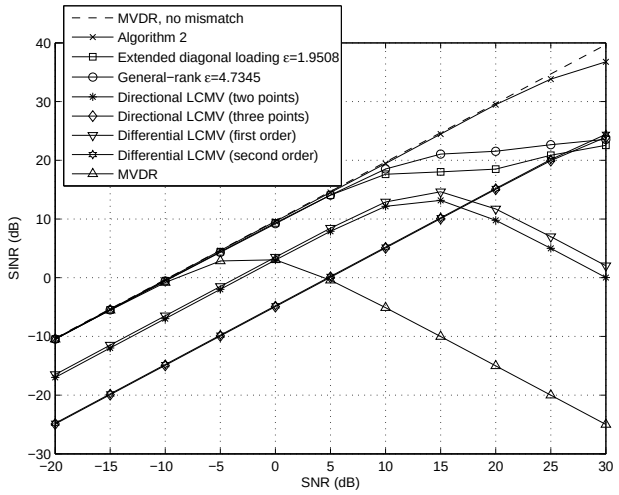

Figure 2.7: Example 2: SINR versus SNR

mismatch. When the SNR increases, the MVDR beamformer tends to suppress the strong SOI to minimize the total output variance. Therefore, in the high SNR region, the SINR decreases when SNR increases. The LCMV beamformers have good performances in high SNR region. However, the performance in low SNR region is much worse compared to other methods. This is because the linear equality constraints are too strong compared to the quadratic inequality constraints. One can observe that for both directional and derivative LCMV methods, each extra linear constraint decreases the SINR by about the same amount in the low SNR region. In this example, Algorithm 2 has the best SINR performance. It is very close to the upper bound provided by the MVDR beamformer without mismatch. Algorithm 2 has a better SINR performance than the general rank method [91] and the extended diagonal loading method [63,73,102] because the uncertainty set has been simplified to be robust only against DOA mismatch. Note that even though these methods have worse performances than Algorithm 2 with regard to DOA error, they have the advantages

of robustness against more general types of steering vector mismatches. The number of iterations in Algorithm 2 depends on the SNR and the choice of α. For instance, it converges with two steps when SNR = 10dB and six steps when SNR = 20dB in this example.

Example 3: SINR versus mismatch angle

In this example, the assumed signal arrival angle θ_m is 45°, and the actual arrival angle ranges from $\theta = 41^\circ$ to $\theta = 49^\circ$. The SINR in Eq. (2.2) is compared for different mismatched angles $(\theta - \theta_m)$. The following methods are considered:

1. *Algorithm 2* with $\theta_1 = 41^\circ$, $\theta_2 = 49^\circ$, $\zeta_1 = 43^\circ$, $\zeta_2 = 45^\circ$, $\zeta_3 = 47^\circ$, initial $\gamma = 1$ and step size $\alpha = 2$.

2. *General-rank method* [91] in Eq. (2.10) with the parameter

$$\epsilon = \max_{49^\circ \geq \theta \geq 41^\circ} \|\mathbf{s}(\theta)\mathbf{s}^\dagger(\theta) - \mathbf{s}(45^\circ)\mathbf{s}^\dagger(45^\circ)\|_F \approx 6.25.$$

3. *Extended diagonal loading method* [63,73,102] in Eq. (2.8) with the parameter

$$\epsilon = \max_{49^\circ \geq \theta \geq 41^\circ} \|\mathbf{s}(\theta) - \mathbf{s}(45^\circ)\| \approx 2.56.$$

4. *Directional LCMV* [96, 103] with three linear constraints which forces the responses of the signal from 41°, 45°, and 49° to be unity.

5. *First-order derivative LCMV*. Same as in Example 1.

6. *The standard MVDR beamformer* in Eq. (2.5).

The SINR of the MVDR beamformer with no mismatch is also displayed in the following figures. The results for SNR = 0dB are shown in Fig. 2.8, and the results for SNR = 10dB are shown in Fig. 2.9. One can observe that the standard MVDR beamformer is very sensitive to the arrival angle mismatch. It is more sensitive when the SNR is larger. Except the standard MVDR, these methods maintain steady SINRs while the mismatched angle $\theta - \theta_m$ varying. In this example, Algorithm 2 has the best SINR performance among these methods. Moreover, when there is no mismatch, the SINR of Algorithm 2 decreases slightly compared to the standard MVDR beamformer.

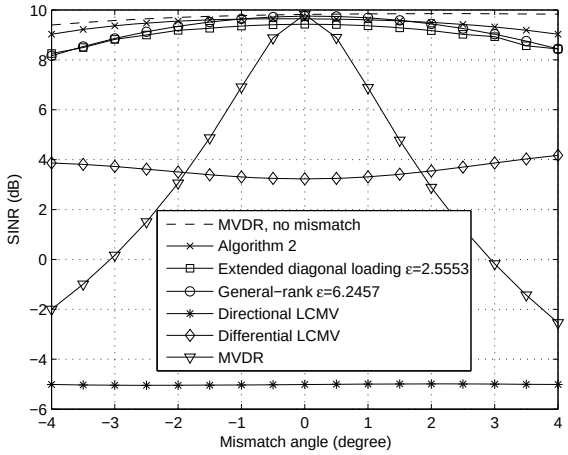

Figure 2.8: Example 3: SINR versus mismatch angle for SNR = 0dB

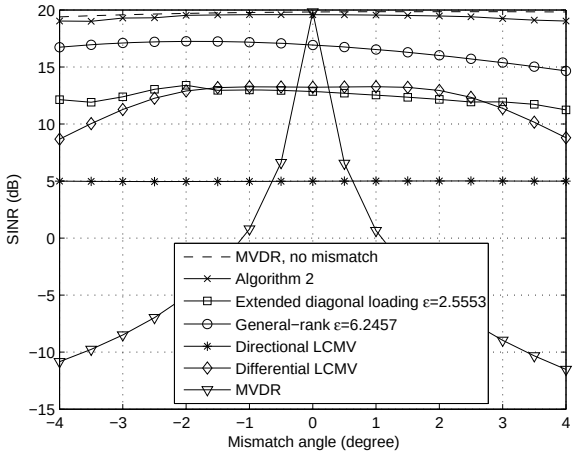

Figure 2.9: Example 3 continued: SINR versus mismatch angle for SNR = 10dB

Example 4: SINR versus N

In this example, the SINR is being compared for various number of antennas N. The actual angle of arrival θ is 43°, but the assumed angle of arrival θ_m is 45°. The following methods considered:

1. *Algorithm 2*. Same as in Example 2.

2. *General-rank method*. Same as in Example 2 except ϵ is now a function of N, and it can be expressed as

$$\epsilon(N) = \max_{48^\circ \geq \theta \geq 42^\circ} \|\mathbf{s}(\theta)\mathbf{s}^\dagger(\theta) - \mathbf{s}(45^\circ)\mathbf{s}^\dagger(45^\circ)\|_F.$$

3. *Extended diagonal loading method*. Same as in Example 2 except ϵ is now a function of N, and it can be expressed as

$$\epsilon(N) = \max_{48^\circ \geq \theta \geq 42^\circ} \|\mathbf{s}(\theta) - \mathbf{s}(45^\circ)\|.$$

4. *Three-point directional LCMV method*. Same as in Example 2.

5. *First order derivative LCMV*. Same as in Example 2.

6. *The standard MVDR beamformer* in Eq. (2.5).

The results for the case of SNR = 0dB and SNR = 10dB are shown in Fig. 2.10 and Fig. 2.11, respectively. One can observe that when there is no mismatch, the SINR performance of the MVDR

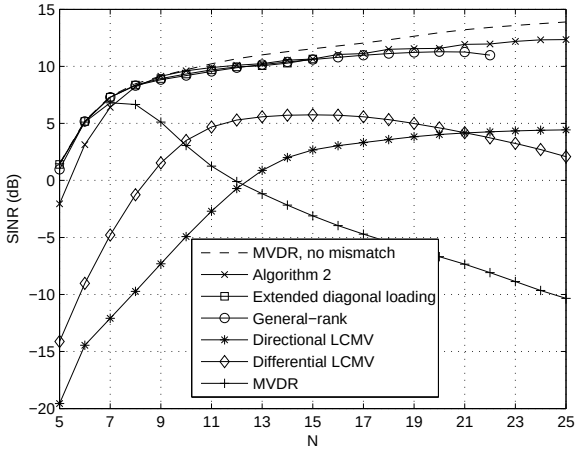

Figure 2.10: Example 4: SINR versus number of antennas for SNR = 0dB

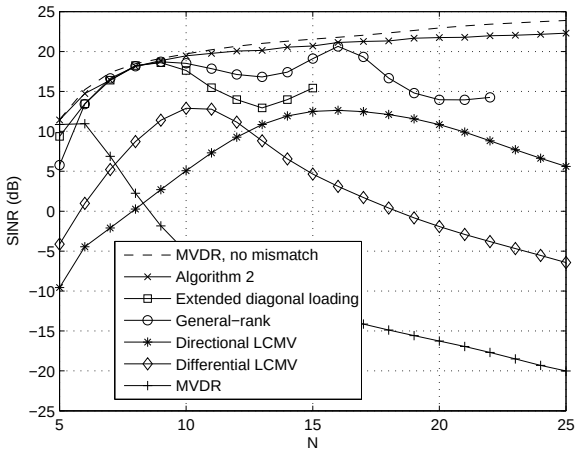

Figure 2.11: Example 4 continued: SINR versus number of antennas for SNR = 10dB

beamformer is an increasing function of the number of the antennas N, since the beamformer has a better ability to suppress the interferences and noise when N increases. However, for the MVDR beamformer with mismatch, the beamformer has a better ability to suppress the SOI as well as interferences when N increases. Therefore, the SINR of the MVDR beamformer increases at the beginning and then decays rapidly when N increases. For the general rank method, the SINRs when N is large than 22 is discarded because the corresponding ϵ are greater than $\|\mathbf{s}(\theta)\mathbf{s}^{\dagger}(\theta)\|_F$. For the same reason, the SINRs when N is larger than 15 are discarded in the extended diagonal loading method. Again, in this example, Algorithm 2 has a very good performance. Among all the robust beamformers, only Algorithm 2 has a nondecreasing SINR with respect to N. However, this does not mean there is no limitation on N for Algorithm 2. According to Lemma 1, the condition which guarantees the convergence of Algorithm 2 can be expressed as

$$|\sin(48^\circ) - \sin(42^\circ)| \approx .074 < \frac{\lambda}{Nd} = \frac{2}{N} \Rightarrow N \leq 27.$$

This means that if the number of antennas N is larger than 27, Algorithm 2 is not guaranteed to converge. In this example, Algorithm 2 fails to converge when $N = 28$.

Example 5: SINR versus number of snapshots

The covariance matrices $\mathbf{R_y}$ used in the previous examples are assumed to be perfect. In practice,

the covariance matrix can only be estimated. For example, we can use

$$\hat{\mathbf{R}}_{\mathbf{y}}(K) = \frac{1}{K}\sum_{k=1}^{K}\mathbf{y}(kT)\mathbf{y}^{\dagger}(kT),$$

where T is the sampling rate of the array, and K is the number of snapshots. The accuracy of the estimated covariance matrix $\hat{\mathbf{R}}_{\mathbf{y}}$ affects the SINR of the beamformer. In this example, the actual arrival angle is 43°, but the assumed arrival angle is 45°. The SINR are compared for different number of snapshots K. The following methods are considered:

1. *Algorithm 2* with $\theta_1 = 42^{\circ}$, $\theta_2 = 48^{\circ}$, $\zeta_1 = 43.5^{\circ}$, $\zeta_2 = 45^{\circ}$, $\zeta_3 = 46.5^{\circ}$, initial $\gamma = 10$ and step size $\alpha = 2$.

2. *General-rank method* [91] with $\epsilon \approx 4.73$ and $\gamma = 10$.

3. *Extended diagonal loading method* [63, 73, 102] with the parameter $\epsilon \approx 1.95$. Before using the algorithm in [63] to compute the diagonal loading level, the estimated covariance matrix is first modified by $\hat{\mathbf{R}}_{\mathbf{y}} \leftarrow \hat{\mathbf{R}}_{\mathbf{y}} + 10\mathbf{I}_{\mathbf{N}}$. In other words, an initial diagonal loading level $\gamma = 10$ is used.

4. *Three point directional LCMV*. Same in as Example 2 except a diagonal loading level $\gamma = 10$ is used.

5. *First-order derivative LCMV*. Same as in Example 2 except a diagonal loading level $\gamma = 10$ is used.

6. *Fixed diagonal loading* [1, 13] with $\gamma = 10$.

7. *The standard MVDR beamformer* in Eq. (2.5) with correct steering vector $\mathbf{s}(\theta)$.

All the methods above use the estimated covariance matrix $\hat{\mathbf{R}}_{\mathbf{y}}(K)$. Due to the fact that the finite-sample effect is considered, each method uses an appropriate diagonal loading level. The SINR of the MVDR beamformer, which uses correct steering vector $\mathbf{s}(\theta)$ and the perfect covariance matrix $\mathbf{R}_{\mathbf{y}}$, is used as an upper bound. In this example, noise $\mathbf{n}(kT)$ is generated according to the Gaussian distribution. The SINR is computed by using the averaged signal power and interference-plus-noise power over 1000 samples. The results are shown in Fig. 2.12 for SNR = 10dB. The MVDR beamformer without mismatch suffers from the finite-sample effect. Therefore the SINR is low

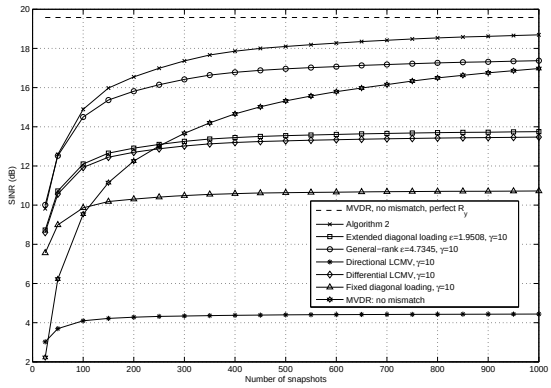

Figure 2.12: Example 5: SINR versus number of snapshots for SNR = 10dB

when the number of snapshots is small. For the fixed diagonal loading method, the SINR is relatively high when the number of snapshots is small. This shows that diagonal loading method is effective against finite-sample effect. However, SINR stops increasing after some number of snapshots because of the SOI steering vector mismatch. Again, Algorithm 2 has the best SINR performance for most situations. This shows that it is robust against both the finite-sample effect and the DOA mismatch.

The famous rapid convergence theorem proposed by Reed et al. in [86] states that a SINR loss of 3dB can be obtained by using the number of snapshots K equal to twice the number of antennas N. In this example, twice the number of antennas N is only 20. However this result is applicable only to the case where the samples are not contaminated by the target signal. Therefore it can not be applied in this example. One can see that in Fig. 2.12 the SINR requires more samples to converge because the sampled covariance matrices contain the target signal of 10dB. In [27], the authors have pointed out that the sample covariance matrix error is equivalent to the DOA error. Since our method is designed for robustness against DOA mismatch, it is also robust against finite-sample effect. However, it is not clear how to specify an appropriate uncertainty set to obtain the robustness against finite-sample effect. This problem will be explored in future work.

The SOI power can be estimated by the total output variance $\mathbf{w}^\dagger \hat{\mathbf{R}}_\mathbf{y} \mathbf{w}$. Fig. 2.13 shows the corresponding estimated SOI power. One can see that the estimated SOI power converges much faster than the SINR. The estimated SOI power represents the sum of signal and "interference + noise" power but the SINR represents the ratio of them. The reduction of the interference plus noise is subtle in the estimated SOI power because it only changes a small portion of the total variance.

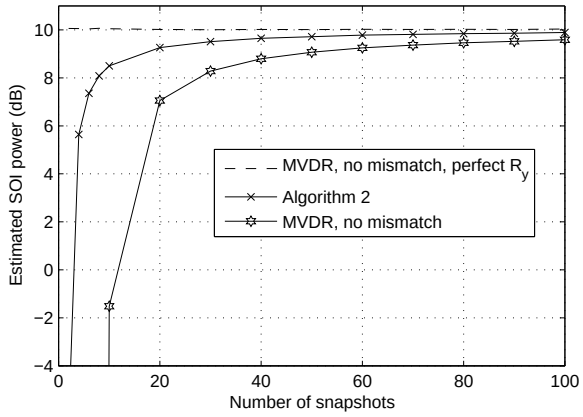

Figure 2.13: Estimated SOI power versus number of snapshots for SNR = 10dB

However, the reduction of the interference plus noise can cause a significant change in SINR. A change in interference plus noise does not affect the SOI as much as it affects the SINR. Therefore the estimated SOI power converges faster than the SINR.

Example 6: SINR versus SNR for general type mismatch

In the previous examples, we consider only the DOA mismatch. Although the proposed method is designed for solving only the DOA mismatch problem, in this example we consider a more general type of mismatch. In this example, the mismatched steering vector is modelled as

$$\mathbf{s}_m = \mathbf{s}(\theta) + \mathbf{e},$$

where $\mathbf{e}$ is a random vector with i.i.d. components $e_i \sim \mathcal{CN}(0, \sigma_e^2)$ for all i. In this example, σ_e^2 is chosen to be 0.01. The SINR in Eq. (2.2) are compared for different SNRs ranging from -20dB to 30dB. The SINR are calculated by the averaged energy over 1000 samples. All parameters are as in Example 2 except steering vector mismatch. The following methods are considered:

1. *Algorithm 2* with $\theta_1 = 41^\circ$, $\theta_2 = 49^\circ$, $\zeta_1 = 43^\circ$, $\zeta_2 = 45^\circ$, $\zeta_3 = 47^\circ$, initial $\gamma = 1$, and step size $\alpha = 2$.

2. *General-rank method*. Same as in Example 2 except ϵ is chosen to be $4N\sigma_e = 4$ to cover most of the steering vector error.

3. *Extended diagonal loading method*. Same as in Example 2 except ϵ is chosen to be $2N\sigma_e = 2$ to cover most of the steering vector error.

4. *Two-point directional LCMV.* Same as in Example 2.

5. *Three-point directional LCMV*. Same as in Example 2.

6. *First order derivative LCMV*. Same as in Example 2.

7. *Second order derivative LCMV*. Same as in Example 2.

8. *The standard MVDR beamformer* in Eq. (2.5).

Due to the fact that no finite-sample effect is considered, except in Algorithm 2 and extended diagonal loading method, no diagonal loading has been used in these methods. Again, the SINR of the MVDR beamformer without mismatch is also plotted as a benchmark. The results are shown in Fig. 2.14. The SINRs of the standard MVDR beamformer and all of the LCMV methods are seriously

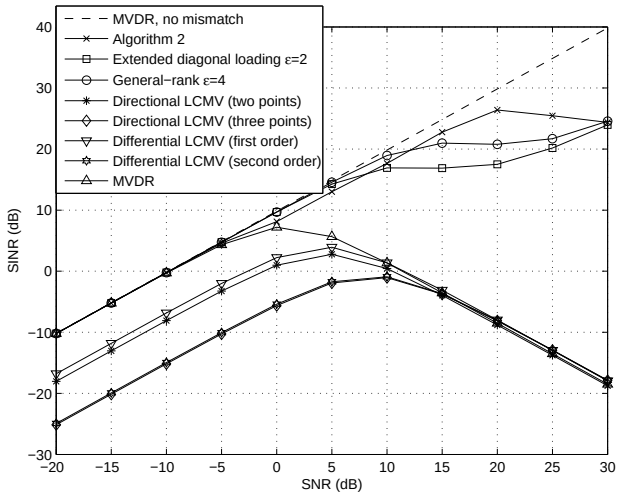

Figure 2.14: Example 6: SINR versus SNR for general type mismatch

degraded by this general type mismatch in the high SNR region. However, the proposed algorithm still has a good performance. As expected, the proposed algorithm has a worse performance than the extended diagonal loading method when SNR equals 0dB, 10dB, and 15dB because it is designed for robustness against DOA mismatch. The differences are about 1.5dB. Surprisingly, however, it has a better SINR performance in the high SNR region compared to other uncertainty based methods. The authors' conjecture is that these uncertainty based methods are based on worst-case,

however the SINR is obtained by averaging the energy. The worst-case design guarantees that *every time* the SOI is protected, however it dose not guarantee that *in average* the SINR performance is good. In the worst-case sense, the extended diagonal loading method [63, 73, 102] should be the best choice. Nevertheless this example shows that the proposed method has an unexpected good performance compared to the LCMV methods when general type of steering vector mismatches occur. We believe that the proposed algorithm is a good candidate for robust beamforming when DOA mismatch is dominant.

2.6 Conclusions

In this chapter, a new beamformer which is robust against DOA mismatch is introduced. This approach quadratically constrains the magnitude responses of two steering vectors and then uses a diagonal loading method to force the magnitude response at a range of arrival angles to exceed unity. Therefore this method can always force the gains at a desired range of angles to exceed a constant level while suppressing the interferences and noise. The analytic solution to the non-convex quadratically constrained minimization problem has been derived, and the diagonal loading factor γ can be determined by a simple iteration method proposed in Algorithm 2. This method is applicable to point source model where $\mathbf{s}(\theta)$ is known whenever θ is known. The complexity required in Algorithm 1 is approximately about the same as in the MVDR beamformer. The overall complexity depends on the number of iterations in Algorithm 2 which depends on the SNR. In our numerical examples, when SNR $<$ 10dB, the number of iterations is less than three. The numerical examples demonstrate that our approach has an excellent SINR performance under a wide range of conditions.

Chapter 3

Space-Time Adpative Processing for MIMO Radar

This chapter focuses on space-time adaptive processing (STAP) for MIMO radar systems which improves the spatial resolution for clutter. With a slight modification, STAP methods developed originally for the single-input multiple-output (SIMO) radar (phased array radar) can also be used in MIMO radar. However, in the MIMO radar, the rank of the jammer-and-clutter subspace becomes very large, especially the jammer subspace. It affects both the complexity and the convergence of the STAP algorithm. In this chapter, the clutter space and its rank in the MIMO radar are explored. By using the geometry of the problem rather than data, the clutter subspace can be represented using prolate spheroidal wave functions (PSWF). A new STAP algorithm is also proposed. It computes the clutter space using the PSWF and utilizes the block diagonal property of the jammer covariance matrix. Because of fully utilizing the geometry and the structure of the covariance matrix, the method has very good SINR performance and low computational complexity. Most of the results of this chapter have been reported in our recent journal paper [15].

3.1 Introduction

The adaptive techniques for processing the data from airborne antenna arrays are called space-time adaptive processing (STAP) techniques. The basic theory of STAP for the traditional single-input multiple-output (SIMO) radar has been well developed [44, 57]. There have been many algorithms proposed in [35, 40, 43–45, 57, 105] and the references therein for improving the complexity and convergence of the STAP in the SIMO radar. With a slight modification, these methods can also be applied to the MIMO radar case. The MIMO extension of STAP can be found in [7]. The MIMO

radar STAP for multipath clutter mitigation can be found in [75]. However, in the MIMO radar, the space-time adaptive processing (STAP) becomes even more challenging because of the extra dimension created by the orthogonal waveforms. On one hand, the extra dimension increases the rank of the jammer and clutter subspace, especially the jammer subspace. This makes the STAP more complex. On the other hand, the extra degrees of freedom created by the MIMO radar allows us to filter out more clutter subspace with little effect on SINR.

In this chapter, we explore the clutter subspace and its rank in MIMO radar. Using the geometry of the MIMO radar and the prolate spheroidal wave function (PSWF), a method for computing the clutter subspace is developed. Then we develop a STAP algorithm which computes the clutter subspace using the geometry of the problem rather than data and utilizes the block-diagonal structure of the jammer covariance matrix. Because of fully utilizing the geometry and the structure of the covariance matrix, our method has very good SINR performance and significantly lower computational complexity compared to fully adaptive methods (Sec. 3.4.2).

In practice, the clutter subspace might change because of effects such as the internal clutter motion (ICM), velocity misalignment, array manifold mismatch, and channel mismatch [44]. In this chapter, we consider an "ideal model", which does not take these effects into account. When this model is not valid, the performance of the algorithm will degrade. One way to overcome this might be to estimate the clutter subspace by using a combination of both the assumed geometry and the received data. Another way might be to develop a more robust algorithm against the clutter subspace mismatch. These ideas will be explored in the future.

The rest of the chapter is organized as follows. In Sec. 3.2, we formulate the STAP approach for MIMO radar. In Sec. 3.3, we explore the clutter subspace and its rank in the MIMO radar. Using prolate spheroidal wave functions (PSWF), we construct a data-independent basis for clutter signals. In Sec. 3.4, we propose a new STAP method for MIMO radar. This method utilizes the technique proposed in Sec. 3.3 to find the clutter subspace and estimates the jammer-plus-noise covariance matrix separately. Finally, the beamformer is calculated by using matrix inversion lemma. As we will see later, this method has very satisfactory SINR performance. In Sec. 3.5, we compare the SINR performance of different STAP methods based on numerical simulations. Finally, Sec. 3.6 concludes the chapter.

3.2 STAP in MIMO Radar

In this section, we formulate the STAP problem in MIMO radar. The MIMO extension for STAP first appeared in [7]. We will focus on the idea of using the extra degrees of freedom to increase the spatial resolution for clutter.

3.2.1 Signal Model

Fig. 3.1 shows the geometry of the MIMO radar STAP with uniform linear arrays (ULA), where

1. d_T is the spacing of the transmitting antennas,
2. d_R is the spacing of the receiver antennas,
3. M is the number of transmitting antennas,
4. N is the number of the receiving antennas,
5. T is the radar pulse period,
6. l indicates the index of radar pulse (slow time),
7. τ represents the time within the pulse (fast time),
8. v_t is the target speed toward the radar station, and
9. v is the speed of the radar station.

Notice that the model assumes the two antenna arrays are linear and parallel. The transmitter and the receiver are close enough so that they share the same angle variable θ. The radar station movement is assumed to be parallel to the linear antenna array. This assumption has been made in most of the airborne ground moving target indicator (GMTI) systems. Each array is composed of omnidirectional elements. The transmitted signals of the mth antenna can be expressed as

$$x_m(lT+\tau) = \sqrt{E}\phi_m(\tau)e^{j2\pi f(lT+\tau)},$$

for $m = 1, 2, \cdots, M-1$, where $\phi_m(\tau)$ is the baseband pulse waveform, f is the carrier frequency, and E is the transmitted energy for the pulse. The demodulated received signal of the nth antenna

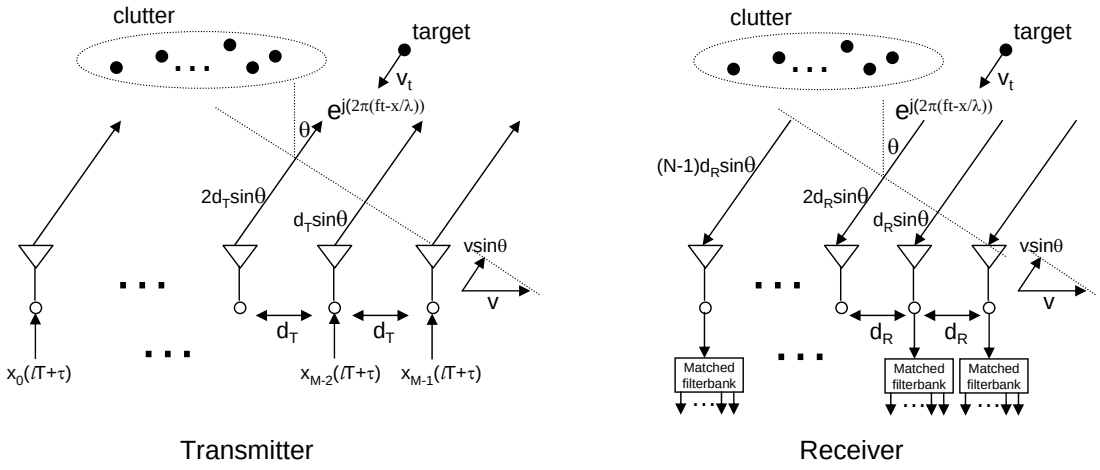

Figure 3.1: This figure illustrates a MIMO radar system with M transmitting antennas and N receiving antennas. The radar station is moving with speed v

can be expressed as

$$
\begin{aligned}
& y_n(lT+\tau+\frac{2r}{c}) \approx \\
& \sum_{m=0}^{M-1} \rho_t \phi_m(\tau) e^{j\frac{2\pi}{\lambda}(\sin\theta_t(2vTl+d_Rn+d_Tm)+2v_tTl)} \\
& + \sum_{i=0}^{N_c-1}\sum_{m=0}^{M-1} \rho_i \phi_m(\tau) e^{j\frac{2\pi}{\lambda}(\sin\theta_i(2vTl+d_Rn+d_Tm))} \\
& + y_n^{(J)}(lT+\tau+\frac{2r}{c}) + y_n^{(w)}(lT+\tau+\frac{2r}{c}),
\end{aligned} \tag{3.1}
$$

where

1. r is the distance of the range bin of interest,
2. c is the speed of light,
3. ρ_t is the amplitude of the signal reflected by the target,
4. ρ_i is the amplitude of the signal reflected by the ith clutter,
5. θ_t is the looking direction of the target,
6. θ_i is the looking direction of the ith clutter,
7. N_c is the number of clutter signals,
8. $y_n^{(J)}$ is the jammer signal in the nth antenna output, and

9. $y_n^{(w)}$ is the white noise in the nth antenna output.

For convenience, all of the parameters used in the signal model are summarized in Table 3.1. The

Table 3.1: List of the parameters used in the signal model

d_T	spacing of the transmitting antennas
d_R	spacing of the receiving antennas
M	number of the transmitting antennas
N	number of the receiving antennas
T	radar pulse period
l	index of radar pulse (slow time)
τ	time within the pulse (fast time)
v_t	target speed toward the radar station
x_m	transmitted signal in the mth antenna
ϕ_m	baseband pulse waveforms
y_n	demodulated received signal in the nth antenna
v_t	target speed toward the radar station
v	speed of the radar station
r	distance of the range bin of interest
c	speed of light
ρ_t	amplitude of the signal reflected by the target
ρ_i	amplitude of the signal reflected by the ith clutter
θ_t	looking direction of the target
θ_i	looking direction of the ith clutter
N_c	number of clutter signals
$y_n^{(J)}$	jammer signal in the nth antenna output
$y_n^{(w)}$	white noise in the nth antenna output

first term in (3.1) represents the signal reflected by the target. The second term is the signal reflected by the clutter. The last two terms represent the jammer signal and white noise. We assume there is no internal clutter motion (ICM) or antenna array misalignment [44]. The phase differences in the reflected signals are caused by the Doppler shift, the differences of the receiving antenna locations, and the differences of the transmitting antenna locations. In the MIMO radar, the transmitting waveforms $\phi_m(\tau)$ satisfy orthogonality:

$$\int \phi_m(\tau)\phi_k^*(\tau)d\tau = \delta_{mk}. \tag{3.2}$$

The sufficient statistics can be extracted by a bank of matched filters as shown in Fig. 3.1. The extracted signals can be expressed as

$$\begin{aligned} & y_{n,m,l} \triangleq \int y_n(lT+\tau+\frac{2r}{c})\phi_m^*(\tau)d\tau = \\ & \rho_t e^{j\frac{2\pi}{\lambda}(\sin\theta_t(2vTl+d_Rn+d_Tm)+2v_tTl)} + \\ & \sum_{i=0}^{N_c-1}\rho_i e^{j\frac{2\pi}{\lambda}(\sin\theta_i(2vTl+d_Rn+d_Tm))} + y_{n,m,l}^{(J)} + y_{n,m,l}^{(w)}, \end{aligned} \tag{3.3}$$

for $n = 0, 1, \cdots, N-1$, $m = 0, 1, \cdots, M-1$, and $l = 0, 1, \cdots, L-1$, where $y_{n,m,l}^{(J)}$ is the corresponding jammer signal, $y_{n,m,l}^{(w)}$ is the corresponding white noise, and L is the number of the pulses in a coherent processing interval (CPI). To simplify the above equation, we define the following normalized spatial and Doppler frequencies:

$$\begin{aligned} f_s &\triangleq \frac{d_R}{\lambda}\sin\theta_t,\ f_{s,i} \triangleq \frac{d_R}{\lambda}\sin\theta_i \\ f_D &\triangleq \frac{2(v\sin\theta_t + v_t)}{\lambda}T. \end{aligned} \tag{3.4}$$

One can observe that the normalized Doppler frequency of the target is a function of both target looking direction and speed. Throughout this chapter we shall make the assumption $d_R = \lambda/2$ so that spatial aliasing is avoided. Using the above definition we can rewrite the extracted signal in (3.3) as

$$\begin{aligned} y_{n,m,l} &= \rho_t e^{j2\pi f_s(n+\gamma m)}e^{j2\pi f_D l} + \\ & \sum_{i=0}^{Nc-1}\rho_i e^{j2\pi f_{s,i}(n+\gamma m+\beta l)} + y_{n,m,l}^{(J)} + y_{n,m,l}^{(w)}, \end{aligned} \tag{3.5}$$

for $n = 0, 1, \cdots, N-1$, $m = 0, 1, \cdots, M-1$, and $l = 0, 1, \cdots, L-1$, where

$$\gamma \triangleq d_T/d_R, \text{ and } \beta \triangleq 2vT/d_R. \tag{3.6}$$

3.2.2 Fully Adaptive MIMO-STAP

The goal of space-time adaptive processing (STAP) is to find a linear combination of the extracted signals so that the SINR can be maximized. Thus the target signal can be extracted from the interferences, clutter, and noise to perform the detection. Stacking the MIMO STAP signals in (3.5), we

obtain the NML vector

$$\mathbf{y} = \begin{pmatrix} y_{0,0,0} & y_{1,0,0} & \cdots & y_{N-1,M-1,L-1} \end{pmatrix}^T. \tag{3.7}$$

Then the linear combination can be expressed as $\mathbf{w}^\dagger\mathbf{y}$, where $\mathbf{w}$ is the weight vector for the linear combination. The SINR maximization can be obtained by minimizing the total variance under the constraint that the target response is unity. It can be expressed as the following optimization problem:

$$\begin{aligned} &\min_{\mathbf{w}} \mathbf{w}^\dagger\mathbf{R}\mathbf{w} \\ &\text{subject to } \mathbf{w}^\dagger\mathbf{s}(f_s, f_D) = 1, \end{aligned} \tag{3.8}$$

where $\mathbf{R} \triangleq E[\mathbf{y}\mathbf{y}^\dagger]$, and $\mathbf{s}(f_s, f_D)$ is the size-NML MIMO space-time steering vector which consists of the elements

$$e^{j2\pi f_s(n+\gamma m)} e^{j2\pi f_D l}, \tag{3.9}$$

for $n = 0, 1, \cdots, N-1$, $m = 0, 1, \cdots, M-1$, and $l = 0, 1, \cdots, L-1$. This $\mathbf{w}$ is called minimum variance distortionless response (MVDR) beamformer [12]. The covariance matrix $\mathbf{R}$ can be estimated by using the neighboring range bin cells. In practice, in order to prevent self-nulling, a target-free covariance matrix can be estimated by using guard cells [44]. The well-known solution to the above problem is [12]

$$\mathbf{w} = \frac{\mathbf{R}^{-1}\mathbf{s}(f_s, f_D)}{\mathbf{s}(f_s, f_D)^\dagger\mathbf{R}^{-1}\mathbf{s}(f_s, f_D)}. \tag{3.10}$$

However, the covariance matrix $\mathbf{R}$ is $NML \times NML$. It is much larger than in the SIMO case because of the extra dimension. The complexity of the inversion of such a large matrix is high. The estimation of such a large covariance matrix also converges slowly. To overcome these problems, partially adaptive techniques can be applied. The methods described in Sec. 3.5 are examples of such partially adaptive techniques. In SIMO radar literature such partially adaptive methods are commonly used [44, 57].

3.2.3 Comparison with SIMO System

In the traditional transmit beamforming, or single-input-multiple-output (SIMO) radar, the transmitted waveforms are coherent and can be expressed as

$$\phi_m(\tau) = \phi(\tau) w_{Tm}$$

for $m = 1, 2, \cdots, M-1$, where $\{w_{Tm}\}$ are the transmit beamforming weights. The sufficient statistics can be extracted by a single matched filter for every receiving antenna. The extracted signal can be expressed as

$$\begin{aligned} y_{n,l} &\triangleq \int y_n(lT + \tau + \frac{2r}{c}) \phi^*(\tau) d\tau = \\ &\rho_t e^{j2\pi f_s n} e^{j2\pi f_D l} \sum_{m=0}^{M-1} w_{Tm} e^{j2\pi f_s \gamma m} + \\ &\sum_{i=0}^{N_c-1} \rho_i e^{j2\pi f_{s,i}(n+\beta l)} \sum_{m=0}^{M-1} w_{Tm} e^{j2\pi f_{s,i} \gamma m} + y^J_{n,l} + y^{(w)}_{n,l}, \end{aligned} \tag{3.11}$$

for $n = 0, 1, \cdots, N-1$, and $l = 0, 1, \cdots, L-1$, where $y^{(J)}_{n,l}$ is the corresponding jammer signal, and $y^{(w)}_{n,l}$ is the corresponding white noise. Comparing the MIMO signals in (3.5) and the SIMO signals in (3.11), one can see that a linear combination with respect to m has been performed on the SIMO signal in the target term and the clutter term. The MIMO radar, however, leaves all degrees of freedom to the receiver. Note that in the receiver, one can perform the same linear combination with respect to m on the MIMO signal in (3.5) to create the SIMO signal in (3.11). The only difference is that the transmitting power for the SIMO signal is less because of the focused beam used in the transmitter. For the SIMO radar, the number of degrees of freedom is M in the transmitter and NL in the receiver. The total number of degrees of freedom is $M + NL$. However, for the MIMO radar, the number of degrees of freedom is NML which is much larger than $M + NL$. These extra degrees of freedom can be used to obtain a better spatial resolution for clutter.

The MIMO radar transmits omnidirectional orthogonal waveforms from each antenna element. Therefore it illuminates all angles. The benefit of SIMO radar is that it transmits focused beams which saves transmitting power. Therefore, for a particular angle of interest, the SIMO radar enjoys a processing gain of M compared to the MIMO radar. However, for some applications like scanning or imaging, it is necessary to illuminate all angles. In this case, the benefit of a focused beam no

longer exists because both systems need to consume the same energy for illuminating all angles. The SIMO system will need to steer the focused transmit beam to illuminate all angles.

A second point is that for the computation of the MIMO beamformer in (3.10), the matrix inversion $\mathbf{R}^{-1}$ needs to be computed only once and it can be applied for all angles. The transmitting array in a MIMO radar does not have a focused beam. So, all the ground points within a range bin are uniformly illuminated. The clutter covariance seen by the receiving antenna array is, therefore, the same for all angles. In the SIMO case, the matrix inversions need to be computed for different angles because the clutter signal changes as the beam is steered through all angles.

3.2.4 Virtual Array

Observing the MIMO space-time steering vector defined in (3.9), one can view the first term $e^{j2\pi f_s(n+\gamma m)}$ as a sampled version of the sinusoidal function $e^{j2\pi f_s x}$. Recall that γ is defined in (3.5) as the ratio of the antenna spacing of the transmitter and receiver. To obtain a good spatial frequency resolution, these signals should be critically sampled and have long enough duration. One can choose $\gamma = N$ because it maximizes the time duration while maintaining critical sampling [7] as shown in Fig. 3.1. Sorting the sample points $n + \gamma m$ for $n = 0, 1, \cdots, N-1$, and $m = 0, 1, \cdots, M-1$, we obtain the sorted sample points $k = 0, 1, \cdots, NM-1$. Thus the target response in (3.9) can be rewritten as

$$e^{j2\pi f_s k} e^{j2\pi f_D l}$$

for $k = 0, 1, \cdots, NM-1$, and $l = 0, 1, \cdots, L-1$. It is as if we have a virtual receiving array with NM antennas. However, the resolution is actually obtained by only M antennas in the transmitter and N antennas in the receiver. Fig. 3.2 compares the SINR performance of the MIMO system and the SIMO system in the array looking direction of zero degree, that is, $f_s = 0$. The optimal space-time beamformer described in (3.10) is used. The parameter L equals 16, and β equals 1.5 in this example. In all plots it is assumed that the energy transmitted by any single antenna element to illuminate all angles is fixed. The SINR drops near zero Doppler frequency because it is not easy to distinguish the slowly moving target from the still ground clutter. The MIMO system with $\gamma = 1$ has a slightly better performance than the SIMO system with the same antenna structure. For the virtual array structure where $\gamma = N$, the MIMO system has a very good SINR performance and it is close to the performance of the SIMO system with NM antennas because they have the same

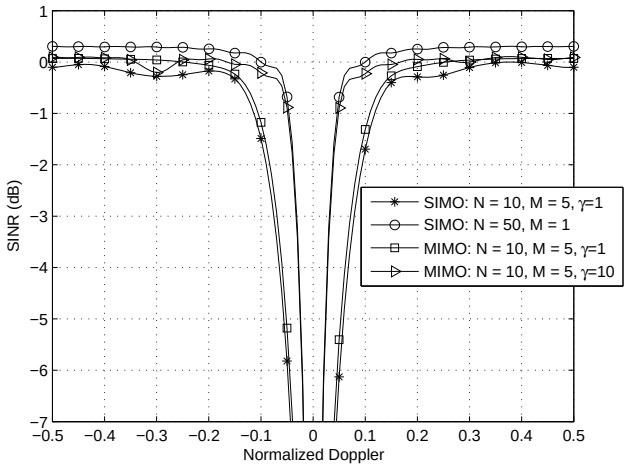

Figure 3.2: The SINR at looking direction zero as a function of the Doppler frequencies for different SIMO and MIMO systems

resolution for the target signal and the clutter signals. The small difference comes from the fact that the SIMO system with NM antennas has a better spatial resolution for the jammer signals. This example shows that the choice of γ is very crucial in the MIMO radar. With the choice $\gamma = 10 = N$, the MIMO radar with only 15 antenna elements has about the same performance as the SIMO radar with 51 array elements. This example also shows that the MIMO radar system has a much better spatial resolution for clutter compared to the traditional SIMO system with same number of physical antenna elements.

3.3 Clutter Subspace in MIMO Radar

In this section, we explore the clutter subspace and its rank in the MIMO radar system. The covariance matrix $\mathbf{R}$ in (3.8) can be expressed as $\mathbf{R} = \mathbf{R}_t + \mathbf{R}_c + \mathbf{R}_J + \sigma^2\mathbf{I}$, where $\mathbf{R}_t$ is the covariance matrix of the target signal, $\mathbf{R}_c$ is the covariance matrix of the clutter, $\mathbf{R}_J$ is the covariance matrix of the jammer, and σ^2 is the variance of the white noise. The clutter subspace is defined as the range space of $\mathbf{R}_c$ and the clutter rank is defined as the rank of $\mathbf{R}_c$. In the space-time adaptive processing (STAP) literature, it is a well-known fact that the clutter subspace usually has a small rank. It was first pointed out by Klemm in [55], that the clutter rank is approximately $N + L$, where N is the number of receiving antennas and L is the number of pulses in a coherent processing interval (CPI). In [104] and [10], a rule for estimating the clutter rank was proposed. The estimated rank is

approximately

$$N + \beta(L-1), \tag{3.12}$$

where $\beta = 2vT/d_R$. This is called Brennan's rule. In [42], this rule has been extended to the case with arbitrary arrays. Taking advantage of the low rank property, the STAP can be performed in a lower dimensional space so that the complexity and the convergence can be significantly improved [35, 40, 43–45, 56, 57, 105]. This result will now be extended to the MIMO radar. These techniques are often called *partially adaptive methods* or *subspace methods*.

3.3.1 Clutter Rank in MIMO Radar

We first study the clutter term in (3.5) which is expressed as

$$y^{(c)}_{n,m,l} = \sum_{i=0}^{Nc-1} \rho_i e^{j2\pi f_{s,i}(n+\gamma m+\beta l)},$$

for $n = 0, 1, \cdots, N-1$, $m = 0, 1, \cdots, M-1$, and $l = 0, 1, \cdots, L-1$. Note that $-0.5 < f_{s,i} < 0.5$ because $d_R = \lambda/2$. Define $c_{i,n,m,l} = e^{j2\pi f_{s,i}(n+\gamma m+\beta l)}$ and

$$\mathbf{c}_i = \left(\; c_{i,0,0,0}, c_{i,1,0,0}, \cdots, c_{i,N-1,M-1,L-1} \; \right)^T. \tag{3.13}$$

By stacking the signals $\{y^{(c)}_{n,m,l}\}$ into a vector, one can obtain

$$\mathbf{y}^{(c)} = \sum_{i=0}^{N_c-1} \rho_i \mathbf{c}_i.$$

Assume that ρ_i are zero-mean independent random variables with variance $\sigma^2_{c,i}$. The clutter covariance matrix can be expressed as

$$\mathbf{R}_c = E[\mathbf{y}^{(c)}\mathbf{y}^{(c)\dagger}] = \sum_{i=0}^{N_c-1} \sigma^2_{c,i}\mathbf{c}_i\mathbf{c}_i^\dagger.$$

Therefore, $\text{span}(\mathbf{R}_c) = \text{span}(\mathbf{C})$, where

$$\mathbf{C} \triangleq \left(\; \mathbf{c}_0, \mathbf{c}_1, \cdots, \mathbf{c}_{N_c-1} \; \right).$$

The vector $\mathbf{c}_i$ consists of the samples of $e^{j2\pi f_{s,i}x}$ at points $\{n+\gamma m+\beta l\}$, where γ and β are defined in (3.6). In general, $\mathbf{c}_i$ is a *nonuniformly* sampled version of the bandlimited sinusoidal waveform $e^{j2\pi f_{s,i}x}$. If γ and β are both integers, the sampled points $\{n+\gamma m+\beta l\}$ can only be integers in

$$\{0, 1, \cdots, N+\gamma(M-1)+\beta(L-1)\}.$$

If $N+\gamma(M-1)+\beta(L-1) \leq NML$, there will be repetitions in the sample points. In other words, some of the row vectors in $\mathbf{C}$ will be exactly the same and there will be at most $N+\gamma(M-1)+\beta(L-1)$ distinct row vectors in $\mathbf{C}$. Therefore the rank of $\mathbf{C}$ is less than $N+\gamma(M-1)+\beta(L-1)$. So is the rank of $\mathbf{R}_c$. We summarize this fact as the following theorem:

Theorem 1 *If γ and β are both integers, then rank*$(\mathbf{R}_c) \leq$ *min*$(N+\gamma(M-1)+\beta(L-1), N_c, NML)$.♦♦♦

Usually N_c and NML are much larger than $N+\gamma(M-1)+\beta(L-1)$. Therefore $N+\gamma(M-1)+\beta(L-1)$ is a good estimation of the clutter rank. This result can be viewed as an extension of Brennan's rule [104], given in (3.12), to the MIMO radar case.

Now we focus on the general case where γ and β are real numbers. The vector $\mathbf{c}_i$ in (3.13) can be viewed as a nonuniformly sampled version of the truncated sinusoidal function

$$c(x; f_{s,i}) \triangleq \begin{cases} e^{j2\pi f_{s,i}x}, & 0 \leq x \leq X \\ 0, & \text{otherwise,} \end{cases} \tag{3.14}$$

where $X \triangleq N-1+\gamma(M-1)+\beta(L-1)$. Furthermore, $-0.5 \leq f_{s,i} \leq 0.5$ because d_R is often selected as $\lambda/2$ in (3.4) to avoid aliasing. Therefore, the energy of these signals is mostly confined to a certain time-frequency region. Fig. 3.3 shows an example of such a signal. Such signals can be well approximated by linear combinations of $\lceil 2WX+1 \rceil$ orthogonal functions [93], where W is the one sided bandwidth and X is the duration of the time-limited functions. In the next section, more details on this will be discussed using prolate spheroidal wave functions (PSWF). In this case, we have $W=0.5$ and $2WX+1 = N+\gamma(M-1)+\beta(L-1)$. The vectors $\mathbf{c}_i$ can be also approximated by a linear combination of the nonuniformly sampled versions of these $\lceil N+\gamma(M-1)+\beta(L-1) \rceil$ orthogonal functions. Thus, in the case where γ and β are nonintegers, we can conclude that only $\lceil N+\gamma(M-1)+\beta(L-1) \rceil$ eigenvalues of the matrix $\mathbf{R}_c$ are significant. In other words,

$$\text{rank}(\mathbf{R}_c) \approx \lceil N+\gamma(M-1)+\beta(L-1) \rceil. \tag{3.15}$$

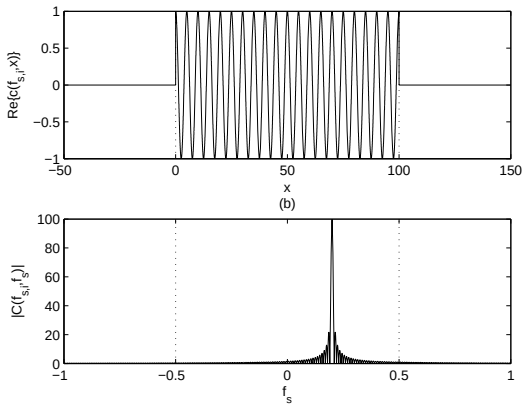

Figure 3.3: Example of the signal $c(x; f_{s,i})$. (a) Real part. (b) Magnitude response of Fourier transform

Note that the definition of this approximate rank is actually the number of the dominant eigenvalues. This notation has been widely used in the STAP literature [44, 57]. In the SIMO radar case, using Brennan's rule, the ratio of the clutter rank and the total dimension of the space-time steering vector can be approximated as

$$\frac{N+\beta(L-1)}{NL} = \frac{1}{L} + \frac{\beta(L-1)}{NL}.$$

In the MIMO radar case with $\gamma = N$, the corresponding ratio becomes

$$\frac{N+N(M-1)+\beta(L-1)}{NML} = \frac{1}{L} + \frac{\beta(L-1)}{NML}.$$

One can observe that the clutter rank now becomes a smaller portion of the total dimension because of the extra dimension introduced by the MIMO radar. *Thus the MIMO radar receiver can null out the clutter subspace with little effect on SINR.* Therefore a better spatial resolution for clutter can be obtained.

The result can be further generalized for the array with arbitrary linear antenna deployment. Let $x_{T,m}, m = 0, 1, \cdots, M-1$ be the transmitting antenna locations, $x_{R,n}, n = 0, 1, \cdots, N-1$ be the receiving antenna locations, and v be the speed of the radar station. Without loss of generality, we set $x_{T,0} = 0$ and $x_{R,0} = 0$. Then the clutter signals can be expressed as

$$y^{(c)}_{n,m,l} = \sum_{i=0}^{N_c-1} \rho_i e^{j\frac{2\pi}{\lambda}\sin\theta_i((x_{R,n}+x_{T,m}+2vTl))},$$

for $n = 0, 1, \cdots, N-1$, $m = 0, 1, \cdots, M-1$, and $l = 0, 1, \cdots, L-1$, where θ_i is the looking-direction of the ith clutter. The term

$$e^{j\frac{2\pi}{\lambda}\sin\theta_i(x_{R,n}+x_{T,m}+2vTl)}$$

can also be viewed as a nonuniform sampled version of the function $e^{j\frac{2\pi}{\lambda}\sin\theta_i x}$. Using the same argument we have made in the uniform linear array (ULA) case, one can obtain

$$\text{rank}(\mathbf{R}_c) \quad \approx \quad \lceil 1 + \frac{2}{\lambda}(x_{R,N-1} + x_{T,M-1} + 2vT(L-1))\rceil.$$

The quantity $x_{R,N-1} + x_{T,M-1} + 2vT(L-1)$ can be regarded as the total aperture of the space-time virtual array. One can see that the number of dominant eigenvalues is proportional to the ratio of the total aperture of the space-time virtual array and the wavelength.

3.3.2 Data Independent Estimation of the Clutter Subspace with PSWF

The clutter rank can be estimated by using (3.15) and the parameters N, M, L, β and γ. However, the clutter subspace is often estimated by using data samples instead of using these parameters [35,40,43–45,56,57,105]. In this section, we propose a method which estimates the clutter subspace using the geometry of the problem rather than the received signal. The main advantage of this method is that it is data independent. The clutter subspace obtained by this method can be used to improve the convergence of the STAP. Experiments also show that the estimated subspace is very accurate in the ideal case (without ICM and array misalignment).

In Fig. 3.3, one can see that the signal in (3.14) is time-limited and most of its energy is concentrated on $-0.5 \le f_s \le 0.5$. To approximate the subspace which contains such signals, we find the basis functions which are time-limited and concentrate their energy on the corresponding bandwidth. Such basis functions are the solutions of the following integral equation [93]

$$\mu\psi(x) = \int_0^X \text{sinc}(2W(x-\zeta))\psi(\zeta)d\zeta,$$

where $\text{sinc}(x) \triangleq \frac{\sin\pi x}{\pi x}$ and μ is a scalar to be solved. This integral equation has infinite number of solutions $\psi_i(x)$ and μ_i for $i = 0, 1, \cdots, \infty$. The solution $\psi_i(x)$ is called prolate spheroidal wave

function (PSWF). By the maximum principle [50], the solution satisfies

$$\psi_0(x) = \arg\max_{\|\psi\|=1} \int_0^X \int_0^X \psi^*(x)\text{sinc}(2W(x-\zeta))\psi(\zeta)d\zeta dx$$
$$\psi_i(x) = \arg\max_{\|\psi\|=1} \int_0^X \int_0^X \psi^*(x)\text{sinc}(2W(x-\zeta))\psi(\zeta)d\zeta dx$$
$$\text{subject to } \int_0^X \psi(x)\psi_k^*(x)dx = 0, \text{ for } k = 0, 1, \cdots, i-1,$$

for $i = 1, 2, \cdots, \infty$. The function $\psi_i(x)$ is orthogonal to the previous basis components $\psi_k(x)$, for $k < i$ while concentrating most of its energy on the bandwidth $[-W, W]$. Moreover, only the first $\lceil 2WX + 1 \rceil$ eigenvalues μ_i are significant [93]. Therefore, the time-band-limited function $c(x; f_{s,i})$ in (3.14) can be well approximated by linear combinations of $\psi_i(x)$ for $i = 0, 1, \cdots, \lceil 2WX + 1 \rceil$. In this case, $W = 0.5$ and $2WX + 1 = N + \gamma(M-1) + \beta(L-1)$. Thus the nonuniformly sampled versions of $c(x; f_{s,i})$, namely $c_{i,n,m,l}$, can be approximated by the linear combination:

$$c_{i,n,m,l} \triangleq e^{j2\pi f_{s,i}(n+\gamma m+\beta l)} \approx \sum_{k=0}^{r_c-1} \alpha_{i,k}\psi_k(n+\gamma m+\beta l),$$

for some $\{\alpha_{i,k}\}$ where

$$r_c \triangleq \lceil N + \gamma(M-1) + \beta(L-1) \rceil. \tag{3.16}$$

Stacking the above elements into vectors, we have

$$\mathbf{c}_i \approx \sum_{k=0}^{r_c-1} \alpha_{i,k}\mathbf{u}_k,$$

where $\mathbf{u}_k$ is a vector which consists of the elements $\psi_k(n+\gamma m+\beta l)$. Finally, we have

$$\text{span}(\mathbf{R}_c) = \text{span}(\mathbf{C}) \approx \text{span}(\mathbf{U}_c), \tag{3.17}$$

where $\mathbf{U}_c \triangleq \begin{pmatrix} \mathbf{u}_0 & \mathbf{u}_1 & \cdots & \mathbf{u}_{r_c-1} \end{pmatrix}$. Note that although the functions $\{\psi_k(x)\}$ are orthogonal, the vectors $\{\mathbf{u}_k\}$ are in general not orthogonal. This is because of the fact that $\{\mathbf{u}_k\}$ are obtained by nonuniform sampling which destroys orthogonality. In practice, the PSWF $\psi_i(x)$ can be computed off-line and stored in the memory. When the parameters change, one can obtain the vectors $\mathbf{u}_k$ by resampling the PSWF $\psi_k(n+\gamma m+\beta l)$ to form the new clutter subspace. In this way, we can obtain

the clutter subspace by using the geometry of the problem.

Performing the Gram-Schmidt procedure on the basis $\{\mathbf{u}_k\}$, we obtain the orthonormal basis $\{\mathbf{q}_k\}$. The clutter power in each orthonormal basis element can be expressed as $\mathbf{q}_k^\dagger \mathbf{R}_c \mathbf{q}_k$. Fig. 3.4 shows the clutter power in the orthogonalized basis elements. In this example, $N = 10$, $M = 5$,

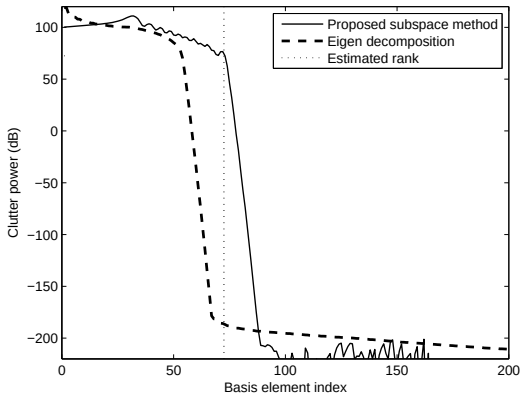

Figure 3.4: Plot of the clutter power distributed in each of the orthogonal basis elements

$L = 16$, $\gamma = 10$, and $\beta = 1.5$. Note that there are a total of $NML = 800$ basis elements but we only show the first 200 on the plot. The clutter covariance matrix $\mathbf{R}_c$ is generated using the model described in [42]. The eigenvalues of $\mathbf{R}_c$ are also shown in Fig. 3.4 for comparison. The estimated clutter rank is $\lceil N + \gamma(M-1) + \beta(L-1) \rceil = 73$. One can see that the subspace obtained by the proposed method captures almost all clutter power. The clutter power decays to less than -200 dB for the basis index exceeding 90.

Compared to the eigen decomposition method, the subspace obtained by our method is larger. This is because of the fact that the clutter spatial bandwidth has been overestimated in this example. More specifically, we have assumed the worst case situation that the clutter spatial frequencies range from -0.5 to 0.5. In actual fact however, the range is only from -0.35 to 0.35. This comes about because of the specific geometry assumed in this example: the altitude is 9km, the range of interest is 12.728km, and a flat ground model is used. Therefore the rank of the subspace is overestimated. It may seem that our method loses some efficiency compared to the eigen decomposition. However, note that the eigen decomposition requires perfect information of the clutter covariance matrix $\mathbf{R}_c$ while our method requires no data. In this example, we assume the perfect $\mathbf{R}_c$ is known. In practice, $\mathbf{R}_c$ has to be estimated from the received signals and it might not be accurate if the number of samples is not large enough. Note that, unlike the eigen decomposition method, the

proposed method based on PSWF does not require the knowledge of $\mathbf{R}_c$.

3.4 New STAP Method for MIMO Radar

In this section, we introduce a new STAP method for MIMO radar which uses the clutter subspace estimation method described in the last section. Because the clutter subspace can be obtained by using the parameter information, the performance and complexity can both be improved. Recall that the optimal MVDR beamformer (3.10) requires knowledge of the covariance matrix $\mathbf{R}$. In practice, this has to be estimated from data. For example, it can be estimated as

$$\hat{\mathbf{R}} = \frac{1}{|\mathcal{B}|} \sum_{k \in \mathcal{B}} \mathbf{y}_k \mathbf{y}_k^\dagger, \tag{3.18}$$

where $\mathbf{y}_k$ is the MIMO-STAP signal vector defined in (3.7) for the kth range bin, and $\mathcal{B}$ is a set which contains the neighbor range bin cells of the range bin of interest. However, some nearest cells around the range bin of interest are excluded from $\mathcal{B}$ in order to avoid including the target signals [44]. There are two advantages of using the target-free covariance matrix $\mathbf{R}$ in (3.10). First, it is more robust to steering vector mismatch. If there is mismatch in the steering vector $\mathbf{s}(f_s, f_D)$ in (3.8), the target signal is no longer protected by the constraint. Therefore the target signal is suppressed as interference. This effect is called self-nulling and it can be prevented by using a target-free covariance matrix. More discussion about self-nulling and robust beamforming can be found in [14, 73] and the references therein. Second, using the target-free covariance matrix, the beamformer in (3.10) converges faster than the beamformer using the total covariance matrix. The famous rapid convergence theorem proposed by Reed et al. [86] states that a SINR loss of 3 dB can be obtained by using the number of target-free snapshots equal to twice the size of the covariance matrix. Note that the imprecise physical model which causes steering vector mismatch does not just create the self-nulling problem. It also affects the clutter subspace. Therefore it affects the accuracy of the clutter subspace estimation in Sec. 3.3.2.

3.4.1 The Proposed Method

The target-free covariance matrix can be expressed as $\mathbf{R} = \mathbf{R}_J + \mathbf{R}_c + \sigma^2\mathbf{I}$, where $\mathbf{R}_J$ is the covariance matrix of the jammer signals, $\mathbf{R}_c$ is the covariance matrix of the clutter signals, and σ^2 is the variance of the white noise. By (3.17), there exists a $r_c \times r_c$ matrix $\mathbf{A}_c$ so that $\mathbf{R}_c \approx \mathbf{U}_c \mathbf{A}_c \mathbf{U}_c^\dagger$. Thus

the covariance matrix can be approximated by

$$\mathbf{R} \approx \underbrace{\mathbf{R}_J + \sigma^2\mathbf{I}}_{\text{call this } \mathbf{R}_v} + \mathbf{U}_c\mathbf{A}_c\mathbf{U}_c^\dagger. \tag{3.19}$$

We assume the jammer signals $y^{(J)}_{n,m,l}$ in (3.5) are statistically independent in different pulses and different orthogonal waveform components [44]. Therefore they satisfy

$$E[y^{(J)}_{n,m,l} \cdot y^{(J)\dagger}_{n',m',l'}] = \begin{cases} r_{J,n,n'}, & m = m', l = l' \\ 0, & \text{otherwise,} \end{cases}$$

for $n, n' = 0, 1, \cdots, N$, $m, m' = 0, 1, \cdots, M$, and $l, l' = 0, 1, \cdots, L$. Using this fact, the jammer-plus-noise covariance matrix $\mathbf{R}_v$ defined in (3.19) can be expressed as

$$\mathbf{R}_v = \text{diag}(\mathbf{R}_{vs}, \mathbf{R}_{vs}, \cdots, \mathbf{R}_{vs}), \tag{3.20}$$

where $\mathbf{R}_{vs}$ is an $N \times N$ matrix with elements $[\mathbf{R}_{vs}]_{n,n'} = r_{J,n,n'} + \sigma^2$ for $n, n' = 0, 1, \cdots, N$. Therefore the covariance matrix $\mathbf{R}$ in (3.19) consists of a *low-rank* clutter covariance matrix and a *block-diagonal* jammer-pulse-noise. By using the matrix inversion lemma [48], one can obtain

$$\mathbf{R}^{-1} \approx \mathbf{R}_v^{-1} - \mathbf{R}_v^{-1}\mathbf{U}_c(\mathbf{A}_c^{-1} + \mathbf{U}_c^\dagger\mathbf{R}_v^{-1}\mathbf{U}_c)^{-1}\mathbf{U}_c^\dagger\mathbf{R}_v^{-1}. \tag{3.21}$$

The inverse of the block-diagonal matrix $\mathbf{R}_v^{-1}$ is simply $\mathbf{R}_v^{-1} = \text{diag}(\mathbf{R}_{vs}^{-1}, \mathbf{R}_{vs}^{-1}, \cdots, \mathbf{R}_{vs}^{-1})$ and the multiplication of the block-diagonal matrix with another matrix is simple.

3.4.2 Complexity of the New Method

The complexity of directly inverting the $NML \times NML$ covariance matrix $\mathbf{R}$ is $O(N^3M^3L^3)$. Taking advantage of the block-diagonal matrix and the low rank matrix, in (3.21), the complexity for computing $\mathbf{R}_v^{-1}$ is only $O(N^3)$ and the complexity for computing $\mathbf{A}_c^{-1}$ and $(\mathbf{A}_c + \mathbf{U}_c^\dagger\mathbf{R}_v^{-1}\mathbf{U}_c)^{-1}$ is only $O(r_c^3)$, where r_c is defined in (3.16). The overall complexity for computing (3.21) is thus reduced from $O(N^3M^3L^3)$ to $O(r_cN^2M^2L^2)$. This is the complexity of the multiplication of an $(NML \times r_c)$ matrix by a $(r_c \times NML)$ matrix.

3.4.3 Estimation of the Covariance Matrices

In (3.21), the matrix $\mathbf{U}_c$ can be obtained by the nonuniform sampling of the PSWF as described in the last section. The jammer-pulse-noise covariance matrix $\mathbf{R}_v$ and the matrix $\mathbf{A}_c$ both require further estimation from the received signals. Because of the block-diagonal structure, one can estimate the covariance matrix $\mathbf{R}_v$ by estimating its submatrix $\mathbf{R}_{vs}$ defined in (3.20). The matrix $\mathbf{R}_{vs}$ can be estimated when there are no clutter and target signals. For this, the radar transmitter *operates in passive mode* so that the receiver can collect the signals with only jammer signals and white noise [57]. The submatrix $\mathbf{R}_{vs}$ can be estimated as

$$\hat{\mathbf{R}}_{vs} = \frac{1}{K_v} \sum_{k=0}^{K_v-1} \mathbf{r}_k \mathbf{r}_k^\dagger, \tag{3.22}$$

where $\mathbf{r}_k$ is an $N \times 1$ vector which represents the target-free and clutter-free signals received by N receiving antennas. By (3.19), one can express $\mathbf{A}_c$ as

$$\mathbf{A}_c = (\mathbf{U}_c^\dagger \mathbf{U}_c)^{-1} \mathbf{U}_c^\dagger (\mathbf{R} - \mathbf{R}_v) \mathbf{U}_c (\mathbf{U}_c^\dagger \mathbf{U}_c)^{-1}.$$

Therefore, one can estimate $\mathbf{A}_c$ by using

$$\hat{\mathbf{A}}_c = \frac{1}{K} \sum_{k=0}^{K-1} \mathbf{x}_k \mathbf{x}_k^\dagger - (\mathbf{U}_c^\dagger \mathbf{U}_c)^{-1} \mathbf{U}_c^\dagger \hat{\mathbf{R}}_v \mathbf{U}_c (\mathbf{U}_c^\dagger \mathbf{U}_c)^{-1}, \tag{3.23}$$

where $\mathbf{x}_k = (\mathbf{U}_c^\dagger \mathbf{U}_c)^{-1} \mathbf{U}_c^\dagger \mathbf{y}_k$ and $\mathbf{y}_k$ is the $NML \times 1$ MIMO-STAP signal vector defined in (3.7). Substituting (3.22), (3.23), and (3.21) into the MIMO-STAP beamformer in (3.10), we obtain

$$\begin{aligned} &\mathbf{w} \propto \\ &(\hat{\mathbf{R}}_v^{-1} - \hat{\mathbf{R}}_v^{-1} \mathbf{U}_c (\hat{\mathbf{A}}_c^{-1} + \mathbf{U}_c^\dagger \hat{\mathbf{R}}_v^{-1} \mathbf{U}_c)^{-1} \mathbf{U}_c^\dagger \hat{\mathbf{R}}_v^{-1}) \mathbf{s}(f_s, f_d) \end{aligned} \tag{3.24}$$

3.4.4 Zero-Forcing Method

Instead of estimating $\mathbf{A}_c$ and computing the MVDR by (3.24), one can directly "null out" the entire clutter subspace as described next. Assume that the clutter-to-noise ratio is very large and therefore all of the eigenvalues of $\mathbf{A}_c$ approach infinity. We obtain $\mathbf{A}_c^{-1} \approx \mathbf{0}$. Substituting it into (3.24), one

can obtain the MIMO-STAP beamformer as

$$\mathbf{w} \propto (\hat{\mathbf{R}}_v^{-1} - \hat{\mathbf{R}}_v^{-1}\mathbf{U}_c(\mathbf{U}_c^\dagger\hat{\mathbf{R}}_v^{-1}\mathbf{U}_c)^{-1}\mathbf{U}_c^\dagger\hat{\mathbf{R}}_v^{-1})\mathbf{s}(f_s, f_d). \tag{3.25}$$

Thus we obtain a "zero-forcing" beamformer which nulls out the entire clutter subspace. The advantage of this zero-forcing method is that it is no longer necessary to estimate $\mathbf{A}_c$. In this method, we only need to estimate $\mathbf{R}_{vs}$. The method is independent of the range bin. The matrix $\mathbf{R}^{-1}$ computed by this method can be used for all range bins. Because there are lots of extra dimensions in MIMO radars, dropping the entire clutter subspace will reduce only a small portion of the total dimension. Therefore it will not affect the SINR performance significantly, as we shall demonstrate. Thus this method can be very effective in MIMO radars.

3.4.5 Comparison with Other Methods

In the sample matrix inversion (SMI) method [44], the covariance matrix is estimated to be the quantity $\hat{\mathbf{R}}$ in (3.18) and $\hat{\mathbf{R}}^{-1}$ is directly used in (3.10) to obtain the MVDR beamformer. However, some important information about the covariance matrix is unused in the SMI method. This information includes the parameters γ and β, the structure of the clutter covariance matrix, and the block diagonal structure of the jammer covariance matrix.

Our method in (3.24) utilizes this information. We first estimate the clutter subspace by using parameters γ and β in (3.17). Because the jammer matrix is block diagonal and the clutter matrix has low rank with known subspace, by using the matrix inversion lemma, we could break the inversion of a large matrix $\mathbf{R}$ into the inversions of some smaller matrices. Therefore the computational complexity was significantly reduced. Moreover, by using the structure, fewer parameters need to be estimated. In our method, only the $r_c \times r_c$ matrix $\mathbf{A}$ and the $N \times N$ matrix $\mathbf{R}_{vs}$ need to be estimated rather than the the $NML \times NML$ matrix $\mathbf{R}$ in the SMI method. Therefore our method also converges much faster.

In subspace methods [35, 40, 43–45, 57, 105], the clutter and the jammer subspace are both estimated simultaneously using the STAP signals rather than from problem geometry. Therefore the parameters γ and β and the block diagonal structure of the jammer covariance matrix are not fully utilized. In [56], the target-free and clutter-free covariance matrix are also estimated using (3.22). The jammer and clutter are filtered out in two separate stages. Therefore the block diagonal property of the jammer covariance matrix has been used in [56]. However, the clutter subspace structure

has not been fully utilized in this method.

3.5 Numerical Examples

In this section, we compare the SINR performance of our methods and other existing methods. In the example, the parameters are $M = 5$, $N = 10$, $L = 16$, $\beta = 1.5$, and $\gamma = 10$. The altitude is 9km and the range of interest is 12.728km. For this altitude and range, the clutter is generated by using the model in [42]. The clutter to noise ratio (CNR) is 40 dB. There are two jammers at 20° and -30° degree. The jammer to noise ratio (JNR) for each jammer equals 50 dB. The SINR is normalized so that the maximum SINR equals 0 dB. The jammers are modelled as point sources which emit independent white Gaussian signals. The clutter is modelled using discrete points as described in (3.1). The clutter points are equally spaced on the range bin and the RCS for each clutter is modelled as identical independent Gaussian random variables. In general, the variance of ρ_i will vary along the ground, as we move within one range bin. However, for simplicity we assume this variance is fixed. The number of clutter points N_c is ten thousand. The clutter points for different range bins are also independent. The following methods are compared:

1. *Sample matrix inversion (SMI) method [44].* This method estimates the covariance matrix $\mathbf{R}$ using (3.18) and directly substitutes it into (3.10).

2. *Loaded sample matrix inversion (LSMI) method [1, 13].* Before substituting $\hat{\mathbf{R}}$ into (3.10), a diagonal loading $\hat{\mathbf{R}} \leftarrow \hat{\mathbf{R}} + \delta\mathbf{I}$ is performed. In this example, δ is chosen as ten times the white noise level.

3. *Principal component (PC) method. [44].* This method uses a KLT filterbank to extract the jammer-plus-clutter subspace. Then the space-time beamforming can be performed in this subspace.

4. *Separate jammer and clutter cancellation method [56]* (abbreviated as SJCC below). This method also utilizes the jammer-plus-noise covariance matrix $\mathbf{R}_{vs}$ which can be estimated as in (3.22). The covariance matrix can be used to filter out the jammer and form a spatial beam. Then the clutter can be further filtered out by space-time filtering [56]. In this example, a diagonal loading is used for the space-time filtering with a loading factor which equals ten times the white noise level.

5. *The new zero-forcing (ZF) method.* This method directly nulls out the clutter subspace as described in (3.25).

6. *The new minimum variance method.* This method estimates $\hat{\mathbf{R}}_{vs}$ and $\hat{\mathbf{A}}_c$ and uses (3.24). In this example, a diagonal loading is used for $\hat{\mathbf{A}}_c$ with a loading factor which equals ten times the white noise level.

7. *MVDR with perfectly known* $\mathbf{R}$. This method is unrealizable because the perfect $\mathbf{R}$ is always unavailable. It is shown in the figure because it serves as an upper bound on the SINR performance.

Fig. 3.5 shows the comparison of the SINR for $f_s = 0$ as a function of the Doppler frequencies. The SINR is defined as

$$\text{SINR} \triangleq \frac{|\mathbf{w}^\dagger \mathbf{s}(f_s, f_D)|^2}{\mathbf{w}^\dagger \mathbf{R} \mathbf{w}},$$

where $\mathbf{R}$ is the target-free covariance matrix. To compare these methods, we fix the number of

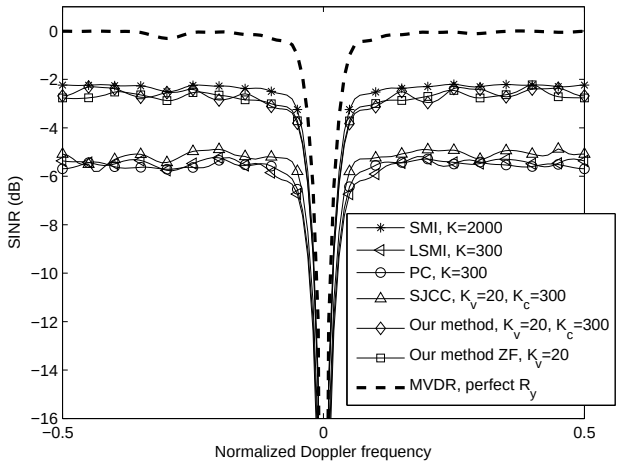

Figure 3.5: The SINR performance of different STAP methods at looking direction zero as a function of the Doppler frequency

samples K and the number of jammer-plus-noise samples K_v. In all of the methods except the SMI method, 300 samples and 20 jammer-plus-noise samples are used. We use 2000 samples instead of 300 samples in the SMI method because the estimated covariance matrix in (3.18) with 300 samples is not full-rank and therefore can not be inverted. The spatial beampatterns and space-time beampatterns for the target at $f_s = 0$ and $f_D = 0.25$ for four of these methods are shown in Fig. 3.6 and

Fig. 3.7, respectively. The spatial beampattern is defined as

$$\sum_{k=0}^{ML-1} |\mathbf{w}^{\dagger}_{(1:N)+kML}\mathbf{s}(f_s)|^2,$$

where $\mathbf{s}(f_s)$ is the spatial steering vector

$$\begin{pmatrix} 1 & e^{j2\pi f_s} & \dots & e^{j2\pi f_s(N-1)} \end{pmatrix}^T,$$

and $\mathbf{w}_{(1:N)+kML}$ represents N successive elements of $\mathbf{w}$ starting from $kML+1$. The space-time beampattern is defined as

$$|\mathbf{w}^{\dagger}\mathbf{s}(f_s, f_D)|,$$

where $\mathbf{s}(f_s, f_D)$ is the space-time steering vector defined in (3.9). The spatial beampattern rep-

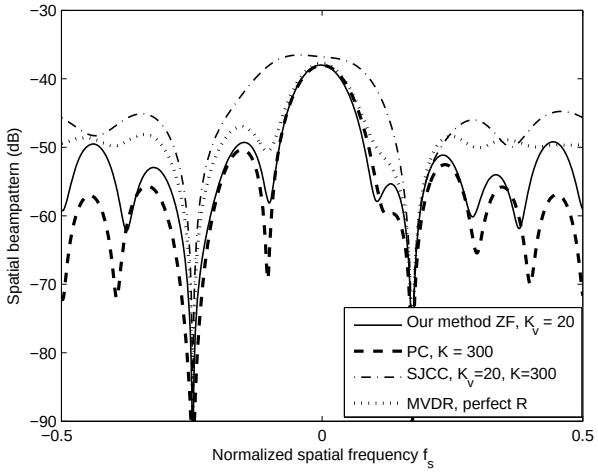

Figure 3.6: Spatial beampatterns for four STAP methods

resents the jammer and noise rejection and the space-time beampattern represents the clutter rejection. In Fig. 3.6, one can see the jammer notches at the corresponding jammer arrival angles -30° and 20°. In Fig. 3.7, one can also observe the clutter notch in the beampatterns. In Fig. 3.5, lacking use of the covariance matrix structure, the SMI method requires a lot of samples to obtain good performance. It uses 2000 samples but the proposed minimum variance method which has a comparable performance uses only 300 samples. The PC method and LSMI method utilize the fact that the jammer-plus-clutter covariance matrix has low rank. Therefore they require fewer samples

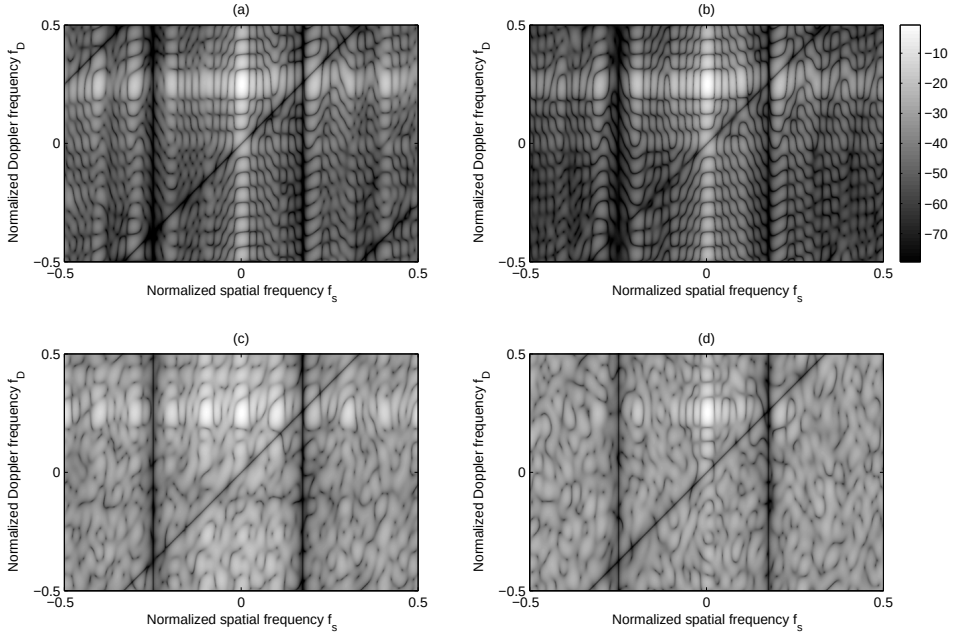

Figure 3.7: Space-time beampatterns for four methods: (a) The proposed zero-forcing method, (b) Principal component (PC) method [44], (c) Separate jammer and clutter cancellation method (SJCC) [56] and (d) Sample matrix inversion (SMI) method [44]

than the SMI method. The performance of these two are about the same. The SJCC method further utilizes the fact that the jammer covariance matrix is block diagonal and estimates the jammer-plus-noise covariance matrix. Therefore the SINR performance is slightly better than the LSMI and PC methods. Our methods not only utilize the low rank property and the block diagonal property but also the geometry of the problem. Therefore our methods have better SINR performance than the SJCC method. The proposed zero-forcing (ZF) method has about the same performance as the minimum variance method. It converges to a satisfactory SINR with very few clutter-free samples. According to (3.15), the clutter rank in this example is approximately

$$\lceil N + \gamma(M-1) + \beta(L-1) \rceil = 73.$$

Thanks to the MIMO radar, the dimension of the space-time steering vector is $MNL = 800$. The clutter rank is just a small portion of the total dimension. This is the reason why the ZF method, which directly nulls out the entire clutter space, works so well.

3.6 Conclusions

In this chapter, we first studied the clutter subspace and its rank in MIMO radars using the geometry of the system. We derived an extension of Brennan's rule for estimating the dimension of the clutter subspace in MIMO Radar systems. This rule is given in (3.15). An algorithm for computing the clutter subspace using nonuniform sampled PSWF was described. Then we proposed a space-time adaptive processing method in MIMO radars. This method utilizes the knowledge of the geometry of the problem, the structure of the clutter space, and the block diagonal structure of the jammer covariance matrix. Using the fact that the jammer matrix is block diagonal and the clutter matrix has low rank with known subspace, we showed how to break the inversion of a large matrix $\mathbf{R}$ into the inversions of smaller matrices using the matrix inversion lemma. Therefore the new method has much lower computational complexity. Moreover, we can directly null out the entire clutter space for large clutter. In our ZF method, only the $N \times N$ jammer-plus-noise matrix $\mathbf{R}_{vs}$ needs to be estimated instead of the the $NML \times NML$ matrix $\mathbf{R}$ in the SMI method, where N is the number of receiving antennas, M is the number of transmitting antennas, and L is the number of pulses in a coherent processing interval. Therefore, for a given number of data samples, the new method has better performance. In Sec. 3.5, we provided an example where the number of training samples was reduced by a factor of 100 with no appreciable loss in performance compared to the SMI method.

In practice, the clutter subspace might change because of effects such as the internal clutter motion (ICM), velocity misalignment, array manifold mismatch, and channel mismatch [44]. In this chapter, we considered an "ideal model", which does not take these effects into account. When this model is not valid, the performance of the algorithm will degrade. One way to overcome this might be to estimate the clutter subspace by using a combination of both the assumed geometry and the received data. Another way might be to develop a more robust algorithm against the clutter subspace mismatch. These ideas will be explored in the future.

Chapter 4

Ambiguity Function of the MIMO Radar and the Waveform Optimization

This chapter focuses on the ambiguity function of the MIMO radar and the corresponding waveform design methods. In traditional (SIMO) radars, the ambiguity function of the transmitted pulse characterizes the compromise between range and Doppler resolutions. It is a major tool for studying and analyzing radar signals. Recently, the idea of ambiguity function has been extended to the case of MIMO radar. In this chapter, some mathematical properties of the MIMO radar ambiguity function are first derived. These properties provide some insights into the MIMO radar waveform design. Then a new algorithm for designing the orthogonal frequency-hopping waveforms is proposed. This algorithm reduces the sidelobes in the corresponding MIMO radar ambiguity function and makes the energy of the ambiguity function spread evenly in the range and angular dimensions. Most of the results of this chapter have been reported in our recent journal paper [16] and book chapter in [70].

4.1 Introduction

Recently, several papers have been published on the topic of MIMO radar waveform design [36, 37, 94, 108, 109]. In [37], the covariance matrix of the transmitted waveforms has been designed to form a focused beam such that the power can be transmitted to a desired range of angles. In [94], the authors have also focused on the design of the covariance matrix to control the spatial power. However in [94], the cross-correlation between the transmitted signals at a number of given target

locations is minimized. In [36, 61, 108, 109], unlike [37, 94], the entire waveforms have been considered instead of just the covariance matrix. Consequently these design methods involve not only the spatial domain but also the range domain. These methods assume some prior knowledge of the impulse response of the target and use this knowledge to choose the waveforms which optimize the mutual information between the received signals and the impulse response of the target. The waveform design which uses prior knowledge about the target has been done in the traditional SIMO radar system as well [5]. In this chapter, we consider a different aspect of the waveform design problem. We design the waveforms to optimize the MIMO radar ambiguity function [89]. Unlike the above methods, we do not assume the prior knowledge about the target.

The waveform design problem based on optimization of the ambiguity function in the traditional SIMO radar has been well studied. Several waveform design methods have been proposed to meet different resolution requirements. These methods can be found in [62] and the references therein. In the traditional SIMO radar system, the radar receiver uses a matched filter to extract the target signal from thermal noise. Consequently, the resolution of the radar system is determined by the response to a point target in the matched filter output. Such a response can be characterized by a function called the ambiguity function [62]. Recently, San Antonio, et al. [89] have extended the radar ambiguity function to the MIMO radar case. It turns out that the radar waveforms affect not only the range and Doppler resolution but also the angular resolution. It is well-known that the radar ambiguity function satisfies some properties such as constant energy and symmetry with respect to the origin [62]. These properties are very handy tools for designing and analyzing the radar waveforms. In this chapter, we derive the corresponding properties for the MIMO radar case.

The major contributions in this chapter are two-fold: (1) to derive new mathematical properties of the MIMO ambiguity function, and (2) to design a set of frequency-hopping pulses to optimize the MIMO ambiguity function. The MIMO radar ambiguity function characterizes the resolutions of the radar system. By choosing different waveforms, we obtain a different MIMO ambiguity function. Therefore the MIMO radar waveform design problem is to choose a set of waveforms which provides a desirable MIMO ambiguity function. Directly optimizing the waveforms requires techniques such as calculus of variation. In general this can be very hard to solve. Instead of directly designing the waveforms, we can impose some structures on the waveforms and design the parameters of the waveforms.

As an example of this idea, the pulse waveforms generated by frequency-hopping codes are

considered in this chapter. Frequency-hopping signals are good candidates for the radar waveforms because they are easily generated and have constant modulus. In the traditional SIMO radar, Costas codes [19, 41] have been introduced to reduce the sidelobe in the radar ambiguity function. The frequency-hopping waveforms proposed in [74] have been applied in a MIMO HF OTH radar system [34]. The frequency-hopping waveforms proposed in [74] were originally designed for multi-user radar system. The peaks in the cross correlation functions of the waveforms are approximately minimized by the codes designed in [74]. However, in the multi-user scenario, each user operates its own radar system. This is different from the MIMO radar system where the receiving antennas can cooperate to resolve the target parameters. In this chapter, we design the frequency-hopping waveforms to optimize the MIMO ambiguity function which directly relates to the MIMO radar system resolution.

The rest of the chapter is organized as follows. In Sec. 2, the MIMO radar ambiguity function will be briefly reviewed. Sec. 3 derives the properties of the MIMO radar ambiguity function. In Sec. 4, we derive the MIMO radar ambiguity function when the pulse trains are transmitted. In Sec. 5, we define the frequency-hopping pulse waveforms in MIMO radar and derive the corresponding MIMO ambiguity function. In Sec. 6, we formulate the frequency-hopping code optimization problem and show how to solve it. In Sec. 7, we test the proposed method and compare its ambiguity function with the LFM (linear frequency modulation) waveforms. Finally, Sec. 8 concludes the chapter. The results in this chapter are for uniform linear arrays but they can easily be generalized.

4.2 Review of MIMO Radar Ambiguity Function

In a SIMO radar system, the radar ambiguity function is defined as [62]

$$|\chi(\tau,\nu)| \triangleq \left| \int_{-\infty}^{\infty} u(t)u^*(t+\tau)e^{j2\pi\nu t}dt \right|, \tag{4.1}$$

where $u(t)$ is the radar waveform. This two-dimensional function indicates the matched filter output in the receiver when a delay mismatch τ and a Doppler mismatch ν occur. The value $|\chi(0,0)|$ represents the matched filter output without any mismatch. Therefore, the sharper the function $|\chi(\tau,\nu)|$ around $(0,0)$, the better the Doppler and range resolution. Fig. 4.1 shows two examples of the ambiguity function. These two ambiguity functions show different Doppler and range tradeoffs. One can see that the LFM pulse has a better range resolution along the cut where Doppler

frequency is zero.

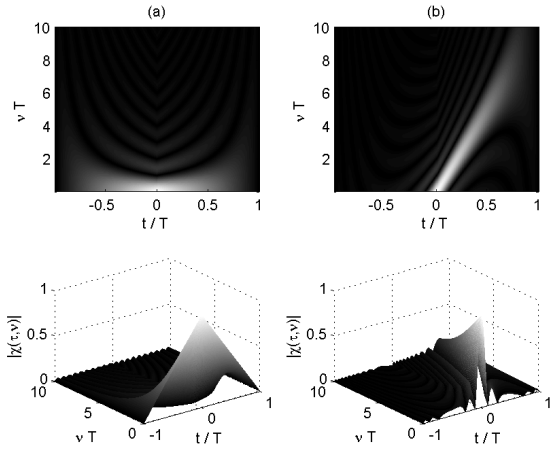

Figure 4.1: Examples of ambiguity functions: (a) Rectangular pulse, and (b) Linear frequency modulation (LFM) pulse with time-bandwidth product 10, where T is the pulse duration

The idea of radar ambiguity functions has been extended to the MIMO radar by San Antonio et al. [89]. In this section, we will briefly review the definition of MIMO radar ambiguity functions. We will focus only on the ULA (uniform linear array) case as shown in Fig. 4.2. The derivation of the MIMO ambiguity function for arbitrary array can be found in [89]. We assume the transmitter and the receiver are parallel and colocated ULAs. The spacing between the transmitting elements

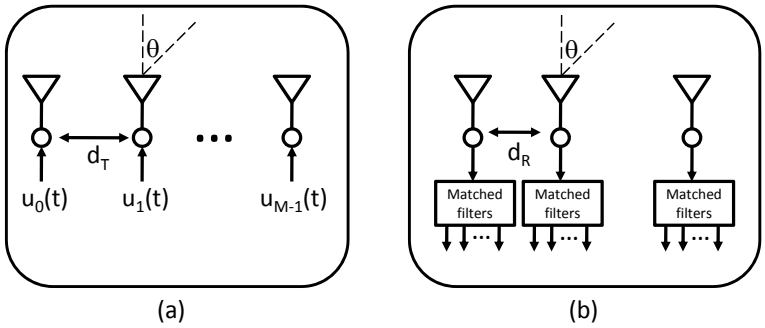

Figure 4.2: MIMO radar scheme: (a) Transmitter, and (b) Receiver

is d_T and the spacing between the receiving elements is d_R. The function $u_i(t)$ indicates the radar waveform emitted by the ith transmitter.

Consider a target at (τ, ν, f) where τ is the delay corresponding to the target range, ν is the

Doppler frequency of the target, and f is the normalized spatial frequency of the target defined as

$$f \triangleq 2\pi \frac{d_R}{\lambda} \sin\theta,$$

where θ is the angle of the target and λ is the wavelength. The demodulated target response in the nth antenna is proportional to

$$y_n^{\tau,\nu,f}(t) \approx \sum_{m=0}^{M-1} u_m(t-\tau) e^{j2\pi\nu t} e^{j2\pi f(\gamma m+n)},$$

for $n = 0, 1, \cdots, N-1$, where N is the number of receiving antennas, $u_m(t)$ is the radar waveform emitted by the mth antenna, $\gamma \triangleq d_T/d_R$ and M is the number of transmitting antennas. If the receiver tries to capture this target signal with a matched filter with the assumed parameters (τ', ν', f') then the matched filter output becomes

$$\begin{aligned} & \sum_{n=0}^{N-1} \int_{-\infty}^{\infty} y_n^{\tau,\nu,f}(t) \cdot (y_n^{\tau',\nu',f'})^*(t) dt \\ = & \left(\sum_{n=0}^{N-1} e^{j2\pi(f-f')n} \right) \cdot \\ & \left(\sum_{m=0}^{M-1} \sum_{m'=0}^{M-1} \int_{-\infty}^{\infty} u_m(t-\tau) u_{m'}^*(t-\tau') \right. \\ & \left. e^{j2\pi(\nu-\nu')t} dt \cdot e^{j2\pi(fm-f'm')\gamma} \right) \end{aligned}$$

The first part in the right hand side of the equation represents the spatial processing in the receiver, and it is not affected by the waveforms $\{u_m(t)\}$. The second part in the right hand side of the equation indicates how the waveforms $\{u_m(t)\}$ affect the spatial, Doppler, and range resolutions of the radar system. Therefore, we define the **MIMO radar ambiguity function** as

$$\chi(\tau, \nu, f, f') \triangleq \sum_{m=0}^{M-1} \sum_{m'=0}^{M-1} \chi_{m,m'}(\tau, \nu) e^{j2\pi(fm-f'm')\gamma}, \tag{4.2}$$

where

$$\chi_{m,m'}(\tau, \nu) \triangleq \int_{-\infty}^{\infty} u_m(t) u_{m'}^*(t+\tau) e^{j2\pi\nu t} dt. \tag{4.3}$$

Note that the MIMO radar ambiguity function can not be expressed as a function of the difference

of the spatial frequencies, namely $f - f'$. Therefore, we need both the target spatial frequency f and the assumed spatial frequency f' to represent the spatial mismatch. We call the function $\chi_{m,m'}(\tau, \nu)$ the **cross ambiguity function** because it is similar to the SIMO ambiguity function defined in (4.1) except it involves two waveforms $u_m(t)$ and $u_{m'}(t)$. Fixing τ and ν in (4.2), one can view the ambiguity function as a scaled two-dimensional Fourier transform of the cross ambiguity function $\chi_{m,m'}(\tau, \nu)$ on the parameters m and m'. The value $|\chi(0, 0, f, f)|$ represents the matched filter output without mismatch. Therefore, the sharper the function $|\chi(\tau, \nu, f, f')|$ around the line $\{(0, 0, f, f)\}$, the better the radar system resolution.

4.3 Properties of The MIMO Radar Ambiguity Function for ULA

We now derive some new properties of the MIMO radar ambiguity function defined in (4.2). The properties are similar to some of the properties of the SIMO ambiguity functions (e.g., see [62]). We normalize the energy of the transmitted waveform to unity. That is,

$$\int_{-\infty}^{\infty} |u_m(t)|^2 dt = 1, \forall m. \tag{4.4}$$

The following property characterizes the ambiguity function when there exists no mismatch.

Property 1. If $\int_{-\infty}^{\infty} u_m(t) u_{m'}^*(t) dt = \delta_{m,m'}$, then

$$\chi(0, 0, f, f) = M, \forall f. \tag{4.5}$$

Proof: We have

$$\chi_{m,m'}(0, 0) = \int_{-\infty}^{\infty} u_m(t) u_{m'}^*(t) dt = \delta_{m,m'}.$$

Substituting the above equation into (4.2), we obtain

$$\begin{aligned} \chi(0, 0, f, f) &= \sum_{m=0}^{M-1} \sum_{m'=0}^{M-1} \delta_{m,m'} e^{j2\pi\gamma(fm - fm')} \\ &= \sum_{m=0}^{M-1} e^{j0} = M. \end{aligned}$$ ■

This property says that if the waveforms are orthogonal, the ambiguity function is a constant

along the line $\{(0,0,f,f)\}$ which is independent of the waveforms $\{u_m(t)\}$. This means the matched filter output is always a constant independent of the waveforms, when there exists no mismatch.

The following property characterizes the integration of the MIMO radar ambiguity function along the line $\{0,0,f,f\}$ even when the waveforms are not orthogonal.

Property 2.

$$\chi(0,0,f,f) \geq 0, \tag{4.6}$$

and if γ is an integer, then

$$\int_0^1 \chi(0,0,f,f)df = M. \tag{4.7}$$

Proof: By using the definitions in (4.2) and (4.3), we have

$$\chi(0,0,f,f) \quad = \quad \int_{-\infty}^{\infty} \left| \sum_{m=0}^{M-1} u_m(t) e^{j2\pi f m\gamma} \right|^2 dt \geq 0.$$

By using the definitions in (4.2) and (4.3) and changing variables, we obtain

$$\begin{aligned} & \int_0^1 \chi(0,0,f,f)df \\ = & \int_0^1 \sum_{m=0}^{M-1} \sum_{m'=0}^{M-1} \chi_{m,m'}(0,0) e^{j2\pi f\gamma(m-m')} df \\ = & \sum_{m=0}^{M-1} \sum_{m'=0}^{M-1} \chi_{m,m'}(0,0)\delta_{m,m'} = M. \end{aligned}$$ ■

This property says that when γ is an integer, the integration of the MIMO radar ambiguity function along the line $\{0,0,f,f\}$ is a constant, no matter how waveforms are chosen. The following property characterizes the energy of the cross ambiguity function.

Property 3.

$$\int_{-\infty}^{\infty} \int_{-\infty}^{\infty} |\chi_{m,m'}(\tau,\nu)|^2 d\tau d\nu = 1. \tag{4.8}$$

Proof: We have

$$\begin{aligned}
&\int_{-\infty}^{\infty}\int_{-\infty}^{\infty}|\chi_{m,m'}(\tau,\nu)|^2 d\tau d\nu \\
= &\int_{-\infty}^{\infty}\int_{-\infty}^{\infty}\left|\int_{-\infty}^{\infty}u_m(t)u_{m'}^*(t+\tau)e^{j2\pi\nu t}dt\right|^2 d\nu d\tau \\
= &\int_{-\infty}^{\infty}\int_{-\infty}^{\infty}\left|u_m(t)u_{m'}^*(t+\tau)\right|^2 dt d\tau,
\end{aligned}$$

where we have used Parseval's theorem [79] to obtain the last equality. By changing variables, we obtain

$$\begin{aligned}
\int_{-\infty}^{\infty}\int_{-\infty}^{\infty}\left|u_m(t)u_{m'}^*(t+\tau)\right|^2 dt d\tau &= \\
\int_{-\infty}^{\infty}|u_m(t)|^2 dt \int_{-\infty}^{\infty}|u_{m'}(t)|^2 dt &= 1. \qquad \blacksquare
\end{aligned}$$

This property states that the energy of the cross ambiguity function is a constant, independent of the waveforms $u_m(t)$ and $u_{m'}(t)$. In the special case of $m = m'$, this property reduces to the well-known result that the SIMO radar ambiguity function defined in (4.1) has constant energy [62]. The following property characterizes the energy of the MIMO radar ambiguity function.

Property 4. If γ is an integer, then

$$\int_0^1\int_0^1\int_{-\infty}^{\infty}\int_{-\infty}^{\infty}|\chi(\tau,\nu,f,f')|^2 d\tau d\nu df df' = M^2. \tag{4.9}$$

Proof: By using the definition of MIMO radar ambiguity function in (4.2) and performing appropriate change of variables, we have

$$\begin{aligned}
&\int_0^1\int_0^1\int_{-\infty}^{\infty}\int_{-\infty}^{\infty}|\chi(\tau,\nu,f,f')|^2 d\tau d\nu df df' \\
= &\frac{1}{\gamma^2}\int_{-\infty}^{\infty}\int_{-\infty}^{\infty}\int_0^{\gamma}\int_0^{\gamma} \\
&\left|\sum_{m=0}^{M-1}\sum_{m'=0}^{M-1}\chi_{m,m'}(\tau,\nu)e^{j2\pi(fm-f'm')}\right|^2 df df' d\tau d\nu.
\end{aligned} \tag{4.10}$$

Using Parserval's theorem and applying Property 3, the above integral reduces to

$$\int_{-\infty}^{\infty}\int_{-\infty}^{\infty}\sum_{m=0}^{M-1}\sum_{m'=0}^{M-1}|\chi_{m,m'}(\tau,\nu)|^2 d\tau d\nu = \sum_{m'=0}^{M-1}\sum_{m'=0}^{M-1} 1 = M^2.$$

■

This property states that when γ is an integer, the energy of the MIMO radar ambiguity function is a constant which is independent of the waveforms $\{u_m(t)\}$. For example, whether we choose $\gamma = 1$ or $\gamma = N$, the energy of the MIMO radar ambiguity function is the same. Recall that Property 2 states that the integration of MIMO radar ambiguity function along the line $\{(0, 0, f, f\}$ is also a constant. This implies that in order to make the ambiguity function sharp around $\{0, 0, f, f\}$, we have to spread the energy of the ambiguity function evenly on the available time and bandwidth.

For the case that γ is not an integer, we can not directly apply Parserval's theorem. In this case, the energy of the ambiguity function actually depends on the waveforms $\{u_m(t)\}$. However, the following property characterizes the range of the energy of the MIMO radar ambiguity function.

Property 5.

$$\begin{aligned}\frac{\lfloor\gamma\rfloor^2}{\gamma^2}M^2 \le \int_0^1\int_0^1\int_{-\infty}^{\infty}\int_{-\infty}^{\infty}|\chi(\tau,\nu,f,f')|^2 d\tau d\nu df df' \\ \le \frac{\lceil\gamma\rceil^2}{\gamma^2}M^2\end{aligned} \tag{4.11}$$

where $\lfloor\gamma\rfloor$ is the largest integer $\le \gamma$, and $\lceil\gamma\rceil$ is the smallest integer $\ge \gamma$.

Proof: Using (4.10), we have

$$\begin{aligned}&\int_0^1\int_0^1\int_{-\infty}^{\infty}\int_{-\infty}^{\infty}|\chi(\tau,\nu,f,f')|^2 d\tau d\nu df df' \\ \le\ & \frac{1}{\gamma^2}\int_{-\infty}^{\infty}\int_{-\infty}^{\infty}\int_0^{\lceil\gamma\rceil}\int_0^{\lceil\gamma\rceil} \\ & \left|\sum_{m=0}^{M-1}\sum_{m'=0}^{M-1}\chi_{m,m'}(\tau,\nu)e^{j2\pi(fm-f'm')}\right|^2 df df' d\tau d\nu.\end{aligned} \tag{4.12}$$

Using Parserval's theorem and applying Property 3, the above value equals

$$\frac{\lceil\gamma\rceil^2}{\gamma^2}\int_{-\infty}^{\infty}\int_{-\infty}^{\infty}\sum_{m=0}^{M-1}\sum_{m'=0}^{M-1}|\chi_{m,m'}(\tau,\nu)|^2 d\tau d\nu = \frac{\lceil\gamma\rceil^2}{\gamma^2}M^2.$$

The lower bound can be obtained similarly. ■

For the case that γ is not integer, the energy of the MIMO radar ambiguity function can actually be affected by the waveforms $\{u_m(t)\}$. However, the above property implies that when γ is large, the amount by which the energy can be affected by the waveforms is small. Note that the bound provided by this property is loose when γ is small. This is because in (4.12), we have quantized γ in the integration interval in order to apply the Parserval's theorem. However, in order to form a large virtual array and keep the interference rejection ability on the receiver side, the spacings between the transmitting antennas are usually larger than those of the receiving antennas. So γ is usually large. Using similar lines of argument as in 4.12, we can show that when γ is not an integer, Property 2 can be replaced with the following property.

Property 6.

$$M\frac{\lfloor\gamma\rfloor}{\gamma} \leq \int_0^1 \chi(0,0,f,f)df \leq M\frac{\lceil\gamma\rceil}{\gamma}. \tag{4.13}$$

The following property characterizes the symmetry of the cross ambiguity function.

Property 7.

$$\chi_{m,m'}(-\tau,-\nu) = \chi^*_{m',m}(\tau,\nu)e^{-j2\pi\nu\tau}. \tag{4.14}$$

Proof: By the definition of the cross ambiguity function (4.3) and changing variables, we have

$$\begin{aligned}
\chi_{m,m'}(-\tau,-\nu) &= \int_{-\infty}^{\infty} u_m(t)u^*_{m'}(t-\tau)e^{-j2\pi\nu t}dt \\
&= \int_{-\infty}^{\infty} u_m(t+\tau)u^*_{m'}(t)e^{-j2\pi\nu(t+\tau)}dt \\
&= \chi^*_{m',m}(\tau,\nu)e^{-j2\pi\nu\tau}. \qquad \blacksquare
\end{aligned}$$

Using the above property, we can obtain the following property of the MIMO radar ambiguity function.

Property 8.

$$\chi(-\tau,-\nu,f,f') = \chi^*(\tau,\nu,f',f)e^{-j2\pi\nu\tau} \tag{4.15}$$

Proof: Using the definition of the MIMO radar ambiguity function (4.2) and Property 7, we have

$$\begin{aligned}
& \chi(-\tau,-\nu,f,f') \\
= & \sum_{m=0}^{M-1}\sum_{m'=0}^{M-1}\chi_{m,m'}(-\tau,-\nu)e^{j2\pi\gamma(fm-f'm')} \\
= & \sum_{m=0}^{M-1}\sum_{m'=0}^{M-1}\chi^*_{m',m}(\tau,\nu)e^{-j2\pi\nu\tau}e^{j2\pi\gamma(fm-f'm')} \\
= & \left(\sum_{m=0}^{M-1}\sum_{m'=0}^{M-1}\chi_{m',m}(\tau,\nu)e^{j2\pi\gamma(f'm'-fm)}\right)^* e^{-j2\pi\nu\tau} \\
= & \chi^*(\tau,\nu,f',f)e^{-j2\pi\nu\tau}. \qquad \blacksquare
\end{aligned}$$

This property implies that when we design the waveform, we only need to focus on the region $\{(\tau,\nu,f,f')|\tau \geq 0\}$ or the region $\{(\tau,\nu,f,f')|f \geq f'\}$ of the MIMO radar ambiguity function. For example, given two spatial frequencies f and f' it is sufficient to study only $\chi(\tau,\nu,f,f')$ because the function $\chi(\tau,\nu,f',f)$ can be deduced from the symmetry property. The following property characterizes the cross ambiguity function of the linear frequency modulation (LFM) signal.

Property 9. Define

$$u_m^{LFM}(t) \triangleq u_m(t)e^{j\pi kt^2}.$$

If $\chi_{m,m'}(\tau,\nu) = \int_{-\infty}^{\infty} u_m(t)u^*_{m'}(t+\tau)e^{j2\pi\nu t}dt$ then

$$\begin{aligned}
\chi^{LFM}_{m,m'}(\tau,\nu) & \triangleq \int_{-\infty}^{\infty} u_m^{LFM}(t)(u_{m'}^{LFM}(t+\tau))^* e^{j2\pi\nu t}dt \\
& = \chi_{m,m'}(\tau,\nu-k\tau)e^{-j\pi k\tau^2}.
\end{aligned} \tag{4.16}$$

Proof: From direct calculation, we have

$$\begin{aligned}
\chi^{LFM}_{m,m'}(\tau,\nu) & = \int_{-\infty}^{\infty} u_m(t)u^*_{m'}(t+\tau)\cdot \\
& \quad e^{j\pi k(-2t\tau-\tau^2)}e^{j2\pi\nu t}dt \\
& = \chi_{m,m'}(\tau,\nu-k\tau)e^{-j\pi k\tau^2}. \qquad \blacksquare
\end{aligned}$$

This property says that linear frequency modulation shears off the cross ambiguity function. We use this property to obtain the following result for the MIMO radar ambiguity function.

Property 10.

If $\chi(\tau,\nu,f,f') = \sum_{m=0}^{M-1}\sum_{m'=0}^{M-1}\chi_{m,m'}(\tau,\nu)e^{j2\pi\gamma(fm-f'm')}$ then

$$\begin{aligned}\chi^{LFM}(\tau,\nu,f,f') &\triangleq \sum_{m=0}^{M-1}\sum_{m'=0}^{M-1}\chi^{LFM}_{m,m'}(\tau,\nu)e^{j2\pi\gamma(fm-f'm')} \\ &= \chi(\tau,\nu-k\tau,f,f')e^{-j\pi k\tau^2}. \end{aligned} \tag{4.17}$$

We omit the proof because this property can be easily obtained by just applying Property 9. This property states that adding LFM modulations shears off the MIMO radar ambiguity function. This shearing can improve the range resolution because it compresses the ambiguity function along the direction $(\tau,0,f,f)$ [62]. Fig. 4.3 illustrates contours of constants $\chi(\tau,\nu,f,f')$ and $\chi(\tau,\nu-k\tau,f,f')$ with some fixed f and f'. One can observe that the delay resolution has been improved after the

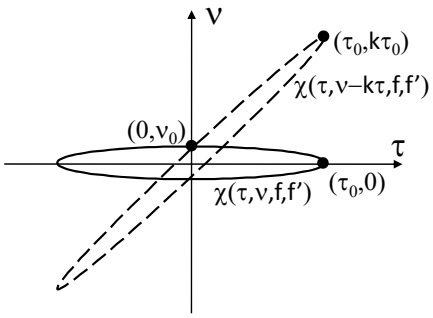

Figure 4.3: Illustration of the LFM shearing

LFM shearing.

To summarize, Properties 1 to 6 characterize the signal component and the energy of the ambiguity function. They imply that if we attempt to squeeze the ambiguity function to the line $\{0,0,f,f\}$, the signal component cannot go arbitrarily high. Also if we attempt to eliminate some unwanted peaks in the ambiguity function, the energy will reappear somewhere else. Property 8 suggests that it is sufficient to study only half of the ambiguity function ($\tau \geq 0$). Properties 9 and 10 imply that the LFM modulation shears the ambiguity function. Therefore it improves the resolution along the range dimension.

4.4 Pulse MIMO Radar Ambiguity Function

In this chapter, we consider the waveform design problem for the pulse waveforms generated by frequency-hopping codes. In this section, we derive the MIMO radar ambiguity function for the case when the waveform $u_m(t)$ consists of the shifted versions of a shorter waveform $\phi_m(t)$. In this case, the pulse design problem becomes choosing the waveform $\phi_m(t)$ to obtain a good MIMO ambiguity function $\chi(\tau, \nu, f, f')$. Therefore, it is important to study the relation between the MIMO ambiguity function and the pulse $\phi_m(t)$. Since modulation and scalar multiplication will not change the shape of the ambiguity function, for convenience, we write the transmitted signals as

$$u_m(t) = \sum_{l=0}^{L-1} \phi_m(t - T_l). \tag{4.18}$$

Fig. 4.4 illustrates the transmitted pulse waveform. Note that the duration of $\phi_m(t)$, namely T_ϕ,

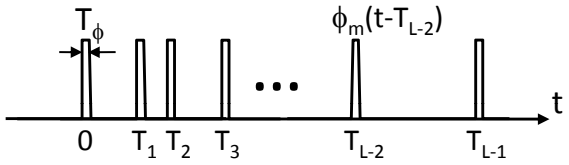

Figure 4.4: Illustration of the pulse waveform

is small enough such that $T_\phi \ll \min_{l,l'}(|T_l - T_{l'}|)$. To obtain the relation between $\phi_m(t)$ and the MIMO ambiguity function $\chi(\tau, \nu, f, f')$, we first derive the cross ambiguity function. Using (4.3) and (4.18) and changing variables, the cross ambiguity function can be expressed as

$$\begin{aligned}
&\chi_{m,m'}(\tau, \nu) = \\
&\sum_{l'=0}^{L-1} \sum_{l=0}^{L-1} \int_{-\infty}^{\infty} \phi_m(t) \phi_{m'}^*(t + T_l - T_{l'} + \tau) e^{j2\pi\nu(t+T_l)} dt \\
&= \sum_{l'=0}^{L-1} \sum_{l=0}^{L-1} \chi_{m,m'}^{\phi}(\tau + T_l - T_{l'}, \nu) e^{j2\pi\nu T_l},
\end{aligned} \tag{4.19}$$

where $\chi^{\phi}_{m,m'}(\tau,\nu)$ is defined as the cross ambiguity function of the pulses $\phi_m(t)$ and $\phi_{m'}(t)$, that is,

$$\chi^{\phi}_{m,m'}(\tau,\nu) = \int_0^{T_\phi} \phi_m(t)\phi^*_{m'}(t+\tau)e^{j2\pi\nu t}dt.$$

We assume that the Doppler frequency ν and the support of pulse T_ϕ are both small enough such that $T_\phi\nu \approx 0$. This means the Doppler frequency envelope remains approximately constant within the pulse. Such an assumption is usually made in pulse Doppler processing [87]. So the above the equation becomes

$$\chi^{\phi}_{m,m'}(\tau,\nu) \approx \int_0^{T_\phi} \phi_m(t)\phi^*_{m'}(t+\tau)dt \triangleq r^{\phi}_{m,m'}(\tau), \tag{4.20}$$

where $r^{\phi}_{m,m'}(\tau)$ is the cross correlation between $\phi_m(t)$ and $\phi_{m'}(t)$. Thus, the cross ambiguity function reduces to the cross correlation function and it is no longer a function of Doppler frequency ν. Substituting the above result into (4.19), we obtain

$$\chi_{m,m'}(\tau,\nu) \approx \sum_{l'=0}^{L-1}\sum_{l=0}^{L-1} r^{\phi}_{m,m'}(\tau + T_l - T_{l'})e^{j2\pi\nu T_l}. \tag{4.21}$$

For values of the delay τ satisfying $|\tau| < \min_{l,l'}(|T_l - T_{l'}|) - T_\phi$, the shifted correlation function satisfies

$$r^{\phi}_{m,m'}(\tau + T_l - T_{l'}) = \int_0^{T_\phi} \phi_m(\tau)\phi^*_{m'}(t+\tau+T_l-T_{l'})dt = 0,$$

when $l \neq l'$. For $|\tau| \geq \min_{l,l'}(|T_l - T_{l'}|) - T_\phi$, the response in the ambiguity function is created by the second trip echoes. This ambiguity is called range folding. In this chapter, we assume the pulse repetition frequency (PRF) is low enough so that no reflections occur at these second trip ranges. We will focus on the ambiguity function only when $|\tau| < \min_{l,l'}(|T_l - T_{l'}|) - T_\phi$. In this case, we have

$$\chi_{m,m'}(\tau,\nu) \approx r^{\phi}_{m,m'}(\tau)\sum_{l=0}^{L-1} e^{j2\pi\nu T_l}.$$

Notice that the Doppler processing is separable from the correlation function. This is because of the assumption that the duration of the pulses T_ϕ and the Doppler frequency ν are small enough

so that $\nu T_\phi \approx 0$. This implies that the choice of the waveforms $\{\phi_m(t)\}$ does not affect the Doppler resolution. Using the definition of MIMO ambiguity function (4.2), we have

$$\chi(\tau,\nu,f,f') = \sum_{m=0}^{M-1}\sum_{m'=0}^{M-1} r^{\phi}_{m,m'}(\tau)e^{j2\pi(fm-f'm')\gamma} \cdot \sum_{l=0}^{L-1} e^{j2\pi\nu T_l},$$

for $|\tau| < \min_{l,l'}(|T_l - T_{l'}|) - T_\phi$.

The preceding analysis clearly shows how the problem of waveform design should be approached. The MIMO ambiguity function depends on the cross correlation functions $r^{\phi}_{m,m'}(\tau)$. Also, the pulses $\{\phi_m(t)\}$ only affect the range and spatial resolution. They do not affect the Doppler resolution. Therefore, to obtain a sharp ambiguity function, we should design the pulses $\{\phi_m(t)\}$ such that the function

$$\Omega(\tau,f,f') \triangleq \sum_{m=0}^{M-1}\sum_{m'=0}^{M-1} r^{\phi}_{m,m'}(\tau)e^{j2\pi(fm-f'm')\gamma} \tag{4.22}$$

is sharp around the line $\{(\tau,f,f')\big|\tau=0, f=f'\}$. For $M=1$, the signal design problem reduces to the special case of the SIMO radar. In this case, Eq. (4.22) reduces to the autocorrelation function

$$\Omega(\tau,f,f') = r^{\phi}_{0,0}(\tau).$$

Thus in the SIMO radar case, the signal design problem is to generate a pulse with a sharp autocorrelation. The linear frequency modulation (LFM) signal is an example which has a sharp autocorrelation [62]. Besides its sharp autocorrelation function, the LFM pulse can be conveniently generated and it has constant modulus. These reasons make the LFM signal a very good candidate in a pulse repetition radar system. For the MIMO radar case which satisfies $M > 1$, we need to consider not only the autocorrelation functions but also the cross correlation functions between pulses such that $\Omega(\tau,f,f')$ can be sharp.

4.5 Frequency-Hopping Pulses

Instead of directly designing the pulses, we can impose some structures on the pulses and design the parameters of the pulses. As an example of this idea, we now consider the pulse generated by frequency-hopping codes. In this section, we derive the MIMO radar ambiguity function of the

frequency-hopping pulses. These pulses have the advantage of constant modulus. The frequency-hopping pulses can be expressed as

$$\phi_m(t) = \sum_{q=0}^{Q-1} e^{j2\pi c_{m,q}\Delta f t} s(t - q\Delta t), \tag{4.23}$$

where

$$s(t) \triangleq \begin{cases} 1, & t \in [0, \Delta t) \\ 0, & \text{otherwise,} \end{cases}$$

$c_{m,q} \in \{0, 1, \cdots, K-1\}$ is the frequency-hopping code, and Q is the length of the code. The duration of the pulse is $T_\phi = Q\Delta t$, and the bandwidth of the pulses is approximately

$$BW_\phi \approx (K-1)\Delta f + \frac{1}{\Delta t}.$$

In this chapter, we are interested in the design of orthogonal waveforms. To maintain orthogonality, the code $\{c_{m,q}\}$ could be constrained to satisfy

$$\begin{aligned} &c_{m,q} \neq c_{m',q}, \text{ for } m \neq m', \forall q \\ &\Delta t \Delta f = 1. \end{aligned} \tag{4.24}$$

Now instead of directly designing the pulses $\phi_m(t)$, the signal design problem becomes designing the code $c_{m,q}$ for $m = 0, 1, \cdots, M-1$ and $q = 0, 1, \cdots, Q-1$. Recall that our goal is to design the transmitted signals such that the function $\Omega(\tau, f, f')$ in (4.22) is sharp (as explained in Sec. 5). So, we are interested in the expression for the function $\Omega(\tau, f, f')$ in terms of $\{c_{m,q}\}$. To compute the function $\Omega(\tau, f, f')$, we first compute the cross correlation function $r^{\phi}_{m,m}(\tau)$. By using (4.23) and (4.20), this can be expressed as

$$\begin{aligned} &r^{\phi}_{m,m'}(\tau) = \\ &\sum_{q=0}^{Q-1}\sum_{q'=0}^{Q-1} \chi^{\text{rect}}\big(\tau - (q'-q)\Delta t, (c_{m,q} - c_{m',q'})\Delta f\big) \\ &\cdot e^{j2\pi\Delta f(c_{m,q} - c_{m',q'})q\Delta t} e^{j2\pi\Delta f c_{m',p'}\tau}, \end{aligned} \tag{4.25}$$

where $\chi^{\text{rect}}(\tau,\nu)$ is the SIMO ambiguity function of the rectangular pulse $s(t)$, given by

$$\chi^{\text{rect}}(\tau,\nu) \triangleq \int_0^{\Delta t} s(t)s(t+\tau)e^{j2\pi\nu}dt \tag{4.26}$$
$$= \begin{cases} \frac{\Delta t-|\tau|}{\Delta t}\text{sinc}\left(\nu(\Delta t-|\tau|)\right)e^{j\pi\nu(\tau+\Delta t)}, \text{if } |\tau|<\Delta t \\ 0, \text{otherwise.} \end{cases}$$

Substituting (4.25) into (4.22), we obtain

$$\Omega(\tau,f,f') = \sum_{m,m'=0}^{M-1}\sum_{q,q'=0}^{Q-1}\chi^{\text{rect}}\big(\tau-(q'-q)\Delta t,(c_{m,q}-c_{m',q'})\Delta f\big) \cdot e^{j2\pi\Delta f(c_{m,q}-c_{m',q'})q\Delta t}e^{j2\pi\Delta f c_{m',q'}\tau}e^{j2\pi(fm-f'm')}.$$

Define $\tau = k\Delta t+\eta$, where $|\eta|<\Delta t$. By using the fact that $\chi^{\text{rect}}(\tau,\nu)=0$ when $|\tau|>\Delta t$, the above equation can be further simplified as

$$\Omega(k\Delta t+\eta,f,f') = \sum_{m,m'=0}^{M-1}\sum_{q=0}^{Q-1}\chi^{\text{rect}}\big(\eta,(c_{m,q}-c_{m',q+k})\Delta f\big) \cdot e^{j2\pi\Delta f c_{m',q+k}(k\Delta t+\eta)}e^{j2\pi\Delta f(c_{m,q}-c_{m',q+k})q\Delta t} \cdot e^{j2\pi(fm-f'm')\gamma}. \tag{4.27}$$

The next step is to choose the frequency-hopping code $\{c_{m,q}\}$ such that the function $\Omega(\tau,f,f')$ is sharp around $\{0,f,f\}$. We will discuss this in the following section.

4.6 Optimization of the Frequency-Hopping Codes

In this section, we introduce an algorithm to search for frequency-hopping codes which generate good MIMO ambiguity functions. By using (4.22) and the orthogonality of the waveforms, we have

$$\Omega(0,f,f) = \sum_{m,m'=0}^{M-1}\delta_{m,m'}e^{j2\pi f\gamma(m-m')} = M.$$

So, we know that the function $\Omega(\tau,f,f)$ is a constant along the line $\{0,f,f\}$, no matter what codes are chosen. To obtain good system resolutions, we need to eliminate the peaks in $|\Omega(\tau,f,f')|$ which

are not on the line $\{0, f, f\}$. This can be done by imposing a cost function which puts penalties on these peak values. This forces the energy of the function $\Omega(\tau, f, f')$ to be evenly spread in the delay and angular dimensions. As an example of this, we minimize the p-norm of the function $\Omega(\tau, f, f')$. The corresponding optimization problem can be expressed as

$$\begin{aligned} &\min_{\mathbf{C}} f_p(\mathbf{C}) \\ &\text{subject to} \quad \mathbf{C} \in \{0, 1, \cdots, K-1\}^{MQ} \\ &\qquad\qquad c_{m,q} \neq c_{m',q}, \text{ for } m \neq m', \end{aligned} \tag{4.28}$$

where

$$f_p(\mathbf{C}) \triangleq \int_{-\infty}^{\infty} \int_0^1 \int_0^1 |\Omega(\tau, f, f')|^p df df' d\tau, \tag{4.29}$$

and $c_{m,q}$ denotes the (m, q) entry of the matrix $\mathbf{C}$. Note that a greater p imposes more penalty on the higher peaks. The feasible set of this problem is a discrete set. It is known that the simulated annealing algorithm is very suitable for solving this kind of problem [54]. The simulated annealing algorithm runs a Markov chain Monte Carlo (MCMC) sampling on the discrete feasible set [76]. The transition probability of the Markov chain can be chosen so that the equilibrium of the Markov chain is

$$\begin{aligned} \pi_T(\mathbf{C}) &= \frac{1}{Z_T} \exp(\frac{-f_p(\mathbf{C})}{T}), \text{ where} \\ Z_T &= \sum_{\mathbf{C}} \exp(\frac{-f_p(\mathbf{C})}{T}). \end{aligned} \tag{4.30}$$

Here T is a parameter called temperature. By running the MCMC and gradually decreasing the temperature T, the generated sample $\mathbf{C}$ will have a high probability to have a small cost function output [54]. In our case, the transition probability from state $\mathbf{C}$ to $\mathbf{C}'$ is chosen as

$$p(\mathbf{C}, \mathbf{C}') = \begin{cases} \frac{1}{d} \min(1, \exp(\frac{f_p(\mathbf{C}) - f_p(\mathbf{C}')}{T})), & \text{if } \mathbf{C}' \sim \mathbf{C} \\ 1 - \frac{1}{d} \sum_{\mathbf{C}'' \sim \mathbf{C}} \min(1, \exp(\frac{f_p(\mathbf{C}) - f_p(\mathbf{C}'')}{T})), & \text{if } \mathbf{C}' = \mathbf{C} \\ 0, & \text{otherwise,} \end{cases}$$

where $\mathbf{C}' \sim \mathbf{C}$ denotes that $\mathbf{C}'$ and $\mathbf{C}$ differ in exactly one element, and d denotes $\left|\{\mathbf{C}' \middle| \mathbf{C}' \sim \mathbf{C}\}\right|$. It can be shown that the chosen transition probabilities result in the desired equilibrium in (4.30) [76]. The corresponding MCMC sampling can be implemented as the following algorithm.

Algorithm 3 *Given number of waveforms M, length of the code Q, number of frequencies K, initial temperature T, and a temperature decreasing ratio $\alpha \in (0,1)$, the code $\mathbf{C} \in \{0,1,\cdots,K-1\}^{MQ}$ can be computed by the following steps:*

1. *Randomly draw $\mathbf{C}$ from $\{0,1,\cdots,K-1\}^{MQ}$*
   such that $c_{mq} \neq c_{m'q}$ for $m \neq m$.
2. *Randomly draw m from $\{0,1,\cdots,M-1\}$*
   and q from $\{0,1,\cdots,Q-1\}$.
3. *Randomly draw k from $\{0,1,\cdots,K-1\} \setminus c_{mq}$.*
4. $\mathbf{C}' \leftarrow \mathbf{C}, c'_{mq} \leftarrow K$.
5. *Randomly draw U from $[0,1]$.*
6. *If $U < \exp\left(\dfrac{f_p(\mathbf{C}) - f_p(\mathbf{C}')}{T}\right)$, $\mathbf{C} \leftarrow \mathbf{C}'$.*
7. *If the cost $f_p(\mathbf{C})$ is small enough, stop.*
   else $T \leftarrow \alpha T$ and go to Step 2.

4.7 Design Examples

In this section, we present a design example using the proposed method. In this example, we consider a uniform linear transmitting array. The number of transmitted waveforms M equals 4. The length of the frequency-hopping code Q equals 10. The number of frequencies K equals 15. Without loss of generality, we normalize the pulse duration T_ϕ to be unity. By using (4.24), we obtain that the time-bandwidth product

$$\left((K-1)\Delta f + \frac{1}{\Delta t}\right) Q\Delta t = 150.$$

Note that this implies the maximum number of orthogonal waveform obtainable is $BT = 150$ [80]. So, our choice of $M = 4$ orthogonal waveforms is well under the theoretical limit. The cost function in (4.29) can be approximated by a Riemann sum. By applying the symmetry given by Property 8,

we can integrate only the part that has $\tau \geq 0$. Fig. 4.5 shows the real parts and the spectrograms of the waveforms generated by the proposed algorithm. For comparison Fig. 4.6 shows the real parts

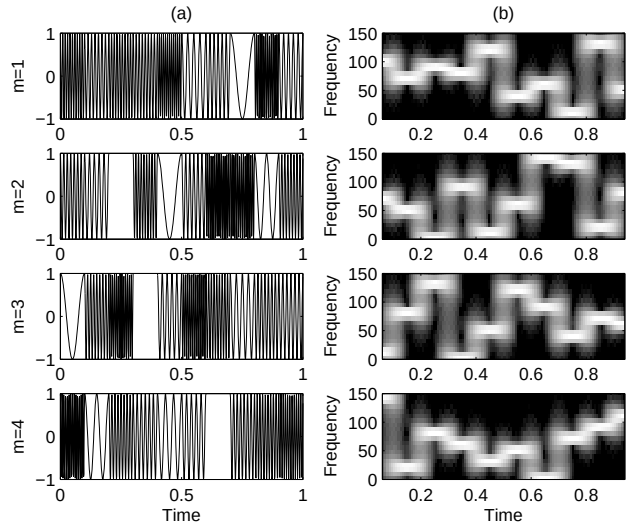

Figure 4.5: (a) Real parts and (b) spectrograms of the waveforms obtained by the proposed method

and the spectrograms of orthogonal LFM waveforms. In this example, these LFM waveforms have the form

$$\phi_m(t) = \exp(j2\pi f_{m,0}t + j\pi kt^2),$$

where $k = 100$, $f_{0,0} = 0$, $f_{1,0} = \lfloor \frac{50}{3} \rfloor$, $f_{2,0} = \lfloor \frac{100}{3} \rfloor$, and $f_{3,0} = 50$. By choosing different initial frequencies, these LFM waveforms can be made orthogonal. These parameters are chosen so that these LFM waveforms occupy the same time duration and bandwidth as the waveforms generated by the proposed method. Fig. 4.7 shows a result of comparing the functions $|\Omega(\tau, f, f')|$. We take samples from the function $|\Omega(\tau, f, f')|$ and plot their empirical cumulative distribution function (ECDF). In other words, this figure shows the percentage of samples of $|\Omega(\tau, f, f')|$ less than various magnitude. We have normalized the highest peak to 0 dB. The results of the proposed method, randomly generated frequency-hopping codes, and the LFM waveforms are compared in the figure. One can see that the proposed frequency-hopping signals yield fewest undesired peaks among all the waveforms. The video which shows the entire function $|\Omega(\tau, f, f')|$ (a plot in (f, f') plane as a function of time τ) can be viewed from [112]. Fig. 4.8 shows the cross correlation functions

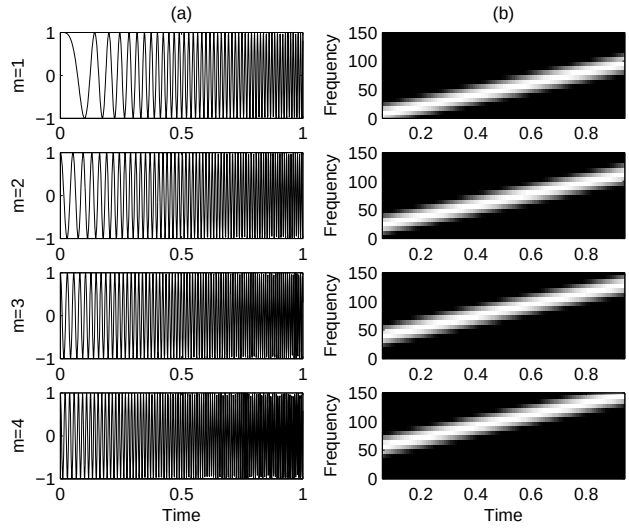

Figure 4.6: (a) Real parts and (b) spectrograms of the orthogonal LFM waveforms

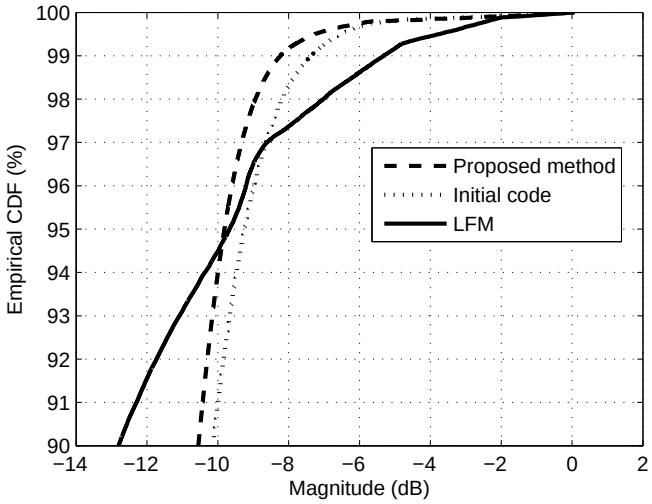

Figure 4.7: Empirical cumulative distribution function of $|\Omega(\tau, f, f')|$

$r^{\phi}_{m,m'}(\tau)$ of the waveforms generated by the proposed algorithm. Fig. 4.9 shows the cross correla-

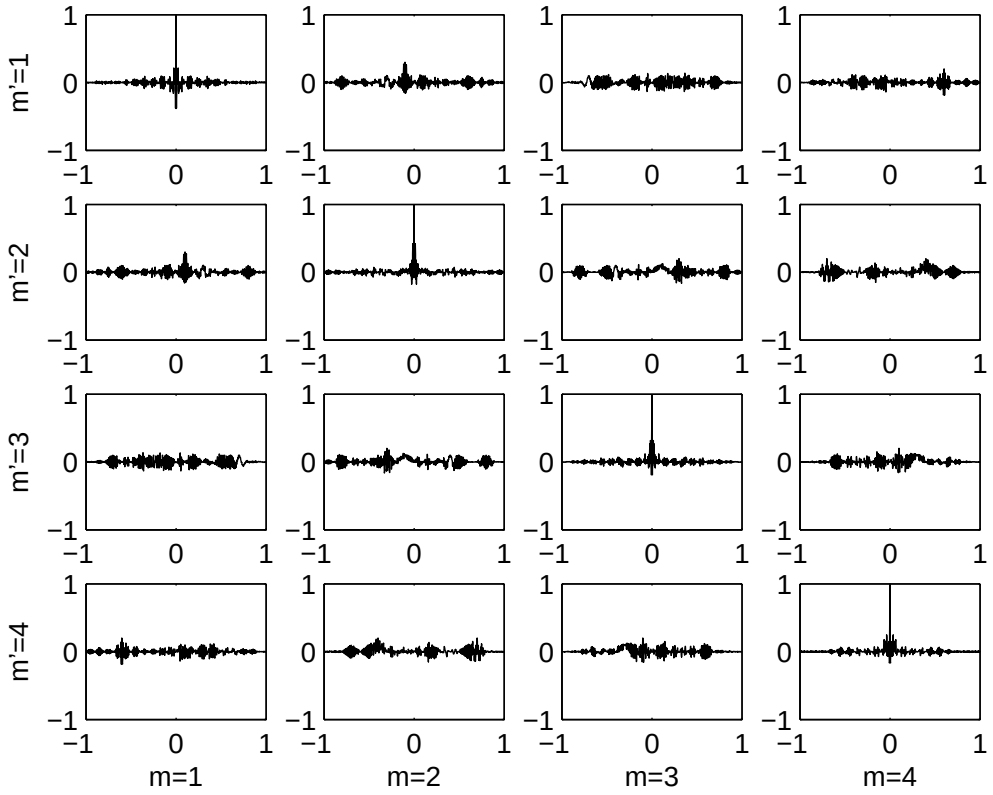

Figure 4.8: Cross-correlation functions $r^{\phi}_{m,m'}(\tau)$ of the waveforms generated by the proposed method

tion functions $r^{\phi}_{m,m'}(\tau)$ of the LFM waveforms. One can observe that for the proposed waveforms, the correlation functions $r^{\phi}_{m,m'}(\tau)$ equal to unity when $m = m'$ and $\tau = 0$. Except at these points, the correlation functions are small everywhere. However, for the LFM waveforms, the correlation functions have several extraneous peaks which also form peaks in the ambiguity function.

4.8 Conclusions

In this chapter, we have derived several properties of the MIMO radar ambiguity function and the cross ambiguity function. These results are derived for the ULA case. To summarize, Property 1, 2, and 6 characterize the MIMO radar ambiguity function along the line $\{(0, 0, f, f)\}$. Properties

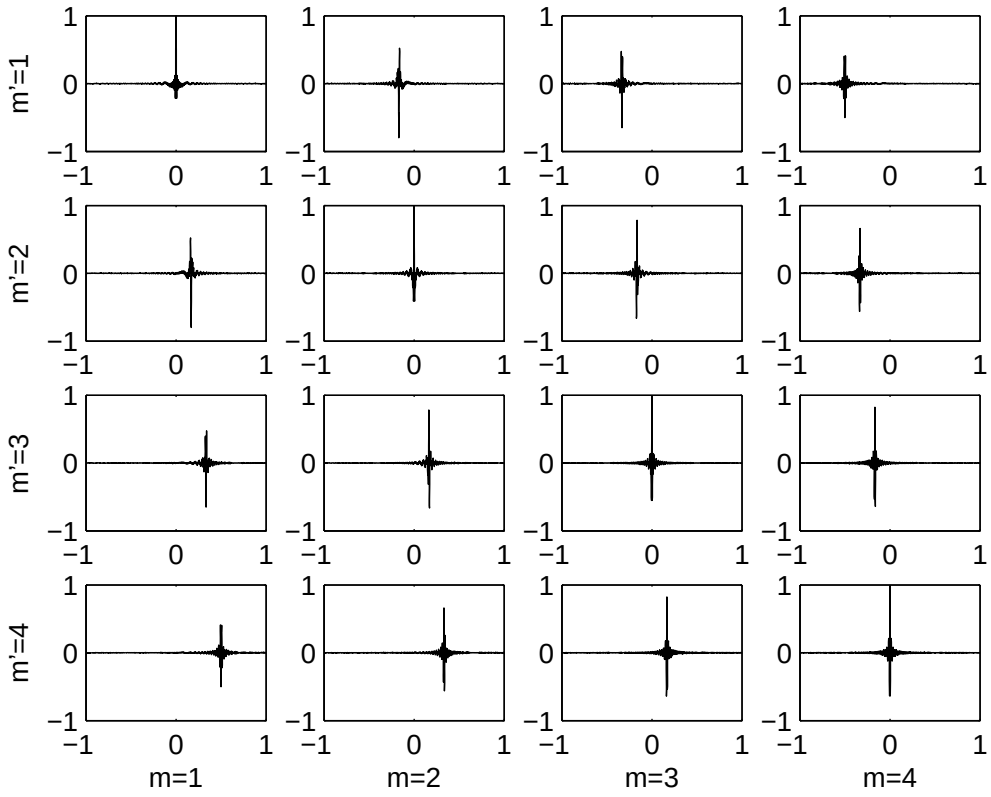

Figure 4.9: Cross correlation functions $r^{\phi}_{m,m'}(\tau)$ of the LFM waveforms

3, 4, and 5 characterize the energy of the cross ambiguity function and the MIMO radar ambiguity function. These properties imply that we can only spread the energy of the MIMO radar ambiguity function evenly on the available time and bandwidth because the energy is confined. Properties 7 and 8 show the symmetry of the cross ambiguity function and the MIMO radar ambiguity function. These properties imply that when we design the waveform, we only need to focus on the region $\{(\tau, \nu, f, f')|\tau \geq 0\}$ of the MIMO radar ambiguity function. Property 9 and 10 show the shear-off effect of the LFM waveform. This shearing improves the range resolution. We have also introduced a waveform design method for MIMO radars. This method is applicable to the case where the transmitted waveforms are orthogonal and consist of multiple shifted narrow pulses. The proposed method applies the simulated annealing algorithm to search for the frequency-hopping codes which minimize the p-norm of the ambiguity function. The numerical examples show that the waveforms generated by this method provide better angular and range resolutions than the LFM waveforms which have often been used in the traditional SIMO radar systems. In this chapter, we have presented the results only for the case of linear arrays. Nevertheless it is possible to further generalize these results for multi-dimensional arrays.

Chapter 5

Waveform Optimization of the MIMO Radar for Extended Target and Clutter

In this chapter, we consider the joint optimization of waveforms and receiving filters in the MIMO radar for the case of extended target in clutter. An extended target can be viewed as a collection of infinite number of point targets. While a point target is characterized by a scalar RCS (radar cross section), an extended target can be characterized by an impulse response. A novel iterative algorithm is proposed to optimize the waveforms and receiving filters such that the detection performance can be maximized. The corresponding iterative algorithms are also developed for the case where only the statistics or the uncertainty set of the target impulse response is available. These algorithms guarantee that the SINR performance improves in each iteration step. Numerical results show that the proposed methods have better SINR performance than existing design methods. Most of the results of this chapter have been reported in our recent journal paper [18].

5.1 Introduction

The MIMO radar waveform design problems have been studied in [16, 36–38, 68, 69, 71, 72, 94, 95, 108, 109]. These methods can be broken into three categories: (1) covariance matrix based design [37, 38, 68, 94, 95], (2) radar ambiguity function based design [16, 69, 71, 72], and (3) extended target based design [36, 108, 109]. In the covariance matrix based design methods, the covariance matrix of the waveforms are considered instead of the entire waveform. Consequently, this kind of design methods affects only the spatial domain. In [37, 38], the covariance matrix of the transmitted waveforms is designed such that the power can be transmitted to a desired range of angles. In [94], the authors have also designed the covariance matrix of the transmitted waveforms to con-

trol the spatial power. However, in [94], the cross-correlation between the transmitted signals at a number of given target locations is minimized. This can further increase the spatial resolution in the receiver. In [68], the covariances between waveforms have been optimized for several design criteria based on the Cramér-Rao bound matrix. In [95], given the optimized covariance matrix, the corresponding signal waveforms are designed to further achieve low PAR (peak-to-average-power ratio) and higher range resolution.

The radar ambiguity function based methods optimize the entire waveforms instead of just their covariances. Thus these design methods involve not only the spatial domain but also the range domain. The angle-Doppler-range resolution of the radar system can be characterized by the MIMO radar ambiguity function [2,83,89]. In [69,71,72], the sidelobe of the autocorrelation and the cross correlation between waveforms are minimized. This sharpens the radar ambiguity function. In [16], the waveforms are directly optimized so that a sharper radar ambiguity function can be obtained. Thus the spatial and range resolution of point targets can be improved.

In the extended target based methods also, the entire waveform is considered as in the radar ambiguity function based approaches. However, unlike the ambiguity function based methods which consider the resolutions of point targets, these methods consider the detection or estimation of *extended* targets. These methods require some prior information about the target and/or clutter impulse response. The extended target based methods have been also studied in the SIMO case [5, 21–24, 61, 65, 82]. In [65], the waveform is optimized to maximize the SINR subject to the constraint that the waveform is similar to a desired waveform. This constraint improves the PAR, and the range resolution of the waveform. In [21], the optimal radar code which considers detection probability, Doppler frequency estimation accuracy, PAR and the range resolution is proposed. In [5,61], the mutual information between the received waveforms and the target impulse response has been optimized by properly designing the transmitting waveforms. This idea has been extended to the MIMO radar case in [108]. The corresponding robust design has also been proposed in [109]. However, in [5, 21, 61, 65, 108, 109] the effect of the clutter is ignored. In [22–24, 82], the clutter impulse response has been considered. In these methods, the SINR has been maximized to improve the detection performance by properly designing the transmitting waveform. Both [82] and [22] have proposed different iterative algorithms to maximize the SINR. In [82], Pillai et al. have proven that in the continuous-time SIMO radar case, the optimal transmitted waveform must be minimum-phase. For the MIMO radar, SINR maximization with both target and clutter infor-

mation has been considered in [36]. A MIMO extension of the method in [82] and a gradient based method have been proposed in [36] to solve for the transmitted waveforms. Several suboptimal solutions have also been studied in [36].

In this chapter, we consider the waveform design problem which maximizes the SINR in the presence of clutter in the colocated MIMO radar case. As shown in [22,36,82], the difficulty of this problem is that the objective function, namely the SINR, is not a convex function of the transmitted waveforms. Moreover, it cannot be easily solved by Lagrange multiplier methods. In [22,36,82], different iterative methods have been developed. In [22], the algorithm guarantees the SINR improves in each iterative step. However, it has not been extended to the MIMO case because the algorithm is based on the symmetry of the SIMO radar ambiguity function [62], which is no longer valid in the MIMO radar case. On the other hand, in [36,82], the algorithms work for the MIMO radar case. However they do not guarantee nondecreasing SINR in each iteration step. Consequently, these algorithms cannot guarantee convergence. In this chapter, we propose a new algorithm which works in the MIMO radar case and guarantees nondecreasing SINR in each iteration step. The numerical results show that it converges faster and has better SINR performances than the method in [36,82]. We also consider the case where only a partial information of the target impulse response is known. This includes the case where only the statistics of the target impulse response are given and the case where only an uncertainty set of the target impulse response is given. The corresponding iterative algorithms have been developed for both cases.

The extended target based waveform design problem is very different from other types of radar waveform design. It requires the knowledge of the clutter statistics and the target impulse response or its statistics. It also requires the transmitted waveforms to adapt to the changing statistics in real-time. Therefore it is more complicated than other methods. The clutter information can be estimated by previous received signals before the target appears. We assume the impulse response of the target of interest is known. The goal is to design the waveforms which are best suitable for detecting this particular target of interest. However, this assumption may not be practical because the target impulse response depends on the orientation of the target. Therefore, in Sec. 5.4, we discuss the case where only the statistics or the uncertainty set of the target impulse response is available. The optimal waveforms for the detection are the waveforms which lead to the greatest SINR. Thus, we consider the problem of maximizing the SINR with the total energy constraint. Some of the important design issues such as constant modulus and range resolution are not considered in this

chapter. From a practical stand-point, it is important that the radar transmitter has a low PAR (peak-to-average-power ratio). Also, the optimal waveforms obtained by the proposed method may not have good performance for range estimation. The waveform design problem which takes into account these important issues will be explored in the future.

The rest of this chapter is organized as follows Sec. 2 introduces the signal model, formulates the problem and reviews the existing algorithms. Sec. 3 proposes the new iterative algorithm for jointly designing the transmitted waveforms and the receiving filters. Sec. 4 proposes the iterative algorithms for random target and uncertain target cases. Sec. 5 shows the results of numerical simulations. Finally Sec. 6 concludes the chapter.

5.2 Problem Formulation and Review

Fig. 5.1 (a) illustrates the model used in this chapter. Consider a MIMO radar system with N_T

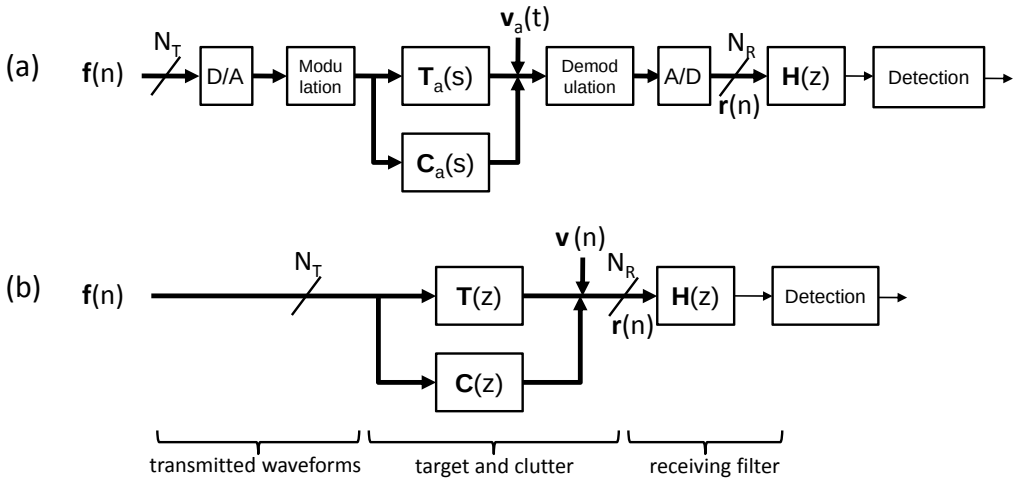

Figure 5.1: Illustration of (a) the signal model, and (b) the discrete baseband equivalent model

transmitting antennas and N_R receiving antennas. A finite duration $N_T \times 1$ vector signal $\mathbf{f}(n)$ is converted to analog waveforms, modulated, and emitted. The waveforms are reflected back by the target and clutter with transfer function $\mathbf{T}_a(s)$ and $\mathbf{C}_a(s)$, respectively. In the receiver, N_R waveforms are received, demodulated and converted back to a discrete vector signal $\mathbf{r}(n)$. Then the received signal $\mathbf{r}(n)$ is processed by a receiving filter $\mathbf{H}(z)$ to further determine the existence of the target. Fig. 5.1 (b) illustrates the discrete baseband equivalent model where $\mathbf{T}(z)$ and $\mathbf{C}(z)$

represent the transfer functions of the target and clutter respectively. We assume $\mathbf{T}(z)$ is a known FIR filter. It can be represented as

$$\mathbf{T}(z) = \sum_{n=0}^{L} \mathbf{t}(n) z^{-n},$$

where $\mathbf{t}(n) \in \mathbb{C}^{N_R \times N_T}$ is the impulse response of the target (i.e., $\mathbf{t}_{k,l}(n) =$ impulse response from the lth transmitting antenna to the kth receiving antenna) and L is the order of the FIR filter. The clutter transfer function can be represented as

$$\mathbf{C}(z) = \sum_{n=-\infty}^{\infty} \mathbf{c}(n) z^{-n},$$

where $\mathbf{c}(n) \in \mathbb{C}^{N_R \times N_T}$ is the impulse response of clutter. We assume $\text{vec}(\mathbf{c}(n))$ is a vector wide-sense stationary (WSS) process with known covariance

$$\mathbf{R}_c(m) \triangleq E[\text{vec}(\mathbf{c}(n))\text{vec}(\mathbf{c}(n-m))^\dagger]. \tag{5.1}$$

The $N_R \times 1$ vector process $\mathbf{v}(n)$ shown in Fig. 5.1 (b) represents the noise in the receiver. We also assume the covariance

$$\mathbf{R}_v(m) \triangleq E[\mathbf{v}(n)\mathbf{v}(n-m)^\dagger] \tag{5.2}$$

is known. The assumption of the availability of this prior information has also been made in [22–24, 36, 82].

With the prior information of the target impulse response and the second order statistics of the clutter impulse response and noise, our goal is to jointly design the $N_T \times 1$ transmitted vector waveform $\mathbf{f}(n)$ and the $N_R \times 1$ receiving filter $\mathbf{H}(z)$ to maximize the detection rate. It is well-known that the optimal detection can be obtained by the log-likelihood ratio test [100]. In this case, the detection rate is a nondecreasing function of the SINR. Therefore, our goal becomes to maximize the SINR by choosing $\mathbf{f}(n)$ and $\mathbf{H}(z)$. The single-input single-output (SISO) case of this problem, where $N_R = N_T = 1$, has been studied by DeLong and Hofstetter in 1967 [22–24] and more recently by Pillai et al. [82]. Two different types of iterative methods have been proposed for solving this problem. DeLong and Hofstetter's iterative method takes advantage of the symmetry property of the cross ambiguity function. This method guarantees the SINR improves in each iteration step.

Nevertheless, the symmetry property cannot be applied in the general MIMO case. Consequently this method cannot be generalized to the MIMO case. On the other hand, Pillai's method has been generalized to the MIMO case by Friedlander [36]. However, this method does not guarantee that the SINR improves in each iteration step. We will soon briefly review this method. In this chapter, we propose a new iterative method for optimizing the MIMO radar transceiver. It works in the MIMO case and also guarantees the SINR improves in every iteration step.

5.2.1 Problem Formulation

The received baseband waveform $\mathbf{r}(n)$ can be expressed as

$$\mathbf{r}(n) = \sum_{m=0}^{L_T} (\mathbf{t}(n-m) + \mathbf{c}(n-m)) \cdot \mathbf{f}(m) + \mathbf{v}(n),$$

where L_T is the order of the finite duration signal $\mathbf{f}(n)$. We define

$$\mathbf{r} \triangleq \left[\mathbf{r}(0)^T\ \mathbf{r}(1)^T \cdots \mathbf{r}(L_R)^T\right]^T \in \mathbb{C}^{N_R(L_R+1)\times 1},$$

where L_R is the order of the receiving filter $\mathbf{H}(z)$. Then the overall received signal can be expressed as

$$\mathbf{r} = (\mathbf{T} + \mathbf{C})\mathbf{f} + \mathbf{v},$$

where

$$\begin{aligned} \mathbf{f} &\triangleq \left[\mathbf{f}(0)^T\ \mathbf{f}(1)^T \cdots \mathbf{f}(L_T)^T\right]^T \in \mathbb{C}^{N_T(L_T+1)\times 1}, \\ \mathbf{v} &\triangleq \left[\mathbf{v}(0)^T\ \mathbf{v}(1)^T \cdots \mathbf{v}(L_R)^T\right]^T \in \mathbb{C}^{N_R(L_R+1)\times 1}, \end{aligned} \tag{5.3}$$

and $\mathbf{T}$ and $\mathbf{C}$ are block Toeplitz matrices defined as

$$\mathbf{T} \triangleq \begin{pmatrix} \mathbf{t}(0) & \mathbf{0} & \cdots & \mathbf{0} \\ \mathbf{t}(1) & \mathbf{t}(0) & \ddots & \vdots \\ \vdots & \mathbf{t}(1) & \ddots & \mathbf{0} \\ \mathbf{t}(L) & \vdots & \ddots & \mathbf{t}(0) \\ \mathbf{0} & \mathbf{t}(L) & \ddots & \mathbf{t}(1) \\ \vdots & \ddots & \ddots & \vdots \\ \mathbf{0} & \cdots & \mathbf{0} & \mathbf{t}(L) \end{pmatrix}, \tag{5.4}$$

and

$$\mathbf{C} \triangleq \begin{pmatrix} \mathbf{c}(0) & \mathbf{c}(-1) & \cdots & \mathbf{c}(-L_T) \\ \mathbf{c}(1) & \mathbf{c}(0) & \ddots & \vdots \\ \vdots & \mathbf{c}(1) & \ddots & \vdots \\ \vdots & \ddots & \ddots & \mathbf{c}(0) \\ \vdots & \ddots & \ddots & \mathbf{c}(1) \\ \vdots & \ddots & \ddots & \vdots \\ \mathbf{c}(L_R) & \mathbf{c}(L_R-1) & \cdots & \mathbf{c}(L) \end{pmatrix}.$$

Fig. 5.2 illustrates the FIR equivalent model, where the $N_R \times (L_R + 1)$ vector $\mathbf{h}$ consists of the impulse response of the receiving filter $\mathbf{H}(z)$. The receiving filter output can be expressed as

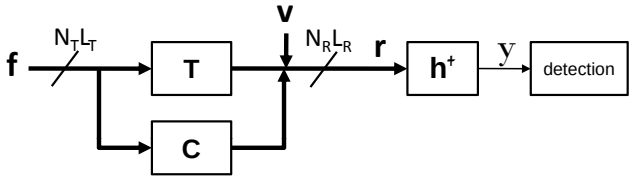

Figure 5.2: The FIR equivalent model

$$\mathbf{y} = \mathbf{h}^\dagger \mathbf{r} = \underbrace{\mathbf{h}^\dagger \mathbf{T}\mathbf{f}}_{\text{signal}} + \underbrace{\mathbf{h}^\dagger \mathbf{C}\mathbf{f}}_{\text{clutter}} + \underbrace{\mathbf{h}^\dagger \mathbf{v}}_{\text{noise}}.$$

Thus the SINR at the filter output can be expressed as

$$\rho(\mathbf{f},\mathbf{h}) \triangleq \frac{|\mathbf{h}^\dagger \mathbf{T}\mathbf{f}|^2}{E[|\mathbf{h}^\dagger \mathbf{C}\mathbf{f}|^2] + E[|\mathbf{h}^\dagger \mathbf{v}|^2]}. \tag{5.5}$$

Our goal is to maximize the SINR subject to the power constraint, that is,

$$\max_{\mathbf{f},\mathbf{h}} \rho(\mathbf{f},\mathbf{h}) \text{ subject to } \|\mathbf{f}\|^2 \leq 1. \tag{5.6}$$

One can first observe that this problem is in general not convex because the objective function is a fourth order rational function. In general, there will be multiple local maxima in the feasible set. It is in general not easy to find the global maximum.

5.2.2 Review of Pillai's method [82]

Now we briefly review the method proposed in [82] for solving the optimization problem in (5.6). Note that the original method proposed in [82] uses a continuous-time SISO model. We review a slightly modified version of this method which works in our discrete-time MIMO model as shown in Fig. 5.1 (b).

To solve the problem in (5.6), we can first solve $\mathbf{h}$ in terms of $\mathbf{f}$. In this case, the optimization problem becomes

$$\max_{\mathbf{h}} \frac{|\mathbf{h}^\dagger \mathbf{T}\mathbf{f}|^2}{\mathbf{h}^\dagger E[\mathbf{C}\mathbf{f}\mathbf{f}^\dagger \mathbf{C}^\dagger]\mathbf{h} + \mathbf{h}^\dagger E[\mathbf{v}\mathbf{v}^\dagger]\mathbf{h}}.$$

Define

$$\mathbf{R}_{c,f} \triangleq E[\mathbf{C}\mathbf{f}\mathbf{f}^\dagger \mathbf{C}^\dagger] \tag{5.7}$$

and $\mathbf{R}_v = E[\mathbf{v}\mathbf{v}^\dagger]$. Note that $\mathbf{R}_{c,f}$ can be obtained by using the clutter covariance $\mathbf{R}_c(m)$ in (5.1) and $\mathbf{R}_v$ can be obtained by using the noise covariance $\mathbf{R}_v(m)$ in (5.2). The above problem can be recast as

$$\min_{\mathbf{h}} \mathbf{h}^\dagger (\mathbf{R}_{c,f} + \mathbf{R}_v)\mathbf{h}$$
$$\text{subject to } \mathbf{h}^\dagger \mathbf{T}\mathbf{f} = 1.$$

This is the well-known minimum variance distortionless response (MVDR) problem [12]. The solution to this problem is

$$\mathbf{h} = \alpha(\mathbf{R}_{c,f} + \mathbf{R}_v)^{-1}\mathbf{T}\mathbf{f}. \tag{5.8}$$

where α is a scalar which satisfies the equality constraint. Note that the scalar can be ignored because it has no effect on the original objective function in (5.5).

Substituting the above $\mathbf{h}$ back into the objective function in (5.5). The new objective function becomes $\mathbf{f}^\dagger\mathbf{T}^\dagger(\mathbf{R}_{c,f} + \mathbf{R}_v)^{-1}\mathbf{T}\mathbf{f}$ which is a function of $\mathbf{f}$ only. Therefore the optimization problem becomes

$$\begin{aligned} &\max_{\mathbf{f}} \mathbf{f}^\dagger\mathbf{T}^\dagger(\mathbf{R}_{c,f} + \mathbf{R}_v)^{-1}\mathbf{T}\mathbf{f} \\ &\text{subject to } \|\mathbf{f}\|^2 \leq 1. \end{aligned} \tag{5.9}$$

Now this problem has only one parameter $\mathbf{f}$. If $\mathbf{R}_{c,f}$ is a constant, the above problem is the well-known Rayleigh quotient [48] and the solution to $\mathbf{f}$ will be the principal component of the matrix $\mathbf{T}^\dagger(\mathbf{R}_{c,f} + \mathbf{R}_v)^{-1}\mathbf{T}$. However, note that from (5.7), $\mathbf{R}_{c,f}$ is a function of $\mathbf{f}$ as well. To solve this problem, Pillai et al. proposed a method which starts with an initial $\mathbf{f}$ and then uses this $\mathbf{f}$ to compute the matrix $\mathbf{T}^\dagger(\mathbf{R}_{c,f} + \mathbf{R}_v)^{-1}\mathbf{T}$. Then the principal component of this matrix is computed to update $\mathbf{f}$. This process is repeated until the SINR is large enough. As we have shown here, this method can be used in the MIMO case. Nevertheless, this method does not guarantee nondecreasing SINR in each iteration step. Consequently, the convergence cannot be guaranteed.

5.3 Proposed Iterative Method

In this section, a new iterative algorithm is introduced for solving the SINR maximization problem in (5.6). Different from the approach in [82], this proposed method guarantees nondecreasing SINR in each iteration step. The technique applied here is that we first optimize the receiving filter $\mathbf{h}$ for fixed transmitted waveforms $\mathbf{f}$ and then optimize $\mathbf{f}$ for fixed receiving filter $\mathbf{h}$. This kind of optimization technique has been applied in different fields such as multiuser transceiver design [90], multicarrier transceiver design [81], and adaptive paraunitary filterbank design [97]. It can be shown that the algorithm gives a solution which is not only a local optimum, but also the global

optimum *separately* along the $\mathbf{f}$ dimension and the $\mathbf{h}$ dimension.

We have already solved $\mathbf{h}$ in terms of $\mathbf{f}$ in (5.8). Now we explain how to solve $\mathbf{f}$ in terms of $\mathbf{h}$ and then we will explain the iterative process. For fixed $\mathbf{h}$, the transmitted waveforms $\mathbf{f}$ can be obtained by solving the following optimization problem

$$\begin{aligned} &\max_{\mathbf{f}} \frac{|\mathbf{h}^\dagger \mathbf{T}\mathbf{f}|^2}{\mathbf{f}^\dagger \mathbf{R}_{c,h}\mathbf{f} + \mathbf{h}^\dagger \mathbf{R}_v \mathbf{h}} \\ &\text{subject to } \|\mathbf{f}\|^2 \leq 1, \end{aligned} \tag{5.10}$$

where $\mathbf{R}_{c,h} \triangleq E[\mathbf{C}^\dagger \mathbf{h}\mathbf{h}^\dagger \mathbf{C}]$ and $\mathbf{R}_v \triangleq E[\mathbf{v}\mathbf{v}^\dagger]$. Note that both $\mathbf{R}_{c,h}$ and $\mathbf{R}_v$ can be obtained by using the prior second order information defined in (5.1) and (5.2). We first look at the Lagrange multiplier method to solve this problem. The Lagrangian can be defined as

$$L(\mathbf{f}, \lambda) \triangleq \frac{|\mathbf{h}^\dagger \mathbf{T}\mathbf{f}|^2}{\mathbf{f}^\dagger \mathbf{R}_{c,h}\mathbf{f} + \mathbf{h}^\dagger \mathbf{R}_v \mathbf{h}} + \lambda(\mathbf{f}^\dagger \mathbf{f} - 1),\ \lambda \geq 0,$$

where λ is the Lagrange multiplier. Differentiating the above function with respect to $\mathbf{f}$ and setting it to zero, we obtain

$$\frac{\mathbf{T}^\dagger \mathbf{h}\mathbf{h}^\dagger \mathbf{T}\mathbf{f}(\mathbf{f}^\dagger \mathbf{R}_{c,h}\mathbf{f} + \mathbf{h}^\dagger \mathbf{R}_v \mathbf{h}) - |\mathbf{h}^\dagger \mathbf{T}\mathbf{f}|^2 \mathbf{R}_{c,h}\mathbf{f}}{(\mathbf{f}^\dagger \mathbf{R}_{c,h}\mathbf{f} + \mathbf{h}^\dagger \mathbf{R}_v \mathbf{h})^2} + \lambda \mathbf{f} = 0.$$

One can see that the above equation has a high order polynomial of $\mathbf{f}$ in the numerator. This makes it hard to solve in general.

We have already seen that directly solving the problem using the method of Lagrange multiplier is not easy. To overcome this difficulty, we recast the problem by using the following proposition.

Proposition 1. If $\mathbf{f}_\star$ solves the optimization problem

$$\max_{f} \frac{|\mathbf{h}^\dagger \mathbf{T}\mathbf{f}|^2}{\mathbf{f}^\dagger \mathbf{R}_{c,h}\mathbf{f} + \mathbf{h}^\dagger \mathbf{R}_v \mathbf{h} \cdot \mathbf{f}^\dagger \mathbf{f}} \tag{5.11}$$

then $\mathbf{f}_{\star\star} \triangleq \mathbf{f}_\star / \|\mathbf{f}_\star\|$ solves (5.10).

Proof: For any $\mathbf{f} \in \mathbb{C}^{N_T(L_T+1)\times 1}$ satisfying $\|\mathbf{f}\|^2 \leq 1$,

$$\begin{aligned} \frac{|\mathbf{h}^\dagger \mathbf{T}\mathbf{f}_{\star\star}|^2}{\mathbf{f}_{\star\star}^\dagger \mathbf{R}_{c,h}\mathbf{f}_{\star\star} + \mathbf{h}^\dagger \mathbf{R}_v \mathbf{h}} &= \frac{|\mathbf{h}^\dagger \mathbf{T}\mathbf{f}_\star|^2}{\mathbf{f}_\star^\dagger \mathbf{R}_{c,h}\mathbf{f}_\star + \mathbf{h}^\dagger \mathbf{R}_v \mathbf{h} \cdot \mathbf{f}_\star^\dagger \mathbf{f}_\star} \\ \geq \frac{|\mathbf{h}^\dagger \mathbf{T}\mathbf{f}|^2}{\mathbf{f}^\dagger \mathbf{R}_{c,h}\mathbf{f} + \mathbf{h}^\dagger \mathbf{R}_v \mathbf{h} \cdot \mathbf{f}^\dagger \mathbf{f}} &\geq \frac{|\mathbf{h}^\dagger \mathbf{T}\mathbf{f}|^2}{\mathbf{f}^\dagger \mathbf{R}_{c,h}\mathbf{f} + \mathbf{h}^\dagger \mathbf{R}_v \mathbf{h}}. \end{aligned}$$

The first inequality is because of the definition of $\mathbf{f}_\star$. The second inequality is from the fact that $\|\mathbf{f}\|^2 \leq 1$. We also have $\|\mathbf{f}_{\star\star}\|^2 \leq 1$. Therefore $\mathbf{f}_{\star\star}$ is a solution to (5.10). ■

Similar technique has been used in [90] to solve an MSE minimization problem in multiuser transceivers. This proposition allows us to get rid of the power constraint in (5.10) and solve the unconstrained problem in (5.11) instead. Eq. (5.11) can be further recast as the MVDR problem

$$\begin{aligned} &\min_{\mathbf{f}} \mathbf{f}^\dagger(\mathbf{R}_{c,h} + \mathbf{h}^\dagger\mathbf{R}_v\mathbf{h}\cdot\mathbf{I})\mathbf{f} \\ &\text{subject to } \mathbf{h}^\dagger\mathbf{T}\mathbf{f} = 1. \end{aligned}$$

The solution to the above problem is [12]

$$\mathbf{f} = \alpha(\mathbf{R}_{c,h} + \mathbf{h}^\dagger\mathbf{R}_v\mathbf{h}\cdot\mathbf{I})^{-1}\mathbf{T}^\dagger\mathbf{h}, \tag{5.12}$$

where α is a scalar which satisfies the power constraint. Note that this scalar can be ignored because $\mathbf{f}$ needs to be normalized to unit norm according to Proposition 1.

Now we know how to solve $\mathbf{h}$ in terms of $\mathbf{f}$ and $\mathbf{f}$ in terms of $\mathbf{h}$. We can iteratively solve for the transmitted waveforms $\mathbf{f}$ and the receiving filter $\mathbf{h}$. Thus the objective function, namely SINR, will be nondecreasing in every iteration step. The algorithm is summarized as follows.

Algorithm 1. Given the target impulse response $\mathbf{T}(z)$, noise covariance $\mathbf{R}_v(m)$, the clutter covariance $\mathbf{R}_c(m)$, and an initial value of the transmitted waveforms $\mathbf{f}$, the transceiver pair $(\mathbf{f}, \mathbf{h})$ can be optimized by repeating the following steps:

1. Compute $\mathbf{R}_{c,f} = E[\mathbf{C}\mathbf{f}\mathbf{f}^\dagger\mathbf{C}^\dagger]$
2. $\mathbf{h} \leftarrow (\mathbf{R}_{c,f} + \mathbf{R}_v)^{-1}\mathbf{T}\mathbf{f}$
3. Compute $\mathbf{R}_{c,h} = E[\mathbf{C}^\dagger\mathbf{h}\mathbf{h}^\dagger\mathbf{C}]$
4. $\mathbf{f} \leftarrow (\mathbf{R}_{c,h} + \mathbf{h}^\dagger\mathbf{R}_v\mathbf{h}\cdot\mathbf{I})^{-1}\mathbf{T}^\dagger\mathbf{h}$
5. $\mathbf{f} \leftarrow \mathbf{f}/\|\mathbf{f}\|$.

We stop when the SINR improvement becomes insignificant. Because the objective function is bounded and is nondecreasing in each step, according to monotone convergence theorem the ob-

jective function will converge to some value $\Phi_\star$ [110]. Even though the point $(\mathbf{f}, \mathbf{h})$ corresponding to this result $\Phi_\star$ is not unique, the algorithm stops in one paticular $(\mathbf{f}_\star, \mathbf{h}_\star)$ yielding $\Phi_\star$. Since $\mathbf{f}_\star$ and $\mathbf{h}_\star$ are local optimum along $\mathbf{f}$ and $\mathbf{h}$ dimension separately, the solution $(\mathbf{f}_\star, \mathbf{h}_\star)$ is also a local optimum, that is,

$$\begin{aligned} &\exists \epsilon > 0 \text{ such that} \\ &\rho(\mathbf{f}_\star, \mathbf{h}_\star) \geq \rho(\mathbf{f}, \mathbf{h}), \forall \, \|\mathbf{f} - \mathbf{f}_\star\|^2 + \|\mathbf{h} - \mathbf{h}_\star\|^2 \leq \epsilon. \end{aligned}$$

Moreover, the algorithm finds the global maximum along $\mathbf{f}$ dimension or $\mathbf{h}$ dimension in each step. Therefore, when the algorithm converges, the solution $(\mathbf{f}_\star, \mathbf{h}_\star)$ will be the global optimum along the $\mathbf{f}$ dimension and $\mathbf{h}$ dimension separately, that is,

$$\begin{aligned} \rho(\mathbf{f}_\star, \mathbf{h}_\star) &\geq \rho(\mathbf{f}_\star, \mathbf{h}), \forall \, \mathbf{h} \\ \rho(\mathbf{f}_\star, \mathbf{h}_\star) &\geq \rho(\mathbf{f}, \mathbf{h}_\star), \forall \, \|\mathbf{f}\|^2 \leq 1. \end{aligned}$$

So, the solution obtained by this iterative algorithm is actually stronger than a local maximum.

Matched Filter Bound.

To evaluate the performance of the suboptimal iterative algorithm, we are interested in how close its SINR performance is to the global optimal solution of the problem in (5.6). However, it does not appear to be a simple matter to obtain the global optimal solution. To avoid this difficulty, we compare the performance of the proposed method to a computable upper bound of the global maximum. One way to obtain such an upper bound is to drop the clutter term in the SINR expression in (5.5). This bound is often called the matched filter bound. It can be expressed as:

$$\max_{\mathbf{f},\mathbf{h}} \frac{|\mathbf{h}^\dagger \mathbf{T} \mathbf{f}|^2}{\mathbf{h}^\dagger \mathbf{R}_v \mathbf{h}} \text{ subject to } \|\mathbf{f}\|^2 \leq 1.$$

One can first solve $\mathbf{h}$ in terms of $\mathbf{f}$ as in (5.8) and obtain

$$\mathbf{h} = \alpha \mathbf{R}_v^{-1} \mathbf{T} \mathbf{f},$$

where α is a scalar which will be determined by the power constraint. Substituting the above

solution into the objective function, the optimization problem becomes

$$\max_{\mathbf{f}} \mathbf{f}^\dagger \mathbf{T}^\dagger \mathbf{R}_v^{-1} \mathbf{T}\mathbf{f} \text{ subject to } \|\mathbf{f}\|^2 \leq 1.$$

This is the well-known Rayleigh quotient [48]. The solution of $\mathbf{f}$ is the principal component of the matrix $\mathbf{T}^\dagger \mathbf{R}_v^{-1} \mathbf{T}$ and the maximum of the objective function is the largest eigenvalue of $\mathbf{T}^\dagger \mathbf{R}_v^{-1} \mathbf{T}$ which is denoted as

$$\lambda_1(\mathbf{T}^\dagger \mathbf{R}_v^{-1} \mathbf{T}).$$

Therefore, this matched filter bound can be easily obtained. The numerical results for the proposed iterative method and the matched filter bound will be presented in Sec. 5.5.

5.4 Iterative Method with Random and Uncertain Target Impulse Response

The iterative method introduced in Sec. 5.3 requires the information of the target impulse response $\mathbf{T}(z)$. In this section, we focus on the case where only a partial information of the target impulse response is available. We consider two different cases. In the first, the target impulse response is modelled as a WSS random process. We assume only the covariance of the process is known. An iterative algorithm for maximizing the SINR in this case will be derived in this section. In the second case, the target impulse response is deterministic but unknown. We assume the target impulse response lies in a convex uncertainty set. An iterative algorithm will be proposed in this section to maximize the worst SINR among all the possible target impulse responses in the given uncertainty set.

5.4.1 Random Target Impulse Response

We first consider the random target impulse response case. We assume the coefficients of the target impulse response vec($\mathbf{t}(n)$) is a WSS random process. We assume the covariance matrix, which is defined as

$$\mathbf{R}_t(m) \triangleq E[\text{vec}(\mathbf{t}(n))\text{vec}(\mathbf{t}(n-m))^\dagger]$$

is known. In this case, the SINR at the receiving filter output is defined as

$$\rho(\mathbf{f},\mathbf{h}) \triangleq \frac{E[|\mathbf{h}^\dagger \mathbf{T}\mathbf{f}|^2]}{E[|\mathbf{h}^\dagger \mathbf{C}\mathbf{f}|^2] + E[|\mathbf{h}\mathbf{v}|^2]}. \tag{5.13}$$

The goal is to solve the following optimization problem:

$$\max_{\mathbf{f},\mathbf{h}} \rho(\mathbf{f},\mathbf{h}) \text{ subject to } \|\mathbf{f}\|^2 \leq 1.$$

The same technique used in Sec. 5.3 can be used to iteratively optimize the parameters $\mathbf{h}$ and $\mathbf{f}$ in each step. To solve $\mathbf{h}$ in terms of $\mathbf{f}$, the optimization problem can be written as

$$\max_{\mathbf{h}} \frac{\mathbf{h}^\dagger \mathbf{R}_{t,f} \mathbf{h}}{\mathbf{h}^\dagger \mathbf{R}_{c,f} \mathbf{h} + \mathbf{h}^\dagger \mathbf{R}_v \mathbf{h}},$$

where $\mathbf{R}_{t,f} \triangleq E[\mathbf{T}\mathbf{f}\mathbf{f}^\dagger \mathbf{T}^\dagger]$, $\mathbf{R}_{c,f} \triangleq E[\mathbf{C}\mathbf{f}\mathbf{f}^\dagger \mathbf{C}^\dagger]$ and $\mathbf{R}_v \triangleq E[\mathbf{v}\mathbf{v}^\dagger]$. Define $\mathbf{L}_{c,f}$ as the lower triangular Cholesky factor of $\mathbf{R}_{c,f} + \mathbf{R}_v$. In other words, the lower triangular matrix $\mathbf{L}_{c,f}$ satisfies $\mathbf{L}_{c,f}\mathbf{L}_{c,f}^\dagger = \mathbf{R}_{c,f} + \mathbf{R}_v$. Define $\mathbf{x} \triangleq \mathbf{L}_{c,f}^\dagger \mathbf{h}$. By changing variables, the optimization problem can be rewritten as

$$\max_{\mathbf{x}} \frac{\mathbf{x}^\dagger \mathbf{L}_{c,f}^{-1} \mathbf{R}_{t,f} \mathbf{L}_{c,f}^{-\dagger} \mathbf{x}}{\mathbf{x}^\dagger \mathbf{x}}.$$

This is the well-known Rayleigh quotient [48] and the solution to the problem is the principal component of the matrix $\mathbf{L}_{c,f}^{-1} \mathbf{R}_{t,f} \mathbf{L}_{c,f}$. Thus, the solution $\mathbf{h}$ can be expressed as

$$\mathbf{h} = \mathbf{L}_{c,f}^{-\dagger} \cdot \mathbf{p}(\mathbf{L}_{c,f}^{-1} \mathbf{R}_{t,f} \mathbf{L}_{c,f}^{-\dagger}), \tag{5.14}$$

where $\mathbf{p}(\mathbf{A})$ denotes the principal component of matrix $\mathbf{A}$.

To solve $\mathbf{f}$ in terms of $\mathbf{h}$, the optimization problem becomes the following.

$$\max_{\mathbf{f}} \frac{\mathbf{f}^\dagger \mathbf{R}_{t,h} \mathbf{f}}{\mathbf{f}^\dagger \mathbf{R}_{c,h} \mathbf{f} + \mathbf{h}^\dagger \mathbf{R}_v \mathbf{h}}$$
$$\text{subject to } \|\mathbf{f}\|^2 \leq 1,$$

where $\mathbf{R}_{t,h} \triangleq E[\mathbf{T}^\dagger \mathbf{h}\mathbf{h}^\dagger \mathbf{T}]$ and $\mathbf{R}_{c,h} \triangleq E[\mathbf{C}^\dagger \mathbf{h}\mathbf{h}^\dagger \mathbf{C}]$. It can be easily verified that a similar result as in Proposition 1 still holds in this case. We can obtain the solution by solving the following problem

instead.

$$\max_{\mathbf{f}} \frac{\mathbf{f}^\dagger \mathbf{R}_{t,h} \mathbf{f}}{\mathbf{f}^\dagger \mathbf{R}_{c,h} \mathbf{f} + \mathbf{h}^\dagger \mathbf{R}_v \mathbf{h} \cdot \mathbf{f}^\dagger \mathbf{f}}.$$

Using the same technique for solving $\mathbf{h}$, we can obtain

$$\mathbf{f} = \mathbf{L}_{c,f}^{-\dagger} \cdot \mathbf{p}(\mathbf{L}_{c,f}^{-1} \mathbf{R}_{t,h} \mathbf{L}_{c,f}^{-\dagger}),$$

where $\mathbf{L}_{c,f}$ is the lower triangular matrix such that $\mathbf{L}_{c,f}\mathbf{L}_{c,f}^\dagger = \mathbf{R}_{c,h} + \mathbf{h}^\dagger \mathbf{R}_v \mathbf{h} \cdot \mathbf{I}$.

We summarize the iterative algorithm for optimizing the transceiver pair in the case of random target impulse response as the following.

Algorithm 2. Given the target impulse response covariance $\mathbf{R}_t(m)$, the clutter covariance $\mathbf{R}_c(m)$, the noise covariance $\mathbf{R}_v(m)$, and an initial value of the transmitted waveforms $\mathbf{f}$, the transceiver pair $(\mathbf{f}, \mathbf{h})$ can be optimized by repeating the following steps:

1. Compute $\mathbf{R}_{c,f} = E[\mathbf{C}\mathbf{f}\mathbf{f}^\dagger\mathbf{C}^\dagger], \mathbf{R}_{t,f} = E[\mathbf{T}\mathbf{f}\mathbf{f}^\dagger\mathbf{T}^\dagger]$
2. Compute the Cholesky decomposition

   $\mathbf{R}_{c,f} + \mathbf{R}_v = \mathbf{L}_{c,f}\mathbf{L}_{c,f}^\dagger$
3. $\mathbf{h} \leftarrow \mathbf{L}_{c,f}^{-\dagger}\mathbf{p}(\mathbf{L}_{c,f}^{-1}\mathbf{R}_{t,f}\mathbf{L}_{c,f}^{-\dagger})$
4. Compute $\mathbf{R}_{c,h} = E[\mathbf{C}^\dagger\mathbf{h}\mathbf{h}^\dagger\mathbf{C}], \mathbf{R}_{t,h} = E[\mathbf{T}^\dagger\mathbf{h}\mathbf{h}^\dagger\mathbf{T}]$
5. Compute the Cholesky decomposition

   $\mathbf{R}_{c,h} + \mathbf{h}^\dagger\mathbf{R}_v\mathbf{h} \cdot \mathbf{I} = \mathbf{L}_{c,f}\mathbf{L}_{c,f}^\dagger$
6. $\mathbf{f} \leftarrow \mathbf{L}_{c,f}^{-\dagger}\mathbf{p}(\mathbf{L}_{c,f}^{-1}\mathbf{R}_{t,h}\mathbf{L}_{c,f}^{-\dagger})$
7. $\mathbf{f} = \mathbf{f}/\|\mathbf{f}\|$

We stop when the SINR improvement becomes insignificant.

We have extended the proposed iterative method to the random target impulse response case. Note that it is not clear how to extend the method proposed in [82] to this case. The method proposed in [82] requires substituting the solution of $\mathbf{h}$ in (5.8) back into the objective function and obtain the optimization problem with only $\mathbf{f}$ parameter as in (5.9). In the random target impulse

response case, substituting the solution $\mathbf{h}$ in (5.14) back, the objective function becomes

$$\lambda_1(\mathbf{L}_{c,f}^{-1}\mathbf{R}_{t,f}\mathbf{L}_{c,f}^{-\dagger}), \tag{5.15}$$

where $\lambda_1(\mathbf{A})$ denotes the maximum eigenvalue of matrix $\mathbf{A}$. The iterative method proposed in [82] treats the matrix $\mathbf{R}_{c,f}$ in (5.9) as a constant with respect to $\mathbf{f}$ in every iteration and obtains the transmitted waveforms $\mathbf{f}$ by Rayleigh principle [48]. However, in the case of random target impulse response, even if we treat the matrix $\mathbf{L}_{c,f}^{-1}$ as a constant with respect to $\mathbf{f}$, it does not appear to be a simple matter to choose $\mathbf{f}$ to maximize the objective function in (5.15). For similar reason, it does not appear to be a simple matter to compute the matched filter bound which we have obtained for the deterministic target case.

5.4.2 Uncertain Target Impulse Response

We now consider the second case where the target impulse response is deterministic but unknown. We assume the target matrix $\mathbf{T}$ lies in a known convex set $\mathcal{S}$. Our goal is to maximize the worst SINR in this set. The worst SINR can be expressed as

$$\rho(\mathbf{f},\mathbf{h}) = \min_{\mathbf{T}\in\mathcal{S}} \frac{|\mathbf{h}^\dagger\mathbf{T}\mathbf{f}|^2}{E[|\mathbf{h}^\dagger\mathbf{C}\mathbf{f}|^2] + E[|\mathbf{h}^\dagger\mathbf{v}|^2]}. \tag{5.16}$$

So the goal is to solve the following optimization problem:

$$\max_{\mathbf{f},\mathbf{h}} \rho(\mathbf{f},\mathbf{h}) \text{ subject to } \|\mathbf{f}\|^2 \le 1. \tag{5.17}$$

To solve this problem, we first recast the problem using the following proposition.

Proposition 2. Define

$$\eta(\mathbf{f},\mathbf{h}) \triangleq \min_{\mathbf{T}\in\mathcal{S}} \frac{|\mathbf{h}^\dagger\mathbf{T}\mathbf{f}|^2}{E[|\mathbf{h}^\dagger\mathbf{C}\mathbf{f}|^2] + E[|\mathbf{h}^\dagger\mathbf{v}|^2]\cdot\mathbf{f}^\dagger\mathbf{f}}. \tag{5.18}$$

If $(\mathbf{f}_\star,\mathbf{h}_\star)$ solves the problem

$$\max_{\mathbf{f},\mathbf{h}} \eta(\mathbf{f},\mathbf{h}), \tag{5.19}$$

then $(\mathbf{f}_{\star\star},\mathbf{h}_\star)$ solves (5.17), where $\mathbf{f}_{\star\star} \triangleq \mathbf{f}_\star/\|\mathbf{f}_\star\|$.

Proof: For any $(\mathbf{f}, \mathbf{h}) \in \mathbb{C}^{N_T(L_T+1)} \times \mathbb{C}^{N_R(L_R+1)}$ satisfying $\|\mathbf{f}\|^2 \leq 1$, we have $\rho(\mathbf{f}_{\star\star}, \mathbf{h}) = \eta(\mathbf{f}_\star, \mathbf{h}) \geq \eta(\mathbf{f}, \mathbf{h}) \geq \rho(\mathbf{f}, \mathbf{h})$. Also, $\|\mathbf{f}_{\star\star}\|^2 \leq 1$. Therefore $(\mathbf{f}_{\star\star}, \mathbf{h}_\star)$ solves (5.17). ■

One can see that the logical flow of this proof is identical to Proposition 1. This proposition allows us to get rid of the power constraint in (5.17) and solve the unconstrained problem in (5.19) instead. To solve the max-min problem, one can first solve for the worst target matrix $\mathbf{T}$ in the minimization problem in (5.18). Since the feasible set $\mathcal{S}$ is convex and the objective function is quadratic with respect to $\mathbf{T}$, the optimization problem in (5.18) is a convex problem. It can be solved numerically if the values of $\mathbf{f}$ and $\mathbf{h}$ are given. However, the values of $\mathbf{f}$ and $\mathbf{h}$ have not yet been given at this moment. They are parameters which will be maximized in (5.19). So, in order to solve the problem in this manner, we need to solve $\mathbf{T}$ in terms of $\mathbf{f}$ and $\mathbf{h}$ analytically. Then the objective function $\eta(\mathbf{f}, \mathbf{h})$ in (5.18) can be expressed analytically in terms of $\mathbf{f}$ and $\mathbf{h}$. However, in general, the analytic solution may not be available. Even if we can obtain the analytic form of $\mathbf{T}$, the resulting function $\eta(\mathbf{f}, \mathbf{h})$ might not be concave in terms of parameter $\mathbf{f}$ or $\mathbf{h}$. If $\eta(\mathbf{f}, \mathbf{h})$ is not concave in terms of $\mathbf{f}$ or $\mathbf{h}$, the problem in (5.19) is in general not easy to solve.

To overcome this difficulty, we apply the following proposition.

Proposition 3. If $(\mathbf{x}_\star, \mathbf{T}_\star)$ solves

$$\min_{\mathbf{T}\in\mathcal{S}} \max_{\mathbf{x}} \frac{|\mathbf{y}^\dagger \mathbf{T}\mathbf{x}|^2}{\mathbf{x}^\dagger \mathbf{R}\mathbf{x}}$$

for some $\mathbf{y}$ and $\mathbf{R}$, then it also solves

$$\max_{\mathbf{x}} \min_{\mathbf{T}\in\mathcal{S}} \frac{|\mathbf{y}^\dagger \mathbf{T}\mathbf{x}|^2}{\mathbf{x}^\dagger \mathbf{R}\mathbf{x}}.$$

Proof: Applying Proposition 1 in [53], one can verify that $(\mathbf{x}_\star, \mathbf{T}_\star)$ is a saddle point, that is,

$$\frac{|\mathbf{y}^\dagger \mathbf{T}_\star \mathbf{x}|^2}{\mathbf{x}^\dagger \mathbf{R}\mathbf{x}} \leq \frac{|\mathbf{y}^\dagger \mathbf{T}_\star \mathbf{x}_\star|^2}{\mathbf{x}_\star^\dagger \mathbf{R}\mathbf{x}_\star} \leq \frac{|\mathbf{y}^\dagger \mathbf{T}\mathbf{x}_\star|^2}{\mathbf{x}_\star^\dagger \mathbf{R}\mathbf{x}_\star}, \ \forall \mathbf{x} \neq 0, \ \mathbf{T} \in \mathcal{S}.$$

By using the minimax theorem [106], the saddle point also solves the second optimization problem. ■

This proposition allows us to change the order of the maximization with respect $\mathbf{f}$ and $\mathbf{h}$ and the minimization with respect to $\mathbf{T}$ in (5.18) and (5.19).

To solve the optimization problem in (5.19), we use the iterative approach as before. In each step, we optimize $\mathbf{f}$ with fixed $\mathbf{h}$ or optimize $\mathbf{h}$ with fixed $\mathbf{f}$. We first demonstrate how to solve $\mathbf{f}$ with fixed $\mathbf{h}$, that is, to solve

$$\max_{\mathbf{f}} \min_{\mathbf{T}\in\mathcal{S}} \frac{|\mathbf{h}^\dagger \mathbf{T}\mathbf{f}|^2}{\mathbf{f}^\dagger \mathbf{R}_{c,h}\mathbf{f} + \mathbf{h}^\dagger \mathbf{R}_v \mathbf{h}\cdot \mathbf{f}^\dagger \mathbf{f}}, \text{ for fixed } \mathbf{h}.$$

Applying Proposition 3, the above problem can be recast as

$$\min_{\mathbf{T}\in S} \max_{\mathbf{f}} \frac{|\mathbf{h}^\dagger \mathbf{T}\mathbf{f}|^2}{\mathbf{f}^\dagger (\mathbf{R}_{c,h} + \mathbf{h}^\dagger \mathbf{R}_v \mathbf{h}\cdot \mathbf{I})\mathbf{f}}.$$

Using the same MVDR approach for obtaining (5.12), one can obtain

$$\mathbf{f} = \alpha(\mathbf{R}_{c,h} + \mathbf{h}^\dagger \mathbf{R}_v \mathbf{h}\cdot \mathbf{I})^{-1}\mathbf{T}^\dagger \mathbf{h},$$

where α is a scalar which will be determined by the power constraint. Substituting $\mathbf{f}$ into the objective function, the optimization problem becomes

$$\min_{\mathbf{T}\in\mathcal{S}} \mathbf{h}^\dagger \mathbf{T}(\mathbf{R}_{c,h} + \mathbf{h}^\dagger \mathbf{R}_v \mathbf{h}\cdot \mathbf{I})^{-1}\mathbf{T}^\dagger \mathbf{h}.$$

Observing the above problem, one can see that the cost function is a convex function and the feasible set $\mathcal{S}$ is a convex set. Therefore it is a convex optimization problem. Note that since $\mathbf{h}$ is fixed now, the solution $\mathbf{T}$ can be solved numerically. This $\mathbf{T}$ yields the worst case target in the uncertainty set.

With similar technique, one can also solve $\mathbf{h}$ with fixed $\mathbf{f}$, and obtain the following solution:

$$\mathbf{h} = \alpha(\mathbf{R}_{c,f} + \mathbf{R}_v)^{-1}\mathbf{T}\mathbf{f},$$

where α is a scalar which will be determined by the power constraint, and $\mathbf{T}$ is the solution to the following convex optimization problem

$$\min_{\mathbf{T}\in\mathcal{S}} \mathbf{f}^\dagger \mathbf{T}^\dagger (\mathbf{R}_{c,f} + \mathbf{R}_v)^{-1}\mathbf{T}\mathbf{f},$$

which can be solved numerically.

With these methods, we can increase the worst SINR defined in (5.16) in each step by optimizing

$\mathbf{f}$ or $\mathbf{h}$ one at a time. We summarize the algorithm as the following.

Algorithm 3. Given the target matrix uncertainty set $\mathcal{S}$, the clutter covariance $\mathbf{R}_c(m)$, noise covariance $\mathbf{R}_v(m)$, and an initial value of the transmitted waveforms $\mathbf{f}$, the transceiver pair $(\mathbf{f}, \mathbf{h})$ can be optimized by the following steps.

1. Compute $\mathbf{R}_{c,f} = E[\mathbf{C}\mathbf{f}\mathbf{f}^\dagger\mathbf{C}^\dagger]$
2. $\mathbf{T}_\star \leftarrow \arg\min_{\mathbf{T}\in\mathcal{S}} \mathbf{f}^\dagger\mathbf{T}^\dagger(\mathbf{R}_{c,f} + \mathbf{R}_v)^{-1}\mathbf{T}\mathbf{f}$
3. $\mathbf{h} \leftarrow (\mathbf{R}_{c,f} + \mathbf{R}_v)^{-1}\mathbf{T}_\star\mathbf{f}$
4. Compute $\mathbf{R}_{c,h} = E[\mathbf{C}^\dagger\mathbf{h}\mathbf{h}^\dagger\mathbf{C}]$
5. $\mathbf{T}_\star \leftarrow \arg\min_{\mathbf{T}\in\mathcal{S}} \mathbf{h}^\dagger\mathbf{T}(\mathbf{R}_{c,h} + \mathbf{h}^\dagger\mathbf{R}_v\mathbf{h}\cdot\mathbf{I})^{-1}\mathbf{T}^\dagger\mathbf{h}$
6. $\mathbf{f} \leftarrow (\mathbf{R}_{c,h} + \mathbf{h}^\dagger\mathbf{R}_v\mathbf{h}\cdot\mathbf{I})^{-1}\mathbf{T}_\star^\dagger\mathbf{h}$
7. $\mathbf{f} \leftarrow \mathbf{f}/\|\mathbf{f}\|$.

We stop when the SINR improvement becomes insignificant.

Special Case: Sphere Uncertainty Set.

Now we consider a sphere uncertainty set, that is,

$$\mathcal{S} = \{\mathbf{T} \mid \|\mathbf{T} - \mathbf{T}_0\|_F^2 \le r^2\}, \tag{5.20}$$

where $\mathbf{T}_0$ is the origin and r is the radius of the sphere. Note that this is a special case of the convex uncertainty set. We assume r is small enough so that $\mathbf{0} \notin \mathcal{S}$. This is a reasonable assumption because if $\mathbf{0} \in \mathcal{S}$, no matter how we choose $\mathbf{f}$ and $\mathbf{h}$, the worst SINR in (5.16) will always be zero. In this case, one can use the Lagrange multiplier method to solve for the worst SINR in (5.16) and obtain

$$\eta(\mathbf{f}, \mathbf{h}) = \frac{|\mathbf{h}^\dagger\mathbf{T}_0\mathbf{f} - r\|\mathbf{h}\|\|\mathbf{f}\|e^{j\angle(\mathbf{h}^\dagger\mathbf{T}_0\mathbf{f})}|^2}{E[|\mathbf{h}^\dagger\mathbf{C}\mathbf{f}|^2] + \mathbf{h}^\dagger\mathbf{R}_v\mathbf{h}}. \tag{5.21}$$

The derivation of the above worst SINR expression is shown in the Appendix in the end of this chapter. Although an analytic solution for the worst SINR can be obtained, one can see that $\eta(\mathbf{f}, \mathbf{h})$ is not convex in either $\mathbf{f}$ or $\mathbf{h}$. So it is difficult to maximize the worst SINR from the above expression.

We can apply Algorithm 3 to solve this problem. In this case, the convex optimization in Step 2

of Algorithm 3 becomes

$$\min_{\|\mathbf{T}-\mathbf{T}_0\|_F^2 \leq r^2} \mathbf{f}^\dagger \mathbf{T}^\dagger (\mathbf{R}_{c,f} + \mathbf{R}_v)^{-1} \mathbf{T}\mathbf{f}. \tag{5.22}$$

As we have mentioned earlier, this is a convex optimization problem and therefore can be solved numerically. However, we will show that in this special case of the sphere uncertainty set, a simple line search algorithm can be used to solve this problem. Define the Lagrangian as

$$\begin{aligned} L(\mathbf{T}, \lambda) \quad &\triangleq \quad \mathbf{f}^\dagger \mathbf{T}^\dagger (\mathbf{R}_{c,f} + \mathbf{R}_v)^{-1} \mathbf{T}\mathbf{f} + \\ &\qquad \lambda(\text{tr}((\mathbf{T} - \mathbf{T}_0)(\mathbf{T} - \mathbf{T}_0)^\dagger) - r^2), \end{aligned}$$

where $\lambda \geq 0$ is the Lagrange multiplier. Differentiating the above function with respect to $\mathbf{T}$ and setting it to zero, we obtain

$$(\mathbf{R}_{c,f} + \mathbf{R}_v)^{-1} \mathbf{T}\mathbf{f}\mathbf{f}^\dagger + \lambda(\mathbf{T} - \mathbf{T}_0) = \mathbf{0}. \tag{5.23}$$

From the above equation, one can observe that $\mathbf{T} - \mathbf{T}_0$ has rank one. Without loss of generality, there exists some $\mathbf{u} \in \mathbb{C}^{N_R(L_R+1)\times 1}$ such that

$$\mathbf{T} - \mathbf{T}_0 = \mathbf{u}\mathbf{f}^\dagger.$$

Substituting $\mathbf{T} = \mathbf{T}_0 + \mathbf{u}\mathbf{f}^\dagger$ into (5.23) and solving for $\mathbf{u}$, one can obtain

$$\mathbf{T} = \mathbf{T}_0 - (\lambda(\mathbf{R}_{c,f} + \mathbf{R}_v) + \|f\|^2 \mathbf{I})^{-1} \mathbf{T}_0 \mathbf{f}\mathbf{f}^\dagger.$$

We have almost finished solving for $\mathbf{T}$ except that there is still an unknown Lagrange multiplier λ in the above equation. Note that usually the constraint in (5.22) can be either an active constraint

$$\|\mathbf{T} - \mathbf{T}_0\|_F^2 = r^2 \tag{5.24}$$

or an inactive constraint $\|\mathbf{T} - \mathbf{T}_0\|_F^2 < r^2$. The inactive constraint only happens when the cost function reaches global minimum, that is, $\mathbf{T} = \mathbf{0}$. But $\mathbf{T} = \mathbf{0}$ cannot happen because we have assumed $\mathbf{0} \notin \mathcal{S}$. Consequently, the constraint will always be active as in (5.24). Thus the Lagrange

multiplier λ can be obtained by solving (5.24). Define the eigenvalue decomposition

$$\mathbf{R}_{c,f} + \mathbf{R}_v = \mathbf{Q}\mathbf{D}\mathbf{Q}^\dagger,$$

where $\mathbf{Q}$ is unitary and $\mathbf{D}$ is diagonal. Eq. (5.24) can thus be expressed as

$$\begin{aligned} & \|\mathbf{T} - \mathbf{T}_0\|_F^2 \\ = \; & \|(\lambda(\mathbf{R}_{c,f} + \mathbf{R}_v) + \|\mathbf{f}\|^2\mathbf{I})^{-1}\mathbf{T}_0\mathbf{f}\mathbf{f}^\dagger\|_F^2 \\ = \; & \|\mathbf{f}\|^2 \cdot \|(\lambda\mathbf{D} + \|\mathbf{f}\|^2\mathbf{I})^{-1}\mathbf{Q}^\dagger\mathbf{T}_0\mathbf{f}\|^2 \\ = \; & \|\mathbf{f}\|^2 \cdot \sum_{i=0}^{N_R(L_R+1)-1} \frac{|(\mathbf{Q}^\dagger\mathbf{T}_0\mathbf{f})_i|^2}{(\lambda \cdot (\mathbf{D})_{i,i} + \|\mathbf{f}\|^2)^2} = r^2. \end{aligned}$$

Note that $(\mathbf{D})_i \geq 0$ because $\mathbf{R}_{c,f} + \mathbf{R}_v$ is positive semidefinite. Also, we have the Lagrange multiplier $\lambda \geq 0$. Therefore, the left side of the last equality is a decreasing function of λ. This implies the solution for λ is unique. In this case, the solution for λ can be easily found by some simple line search algorithm such as Newton's method [9].

Using the same argument, one can solve the convex optimization problem in Step 5 of Algorithm 3 and obtain the following solution

$$\mathbf{T} = \mathbf{T}_0 - \mathbf{h}\mathbf{h}^\dagger\mathbf{T}_0(\lambda(\mathbf{R}_{c,h} + \mathbf{h}^\dagger\mathbf{R}_v\mathbf{h} \cdot \mathbf{I}) + \|\mathbf{h}\|^2\mathbf{I})^{-1},$$

where λ is the Lagrange multiplier. It can be solved by a line search algorithm using the following relation

$$\|\mathbf{h}\|^2 \cdot \sum_{i=0}^{N_T(L_T+1)-1} \frac{|(\mathbf{Q}\mathbf{T}_0^\dagger\mathbf{h})_i|^2}{(\lambda \cdot (\mathbf{D})_{i,i} + \|\mathbf{h}\|^2)^2} = r^2,$$

where $\mathbf{Q}\mathbf{D}\mathbf{Q}^\dagger$ is the eigenvalue decomposition of the matrix $(\mathbf{R}_{c,h} + \mathbf{h}^\dagger\mathbf{R}_v\mathbf{h} \cdot \mathbf{I})$.

Therefore, in the sphere uncertainty set case, the numerical convex optimization in Step 2 and Step 5 of Algorithm 3 can be replaced by the above-mentioned method which can be much more efficient. In [73], similar result has been obtained for solving beamformer robust against steering vector mismatch. The second order cone programming has been replaced by the line search algorithm in [73], by using the Lagrange multiplier method.

5.5 Numerical Examples

In this section, the SINR performances of the proposed method are compared to the method in [82] which has been extended to the MIMO case in [36], and to the orthogonal LFM (linear frequency modulation) waveforms. The orthogonal LFM waveforms is defined as

$$(\mathbf{f})_l = \frac{e^{j\pi \frac{1}{2(L_T+1)}(l \mod N_T)^2} \cdot e^{j2\pi \lfloor \frac{l}{N_T} \rfloor (l \mod N_T)}}{\sqrt{N_T(L_T+1)}}.$$

Note that LFM waveforms are designed for a different purpose, namely, obtaining a sharp ambiguity function. They are good candidates for distinguish point targets, and in imaging. However, the LFM waveforms may not have good SINR performances in the extended target case.

Example 5.1: SINR versus number of iterations

Consider a MIMO radar system with number of transmitting antennas $N_T = 4$ and number of receiving antennas $N_R = 4$. The target impulse response is given by

$$(\mathbf{t}(n))_{k,l} = \begin{cases} 1, & n = 0, 1, \cdots, 20 \\ 0, & \text{otherwise} \end{cases}.$$

The clutter impulse response is modelled as an AR (auto-regressive) process with covariance

$$\mathbf{R}_c(n) = \mathbf{B}\mathbf{A}^{|n|}\mathbf{B}^\dagger,$$

where the parameters $\mathbf{A}$ and $\mathbf{B}$ are 16×16 real matrices shown in Fig. 5.3. Here $\mathbf{A}$ is a positive semidefinite matrix with spectral radius less than unity. The noise $\mathbf{v}(n)$ is modelled as white noise with unity variance. Fig. 5.4 shows the SINR performances defined in (5.5) as a function of the number of iterations. The matched filter bound which has been derived in the end of Sec. 5.3 is also shown in the figure. The matched filter SINR, which takes the clutter signal into account is also shown in the figure. The Note that LFM waveform is fixed, so its SINR is not a function of the number of iterations. The initial waveforms used in Algorithm 1 (the new algorithm proposed in Sec. 3) and in the method in [36, 82] are identical. One can observe that Algorithm 1 has a better performance than other methods. Algorithm 1 also converges very fast. It converges in about six iterations in this example. Moreover, in Algorithm 1, the SINR is a nondecreasing function of the number of iterations. The initial transmitted waveforms are shown in Fig. 5.5 (a)–(d). Note that the

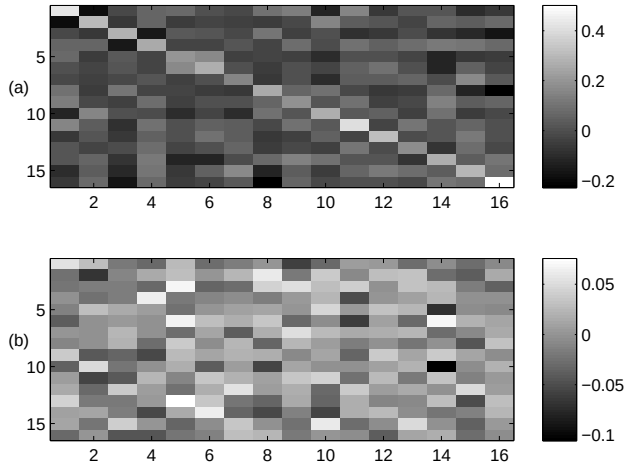

Figure 5.3: Example 5.1: The parameters used in the matrix AR model (a) matrix **A** and (b) matrix **B**

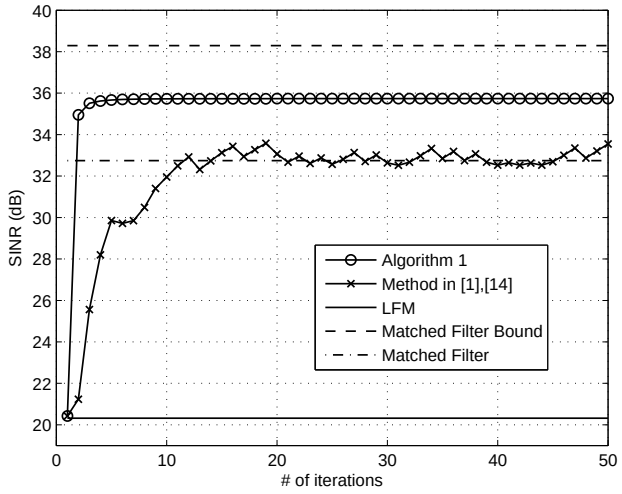

Figure 5.4: Example 5.1: Comparison of the SINR versus number of iterations

vector $\mathbf{f}$ contains four waveforms as defined in Eq. (5.3). The optimized transmitted waveforms and receiving filters are shown in Fig. 5.5 (e)–(l).

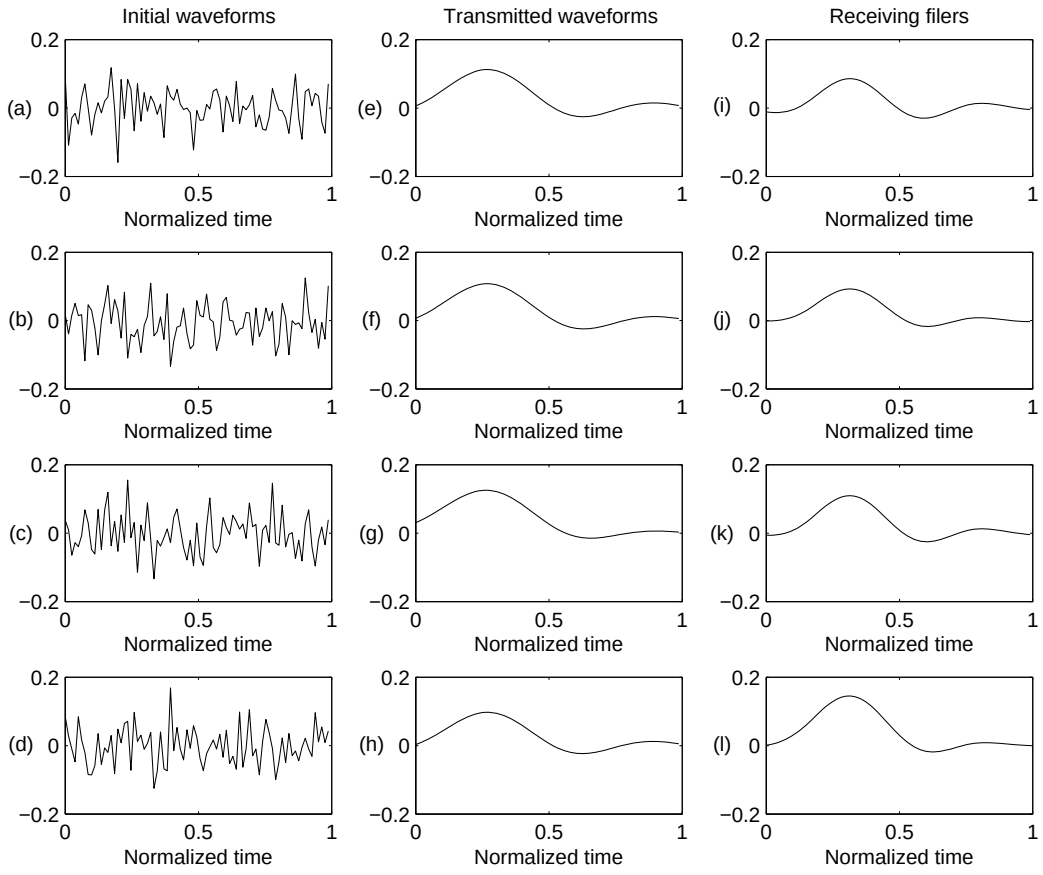

Figure 5.5: Example 5.1: (a)–(d) real part of the initial transmitted waveforms, (e)–(h) real part of the transmitted four waveforms $\mathbf{f}$ obtained by Algorithm 1, (i)–(l) real part of the four receiving filters $\mathbf{h}$ obtained by Algorithm 1

Example 5.2: SINR versus CNR

In this example, the SINR performances are compared for different values of CNR (clutter-to-noise ratio). Consider a MIMO radar with number of transmitting antennas $N_T = 2$ and number of receiving antennas $N_R = 2$. The order of the target impulse response $\mathbf{T}(z)$ is 20. The coefficients $\{(\mathbf{t}(n))_{k,l}\}$ are generated as i.i.d. (independent and identically distributed) circular complex Gaus-

sian random variables with unity variance. The covariance of the clutter impulse response $\mathbf{R}_c(n)$ is generated by using

$$\mathbf{R}_c(n) = \mathbf{U}_c(n) * \mathbf{U}_c(-n)^\dagger,$$

where the notation $*$ denotes convolution, $\mathbf{U}_c(n)$ is a 4×4 matrix sequence with length 31 and the coefficients $\{(\mathbf{U}(n))_{k,l}\}$ are i.i.d. circular complex Gaussian random variables. The noise $\mathbf{v}(n)$ is a white process with unity variance. The initial waveforms used in the algorithms are randomly chosen. The simulation is performed by averaging among 1000 different target, clutter and noise realizations. Fig. 5.6 shows the comparison of the SINR defined in (5.5) under different CNR. The

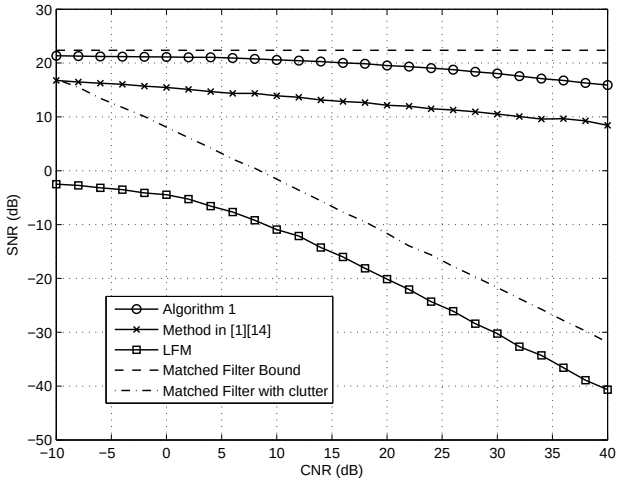

Figure 5.6: Example 5.2: Comparison of the SINR versus CNR

matched filter bound which has been derived in the end of Sec. 5.3 is also shown on the figure. The matched filter SINR, which takes the clutter signal into account is also shown in the figure. One can see that Algorithm 1 has the best SINR performances among all the methods under all CNR. Both Algorithm 1 and method in [36,82] have much better performances than the LFM waveforms. This shows that utilizing the prior information in the transmitter is very crucial for the SINR performance.

Example 5.3: SINR versus CNR with random target impulse response

In this example, the SINR performances are compared under different CNR as in the last example.

However, the coefficients of the target impulse response vec($\mathbf{t}(n)$) are modelled as a WSS random process with covariance $\mathbf{R}_t(n)$. The covariance $\mathbf{R}_t(n)$ is generated by using

$$\mathbf{R}_t(n) = \mathbf{U}_t(n) * \mathbf{U}_t(-n)^\dagger,$$

where $\mathbf{U}_t(n)$ is a 4×4 matrix sequence with length 21 and the coefficients $\{(\mathbf{U}_t(n))_{k,l}\}$ are i.i.d. circular complex Gaussian random variables. Except the target impulse response, all the parameters used in this example are identical to Example 5.2. The simulation is performed by averaging among 1000 different target, clutter, and noise realizations. Fig. 5.7 shows the comparison of the SINR defined in (5.5) under various CNR. We have explained in Sec. 4.1 that it is not clear how to

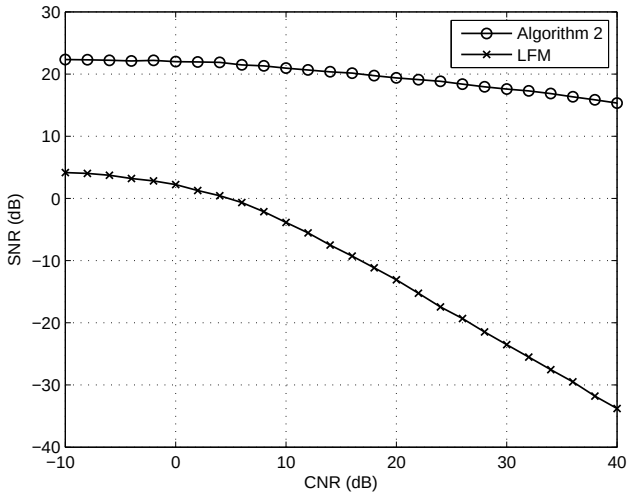

Figure 5.7: Example 5.3: Comparison of the SINR versus CNR with random target impulse response

generalize the method in [36, 82] and the matched filter bound to this case. Thus we only compare Algorithm 2 and LFM waveforms in this case. One can see that Algorithm 2 has a significantly better SINR performances than the LFM waveforms.

Example 5.4: Worst SINR versus CNR with uncertain target impulse response

In this example, we consider that the target matrix $\mathbf{T}$ is in a sphere uncertainty set as shown in (5.20). The worst SINR in (5.21) are compared under various CNR. All the parameters are identical to the last example, except the target impulse response. The center $\mathbf{T}_0$ of the sphere is a block

Toeplitz matrix generated by the matrix sequence $\mathbf{t}_0(n)$ as in (5.4). The order of $\mathbf{t}_0(n)$ is 20. The elements of $\mathbf{t}_0(n)$, namely $\{(\mathbf{t}_0(n))_{k,l}\}$, are generated as i.i.d. circular complex Gaussian random variables with unity variance. The radius r is chosen to be 5% of $\|\mathbf{T}\|_F$. The simulation is performed by averaging among 1000 different target center $\mathbf{T}_0$, clutter, and noise realizations. In this example, the following four different SINR results are compared:

1. *Algorithm 1 without mismatch:* The transceiver pair $(\mathbf{f}, \mathbf{h})$ is obtained by using Algorithm 1 with the target matrix $\mathbf{T} = \mathbf{T}_0$. The SINR is obtained by using (5.5) with $\mathbf{T} = \mathbf{T}_0$ as well.

2. *Algorithm 3:* The transceiver is obtained by using Algorithm 3 with the origin $\mathbf{T}_0$ and radius r. The SINR is the worst SINR obtained by using (5.16).

3. *Algorithm 1:* The transceiver is obtained by using Algorithm 1 with the target matrix $\mathbf{T}_0$. The SINR is the worst SINR obtained by using (5.16).

4. *Method in [36, 82]:* The transceiver is obtained by using the method in [36, 82] with the target matrix $\mathbf{T}_0$. The SINR is the worst SINR obtained by using (5.16).

Fig. 5.8 shows the SINR performances under different CNR. As expected, Algorithm 1 without

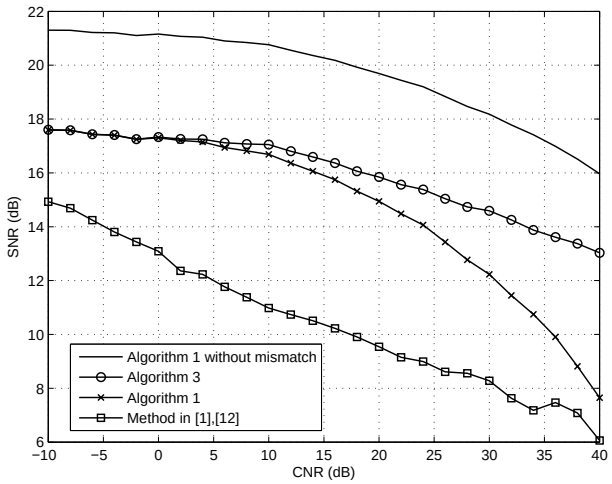

Figure 5.8: Example 5.4: Comparison of the worst SINR versus CNR with uncertain target impulse response

the target mismatch has the best SINR performance. Algorithm 3 which is designed for robustness

against target mismatch has a significantly better worst SINR performance compared to Algorithm 1 in the high CNR region.

5.6 Conclusions

In this chapter, we have proposed an iterative algorithm for jointly designing the transmitted waveforms and the receiving filters to maximize the SINR in MIMO radar with the prior information of the extended target and clutter. This iterative algorithm alternatively solves the optimal transmitted waveforms and the receiving filters by fixing the other parameters. This algorithm finds a local maximum which is also a global maximum along the dimension of the transmitted waveforms and the dimension of the receiving filter separately. The proposed iterative algorithm has also been extended to the case of random target impulse response and the case of uncertain target impulse response. The numerical results show that the proposed iterative algorithm converges faster and also has better SINR performances than previously reported algorithms. Some of the important design issues such as constant modulus and range resolution are not considered in this chapter. From a practical stand-point, it is important that the radar transmitter has a low PAR (peak-to-average-power ratio). Also, the optimal waveforms obtained by the proposed method may not have good performance for range estimation. The waveform design problem which takes into account these important issues will be explored in the future.

5.7 Appendix

In this appendix, we derive the worst SINR in the case of sphere uncertainty target impulse response as shown in (5.21). For simplicity, we ignore the irrelevant denominator in (5.16). The following optimization problem is considered

$$\begin{aligned} &\min_{\mathbf{T}} |\mathbf{h}^\dagger \mathbf{T}\mathbf{f}|^2 \\ &\text{subject to } \|\mathbf{T}-\mathbf{T}_0\|_F^2 \le r^2. \end{aligned} \tag{5.25}$$

The Lagrangian of the above problem can be defined as

$$L(\mathbf{T},\lambda) \triangleq |\mathbf{h}^\dagger \mathbf{T}\mathbf{f}|^2 + \lambda(\text{tr}((\mathbf{T}-\mathbf{T}_0)(\mathbf{T}-\mathbf{T}_0)^\dagger) - r^2),$$

where $\lambda \geq 0$ is the Lagrange multiplier. Differentiating the Lagrangian with respect to $\mathbf{T}$ and setting it to zero, we obtain

$$(\mathbf{h}^\dagger \mathbf{T} \mathbf{f}) \cdot \mathbf{h}\mathbf{f}^\dagger + \lambda(\mathbf{T} - \mathbf{T}_0) = \mathbf{0}.$$

From the above equality, without loss of generality, there exists a scalar α such that

$$\mathbf{T} - \mathbf{T}_0 = \alpha \mathbf{h}\mathbf{f}^\dagger. \tag{5.26}$$

Note that usually the constraint in (5.25) can be either an active constraint

$$\|\mathbf{T} - \mathbf{T}_0\|_F^2 = r^2 \tag{5.27}$$

or an inactive constraint $\|\mathbf{T} - \mathbf{T}_0\|_F^2 < r^2$. The inactive constraint only happens when the cost function reaches global minimum, that is, $\mathbf{T} = \mathbf{0}$. But $\mathbf{T} = \mathbf{0}$ cannot happen because we have assumed $\mathbf{0} \notin \mathcal{S}$. Consequently, the constraint will always be active as in (5.27). By substituting (5.26) into (5.27), one can obtain the magnitude of α as

$$|\alpha| = \frac{r}{\|\mathbf{h}\|\|\mathbf{f}\|}.$$

Substituting this result back into (5.26), we obtain

$$\mathbf{T} = \mathbf{T}_0 - \frac{r\mathbf{h}\mathbf{f}^\dagger}{\|\mathbf{f}\|\|\mathbf{h}\|} e^{j\measuredangle\alpha}.$$

Now the only unknown in the above equation is the phase $\measuredangle\alpha$. To solve for the unknown phase, substituting the above expression into the cost function, one can obtain

$$|\mathbf{h}^\dagger \mathbf{T} \mathbf{f}|^2 = \left|\mathbf{h}^\dagger \mathbf{T}_0 \mathbf{f} - r\|\mathbf{h}\|\|\mathbf{f}\| e^{j\measuredangle\alpha}\right|^2.$$

One can easily verify that the phase which minimizes the above cost function is $\measuredangle\alpha = \measuredangle \mathbf{h}^\dagger \mathbf{T}_0 \mathbf{f}$. Therefore the solution to the problem in (5.27) is

$$\mathbf{T} = \mathbf{T}_0 - \frac{r\mathbf{h}\mathbf{f}^\dagger}{\|\mathbf{f}\|\|\mathbf{h}\|} e^{j\measuredangle(\mathbf{h}^\dagger \mathbf{T}_0 \mathbf{f})}.$$

Substituting the above solution back into the cost function, one can obtain the minimum as

$$|\mathbf{h}^{\dagger}\mathbf{T}\mathbf{f}|^2 = |\mathbf{h}^{\dagger}\mathbf{T}_0\mathbf{f} - r\|\mathbf{h}\|\|\mathbf{f}\|e^{j\angle(\mathbf{h}^{\dagger}\mathbf{T}_0\mathbf{f})}|^2.$$

Chapter 6

Conclusion

In this thesis, we have presented a wide variety of signal processing algorithms for MIMO radar. In Chapter 2, we focused on the design of the beamformer. We proposed a new beamformer robust against DOA mismatch. The MVDR beamformer is known to be very sensitive to the DOA mismatch. This approach quadratically constrains the magnitude responses of two steering vectors and then uses a diagonal loading method to force the magnitude response at a desired range of angles to exceed unity. Therefore this method can always force the magnitude responses at a desire range of angles to exceed a constant level while suppressing the interferences and noise. The analytic solution to the non-convex quadratically constrained minimization problem has been given and the diagonal loading factor can be determined by a simple iteration method. The complexity required is approximately the same as in the MVDR beamformer. The numerical examples demonstrate that our approach has an excellent SINR performance under a wide range of conditions.

In Chapter 3, we focused on the space-time adaptive processing in MIMO radar. We first studied the clutter subspace and its rank in MIMO radar using the geometry of the system. The extension of Brennan's rule for estimating the dimension of the clutter subspace in the MIMO radar was derived. An algorithm for computing the clutter subspace using nonuniform sampled prolate-spheroidal wave function was proposed. We also proposed a space-time adaptive processing algorithm in MIMO radar. This algorithm utilizes the knowledge of the geometry of the problem, and the structure of the jammer covariance matrix. Using the fact that the jammer matrix is block diagonal and the clutter matrix has low rank with known subspace, we showed how to break the inversion of a large covariance matrix into the inversions of several smaller matrices. Thus the new method has much lower computational complexity. Moreover, we can directly null out the entire clutter space for the strong clutter case. We have provided several numerical examples which show

that for a given number of data samples, the new method has much better performance.

In Chapter 4, we studied the ambiguity function of the MIMO radar and the corresponding waveform optimization problem. We derived several useful properties of the MIMO radar ambiguity function and the cross ambiguity function. These properties characterize the energy, symmetry and LFM (linear frequency modulation) of the ambiguity function. The energy properties imply that we can only spread the energy of the MIMO radar ambiguity function evenly on the available time and bandwidth because the energy is confined. The symmetry properties imply that when we design the waveform, we only need to focus on half of the MIMO radar ambiguity function. The LFM properties show that the LFM waveforms creates shear-off effect which improves the range resolution of the ambiguity function. We have also introduced a waveform design method for MIMO radars. The proposed waveforms sharpen the ambiguity function and therefore they provide better system resolution. The proposed method applies the simulated annealing algorithm to search for the frequency-hopping codes which minimize the p-norm of the ambiguity function. The numerical examples show that the waveforms generated by this method provide better angular and range resolutions than the LFM waveforms which have often been used in the traditional SIMO radar systems.

In Chapter 5, we focused on the waveform design problem with information about the target and the clutter responses. We have proposed an iterative algorithm for jointly designing the transmitted waveforms and the receiving filters to maximize the SINR in MIMO radar. This iterative algorithm alternatively solves the optimal transmitted waveforms and the receiving filters by fixing the other parameters. The algorithm finds a local maximum which is also a global maximum along the dimension of the transmitted waveforms and the dimension of the receiving filter separately. We also extended the proposed algorithm to the case of random target impulse response and the case of uncertain target impulse response. The numerical results show that the proposed iterative algorithm converges faster and also has better SINR performances than previously reported algorithms.

6.1 Future Work

There are various topics worthy of future research. In Chapter 3, we have proposed a method which uses the geometry of the problem to improve the MIMO STAP. This method is very effective but may suffer from the model mismatch. A hybrid of the statistical and geometrical approaches

may increase the robustness against geometrical model mismatch and reduce the required samples for estimating the clutter subspace.

In the MIMO radar waveform design, we have considered the waveforms which optimize the SINR. These waveforms are optimal for detection. However, after detecting the target, we often need to estimate its position. In Chapter 4, we have studied the waveforms which provide good resolutions for point targets. To obtain better estimation of the target location, it is also important that the waveforms provide good range and angle resolutions for the extended target discussed in Chapter 5. This may be done by incorporating more constraints in the waveform optimization problem.

The concept of virtual array is the key for increasing the spatial resolution in MIMO radar. We have obtained the virtual array through the transmission of orthogonal waveforms and match filtering. However, transmitting orthogonal waveforms decreases the processing gain. There may exist some better approach to obtain the virtual array resolution without compromising the processing gain. This topic is also worthy of further investigation.

Bibliography

[1] Y. I. Abramovich, "Controlled method for adaptive optimization of filters using the criterion of maximum SNR,"*Radio Engineering and Electronic Physics,* vol. 26, pp. 87–95, March 1981.

[2] Y. I. Abramovich and G. J. Frazer, "Bounds on the Volume and Height Distributions for the MIMO Radar Ambiguity Function," *IEEE Signal Processing Letters,* Volume 15, pp. 505–508, May 2008.

[3] G. S. Antonio and D. R. Fuhrmann, "Beampattern Synthesis for Wideband MIMO Radar Systems," *Proc. 1st. IEEE International Workshop on Computational Advances in Multi-Sensor Adaptive Processing,* pp. 105–108, Dec. 2005.

[4] S. P. Applebaum and D. J. Chapman, "Adaptive arrays with main beam constraints," *IEEE Trans. Ant. Prop.,* vol. AP-24, pp. 650–662, Sept. 1976.

[5] M. R. Bell, "Information Theory and Radar Waveform Design," *IEEE Trans. on Information Theory,* Vol 39, Issue 5, pp. 1578–1597, Sept. 1993.

[6] K. L. Bell, Y. Ephraim, and H. L. Van Trees, "A Bayesian approach to robust adaptive beamforming," *IEEE Trans. Sig. Proc.,* vol. 48, pp. 386–398, Feb. 2000.

[7] D. W. Bliss and K. W. Forsythe, "Multiple-input multiple-output (MIMO) radar and imaging: degrees of freedom and resolution," *Proc. 37th IEEE Asilomar Conf. on Signals, Systems, and Computers,* vol. 1, pp. 54–59, Nov. 2003.

[8] A. H. Booker, C.Y. Ong, J.P. Burg, and G.D. Hair, *Multiple-constraint adaptive filtering.* Dallas, TX: Texas Instrum. Sci. Services Div., April 1969.

[9] S. Boyd and L. Vandenberghe, *Convex Optimization,* Cambridge University Press, 2004.

[10] L. E. Brennan and F. M. Staudaher, "Subclutter Visibility Demonstration," Technical Report RL-TR-92-21, Adaptive Sensors Inc., 1992.

[11] K. M. Buckley and L. J. Griffiths, "An adaptive generalized sidelobe canceler with derivative constraints," *IEEE Trans. Ant. Prop.,* vol. AP-34, pp. 311–319, Mar. 1986.

[12] J. Capon, "High-resolution frequency-wavenumber spectrum analysis," *Proc. IEEE,* vol. 57, no. 8, pp. 1408–1418, Aug. 1969.

[13] B. D. Carlson, "Covariance matrix estimation errors and diagonal loading in adaptive arrays," *IEEE Trans. Aerosp. Electron. Syst.,* vol. 24, pp. 397–401, July 1988.

[14] C. Y. Chen and P. P. Vaidyanathan, "Quadratically Constrained Beamforming Robust Against Direction-of-Arrival Mismatch," *IEEE Trans. on Signal Processing*. vol. 55, pp. 4139–4150, Aug. 2007.

[15] C. Y. Chen and P. P. Vaidyanathan, "MIMO Radar Space-Time Adaptive Processing Using Prolate Spheroidal Wave Functions," *IEEE Trans. on Signal Processing*, vol. 56, pp. 623–635, Feb. 2008.

[16] C. Y. Chen and P. P. Vaidyanathan, "MIMO Radar Ambiguity Properties and Optimization Using Frequency-Hopping Waveforms," *IEEE Trans. on Signal Processing,* Dec. 2008.

[17] C. Y. Chen and P. P. Vaidyanathan, "Joint MIMO Radar Waveform and Receiving Filter Optimization," *International Conference on Acoustics, Speech and Signal Processing,* Taipei, Taiwan R.O.C. April 2009.

[18] C. Y. Chen and P. P. Vaidyanathan, "MIMO Radar Waveform Optimization with Prior Information of the Extended Target and Clutter," *IEEE Trans. on Signal Processing,* accepted for future publication.

[19] J. P. Costas, "A Study of a Class of Detection Waveforms Having Nearly Ideal Range-Doppler Ambiguity Properties," *Proc. IEEE,* Vol. 72, pp. 996–1009, Aug. 1984.

[20] H. Cox, "Resolving power and sensitivity to mismatch of optimum array processors," *J. Acoust. Soc. Amer.,* vol. 54, pp. 771–758, 1973.

[21] A. De Maio, S. De Nicola, Y. Huang, S. Zhang and A. Farina, "Code Design to Optimize Radar Detection Performance Under Accuracy and Similarity Constraints," *IEEE Trans. on Signal Processing*, Nov. 2008.

[22] D. DeLong and E. Hofstetter, "On the design of optimum radar waveforms for clutter rejection," *IEEE Trans. on Information Theory,* Volume 13, Issue 3, pp. 454–463, July 1967.

[23] D. Delong and E. Hofstertter, "The design of clutter-resistant radar waveforms with limited dynamic range," *IEEE Trans. on Information Theory,* Volume 15, Issue 3, pp. 376–385, May 1969.

[24] D. Delong and E. Hofstertter, "Design of radar signals and receivers subject to implementation errors," *IEEE Trans. on Information Theory,* Volume 16, Issue 6, pp. 707–711, Nov. 1970.

[25] C. Duofang, C. Baixiao, and Q. Guodong, "Angle estimation using ESPRIT in MIMO radar," *Electronics Letters,* Volume 44, Issue 12, pp. 770–771, June 2008.

[26] M. H. Er and A. Cantoni, "Derivative constraints for broad-band element space antenna array processors," *IEEE Trans. Acoustic, Speech, Sig. Proc.*, vol. ASSP-31, pp. 1378–1393, Dec. 1983.

[27] D. D. Feldman and L. J. Griffiths, "A projection approach for robust adaptive beamforming," *IEEE Trans. Sig. Proc.*, vol. 42, pp. 867–876, April 1994.

[28] E. Fishler, A. Haimovich, R. S. Blum, D. Chizhik, L. J. Cimini, and R. A. Valenzuela, "MIMO Radar: An Idea Whose Time Has Come," *Proc. IEEE Radar Conference,* pp. 71–78, April 2004.

[29] E. Fishler, A. Haimovich, R. S. Blum, L. J. Cimini, D. Chizhik, and R. A. Valenzuela, "Performance of MIMO Radar Systems: Advantages of Angular Diversity," *Proc. 38th IEEE Asilomar Conf. on Signals, Systems, and Computers,* vol. 1, pp. 305–309, Nov. 2004.

[30] E. Fishler, A. Haimovich, R. S. Blum, L. J. Cimini, D. Chizhik, and R. A. Valenzuela, "Spactial Diversity in Radars-Models and Detection Performance," *IEEE Trans. on Signal Processing,* vol. 54, Issue 3, pp. 823–837, March 2006.

[31] O. L. Forst, III, "An algorithm for linearly constrained adaptive processing," *Proc. IEEE*, vol. 60, pp. 926–935, Aug. 1972.

[32] K. W. Forsythe, D. W. Bliss, and G. S. Fawcett, "Multiple-Input Multiple-Output (MIMO) Radar Performance Issues," *Proc. 38th IEEE Asilomar Conf. on Signals, Systems, and Computers,* pp. 310–315, Nov. 2004.

[33] K. W. Forsythe and D. W. Bliss, "Waveform Correlation and Optimization Issues for MIMO Radar," *Proc. 39th IEEE Asilomar Conf. on Signals, Systems, and Computers,* pp. 1306–1310, Nov. 2005.

[34] G. J. Frazer, B. A. Johnsone, Y. I. Abramovich, "Orthogonal Waveform Support in MIMO HF OTH Radars," *International Conference on Waveform Diversity and Design*, pp. 423–427, June 2007.

[35] B. Friedlander, "A Subspace Method for Space Time Adaptive Processing," *IEEE Trans. on Signal Processing*, vol. 53, Issue 1, pp. 74–82, Jan. 2005.

[36] B. Friedlander, "Waveform Design for MIMO Radars," *IEEE Transactions on Aerospace and Electronic Systems,* Vol 43, Issue 3, pp. 1227–1238, July 2007.

[37] D. R. Fuhrmann and G. S. Antonio, "Transmit Beamforming for MIMO Radar Systems Using Partial Signal Correlation," *Proc. 38th IEEE Asilomar Conf. on Signals, Systems, and Computers,* pp. 295–299, Nov. 2004.

[38] D. R. Fuhrmann and G. S. Antonio, "Transmit Beamforming for MIMO Radar Systems using Signal Cross-Correlation," *IEEE Transactions on Aerospace and Electronic Systems,* Volume 44, Issue 1, pp. 171–186, Jan. 2008.

[39] L. C. Godara, "Application of antenna arrays to mobile communications, Part II: Beam-Forming and Direction-of-Arrival Considerations," *Proc. of the IEEE,* Vol. 85, pp. 1195–1245, August 1997.

[40] J. S. Goldstein, I. Si. Reed, and L. L. Scharf, "A Multistage Representation of the Wiener Filter Based on Orthogonal Projections," *IEEE Trans. on Information Theory,* vol. 44, Issue 7, pp. 2943–2959, Nov. 1998.

[41] S. W. Golomb and H. Taylor, "Construction and Properties of Costas Arrays," *Proc. IEEE*, Vol. 72, pp. 1143–1163, Sept. 1984.

[42] N. A. Goodman and J.M. Stiles, "On Clutter Rank Observed by Arbitrary Arrays,"*IEEE Trans. on Signal Processing*, vol. 55, Issue 1, pp. 178–186, Jan. 2007.

[43] J. R. Guerci, J. S. Goldstein, and I. S. Reed, "Optimal and Adaptive Reduced-Rank STAP," Special Section on Space-Time Adaptive Processing, *IEEE Trans. on Aerospace and Electronic Systems,* vol. 36, Issue 2, pp. 647–663, April 2000.

[44] J. R. Guerci, *Space-time adaptive processing*, Artech House, 2003.

[45] A. M. Haimovich and M. Berin, "Eigenanalysis-based space-time adaptive radar: performance analysis," *IEEE Trans. on Aerospace and Electronic Systems,* vol. 33, Issue 4, pp. 1170–1179, Oct. 1997.

[46] A. M. Haimovich, R. S. Blum, and L. J. Cimini, "MIMO Radar with Widely Separated Antennas," *IEEE Signal Processing Magazine,* Volume 25, Issue 1, pp. 116–129, Jan. 2008.

[47] R. Hoctor and S. Kassam, "The unifying role of the coarray in aperture synthesis for coherent and incoherent imaging," *Proceedings of the IEEE,* vol. 78, issue 4, pp. 735–752, April 1990.

[48] R. A. Horn and C. R. Johnson, *Matrix Analysis,* Cambridge 1985.

[49] D. H. Johnson and D. E. Dudgeon, "Array signal processing: concepts and techniques," Prentice Hall, Englewood Cliffs N.J., 1993.

[50] J. P. Keener, *Principles of Applied Mathematics,* Addison-Welsley, 1988.

[51] H. A. Khan, W. Q. Malik, D. J. Edwards, and C. J. Stevens, "Ultra Wideband Multiple-Input Multiple-Output Radar," *IEEE International Radar Conference,* pp. 900–904, May 2005.

[52] H. A. Khan and D. J. Edwards, "Doppler problems in orthogonal MIMO radars," *IEEE International Radar Conference,* pp. 24–27, April 2006.

[53] S. J. Kim; A. Magnani, A. Mutapcic, S. P. Boyd, and Z. Q. Luo, "Robust Beamforming via Worst-Case SINR Maximization," *IEEE Trans. on Signal Processing,* Volume 56, Issue 4, pp. 1539–1547, Aprial 2008.

[54] S. Kirkpatrick, C. D. Gelatt and M. P. Vecchi, "Optimization by Simulated Annealing," *Science,* Vol. 220, no. 4598, pp. 671–680, 1983.

[55] R. Klemm, "Adaptive clutter suppression for airborne phased array radars", *IEE Proc. F,* 130, (1), pp. 125–132, 1983.

[56] R. Klemm, "Adaptive air- and spaceborne MTI under jamming conditions," *IEEE National Radar Conference,* pp. 167–172, April 1993.

[57] R. Klemm, *Principles of Space-Time Adaptive Processing,* IEE, 2002.

[58] R. Kozick and S. Kassam, "Application of the singular value decomposition to aperture synthesis with boundary arrays," *Antennas and Propagation Society International Symposium*, vol. 1, pp. 526–529, June 1991.

[59] H. Krim and M. Viberg, "Two decades of array signal processing research," *IEEE Sig. proc. Mag.*, Vol. 13, pp. 67–94, July 1996.

[60] J. L. Krolik, "The performance of matched-field beamformers with Mediterranean vertical array data," *IEEE Trans. Sig. Proc.*, vol. 44, no. 10, pp. 2605–2611, Oct. 1996.

[61] A. Leshem, O. Naparstek, and A. Nehorai, "Information Theoretic Adaptive Radar Waveform Design for Multiple Extended Targets," *IEEE Journal of Selected Topics in Signal Processing*, Vol. 1, Issue 1, pp. 42–55, June 2007.

[62] N. Levanon and E. Mozeson, *Radar Signals,* Wiley-IEEE Press, 2004.

[63] J. Li, P. Stoica, and Z. Wang, "On robust capon beamforming and diagonal loading," *IEEE Trans. Sig. Proc.*, pp. 1702–1714, July 2003.

[64] J. Li and P. Stoica, ed., *Robust adaptive beamforming*, , John Wiley & Sons, 2006.

[65] J. Li, J. R. Guerci and L. Xu, "Signal Waveform's Optimal Under Restriction Design for Active Sensing," *IEEE Signal Processing Letters*, Sept. 2006.

[66] J. Li and P. Stoica, "MIMO Radar with Colocated Antennas," *IEEE Signal Processing Magzine* Vol. 24, Issue 5, Sept. 2007.

[67] J. Li, P. Stoica, L. Xu, and W. Roberts, "On Parameter Identifiability of MIMO Radar," *IEEE Signal Processing Letters*, Vol. 14, No. 12, pp. 968–971, Dec. 2007.

[68] J. Li, L. Xu, P. Stoica, K. W. Forsythe, and D. Bliss, "Range Compression and Waveform Optimization for MIMO Radar: A CramérVRao Bound Based Study," *IEEE Trans. on Signal Processing*, Volume 56, Issue 1, pp. 218–232, Jan. 2008.

[69] J. Li, P. Stoica and Xiayu Zheng, "Signal Synthesis and Receiver Design for MIMO Radar Imaging," *IEEE Trans. on Signal Processing*, Aug. 2008.

[70] J. Li and P. Stoica, *MIMO Radar Signal Processing*, John Willey & Sons, 2009.

[71] B. Liu, Z. He, J. Zeng, B. Y. Liu, "Polyphase Orthogonal Code Design for MIMO Radar Systems," *International Conference on Radar,* pp. 1–4, Oct. 2006.

[72] B. Liu, Z. He, and Q. He, "Optimization of Orthogonal Discrete Frequency-Coding Waveform Based on Modified Genetic Algorithm for MIMO Radar," *International Conference on Communication, Circuits, and Systems,* pp. 966–970, July 2007.

[73] R. G. Lorenz and S. P. Boyd, "Robust minimum variance beamforming," *IEEE Trans. on Singnal Processing,* Volume 53, pp. 1684–1696, May 2005.

[74] S. V. Maric and E. L. Titlebaum, "A Class of Frequency Hop Codes with Nearly Ideal Characteristics for Use in Multiple-Access Spread-Spectrum Communications and Radar and Sonar Systems," *IEEE Trans. on Communications,* Vol. 40, Issue 9, pp. 1442–1447, Sept. 1992.

[75] V. F. Mecca, D. Ramakrishnan, and J. L. Krolik, "MIMO Radar Space-Time Adaptive Processing for Multipath Clutter Mitigation" *IEEE Workshop on Sensor Array and Multichannel Signal Processing,* pp. 249–253, July 2006.

[76] N. Metropolis, A.W. Rosenbluth, M.N. Rosenbluth, A.H. Teller, and E. Teller. "Equations of State Calculations by Fast Computing Machines," Journal of Chemical Physics, Vol. 21, no. 6, pp. 1087–1092, 1953.

[77] P. S. Naidu, "Sensor array signal processing," CRC Press, Boca Raton, 2001.

[78] A. V. Oppenheim, A. S. Willsky, and S. Hamid, *Signals and Systems,* Prentice Hall, 1996.

[79] A. V. Oppenheim and R. W. Schafer, *Discrete-Time Signal Processing,* Prentice Hall, 1998.

[80] M. Petrich, "On the Number of Orthogonal Signals Which Can be Placed in a WT-Product," *Journal of the Society for Industrial and Applied Mathematics,* Vol. 11, No. 4, pp. 936–940, Dec. 1963.

[81] S. M. Phoong, Y. B. Chang, and C. Y. Chen, "DFT-modulated filterbank transceivers for multipath fading channels," *IEEE Trans. on Signal Processing,* Volume 53, Issue 1, pp. 182–192, Jan. 2005.

[82] S. U. Pillai, H. S. Oh, D. C. Youla, and J. R. Guerci, "Optimal transmit-receiver design in the presence of signal-dependent interference and channel noise," *IEEE Trans. on Information Theory,* Volume 46, Issue 2, pp. 577–584, March 2003.

[83] J. Y. Qu, J. Y. Zhang, and C. Q. Liu, "The Ambiguity Function of MIMO Radar," *International Symposium on Microwave, Antenna, Propagation and EMC Technologies for Wireless Communications*, pp. 265–268, Aug. 2007.

[84] F. Quian and B. D. Van Veen, "Quadratically constrained adaptive beamforming for coherent signal and interference, *IEEE Trans. Sig. Proc.*, vol. 43, pp. 1890–1900, Aug. 1995.

[85] D. J. Rabideau and P. Parker, "Ubiquitous MIMO Multifunction Digital Array Radar," *Proc. 37th IEEE Asilomar Conf. on Signals, Systems, and Computers*, vol. 1, pp. 1057–1064, Nov. 2003.

[86] J. S. Reed, J. D. Mallett, and L. E. Brennan, "Rapid Convergence Rate in Adaptive Arrays," *IEEE Trans. on Aerospace and Electronic Systems*, Vol. 10, No. 6, pp. 853–863, Nov. 1974.

[87] M. A. Richards, *Fundamentals of Radar Signal Processing*, McGraw-Hill, 2005.

[88] F. C. Robey, S. Coutts, D. Weikle, J. C. McHarg, and K. Cuomo, "MIMO Radar Theory and Experimental Results," *Proc. 38th IEEE Asilomar Conf. on Signals, Systems, and Computers*, vol. 1, pp. 300–304, Nov. 2004.

[89] G. San Antonio, D. R. Fuhrmann, and F. C. Robey, "MIMO Radar Ambiguity Functions," *IEEE Journal of Selected Topics in Signal Processing*, Vol. 1, pp. 167–177, Jun. 2007.

[90] S. Serbetli and A. Yener, "Transceiver optimization for multiuser MIMO systems," *IEEE Trans. on Signal Processing*, Volume 52, Issue 1, pp. 214–226, Jan. 2004.

[91] S. Shahbazpanahi, A. B. Gershman, Z.-Q. Luo, and K. M. Wong, "Robust adaptive beamforming for general-rank signal models, " *IEEE Trans. Sig. Proc.*, pp. 2257–2269, Sept. 2003.

[92] M. Skolnik, *Introduction to Radar Systems*, McGraw-Hill, 2001.

[93] D. Slepian, and H. O. Pollak, "Prolate Spheroidal Wave Functions, Fourier Analysis and Uncertainty-III: the dimension of the space of essentially time-and-band-limited signals," *Bell Syst. Tech. J.*, pp. 1295–1336, July 1962.

[94] P. Stoica, J. Li, and Y. Xie, "On Probing Signal Design For MIMO Radar," *IEEE Trans. on Signal Processing* Volume 55, Issue 8, Aug. 2007.

[95] P. Stoica, J. Li and X. Zhu, "Waveform Synthesis for Diversity-Based Transmit Beampattern Design," *IEEE Trans. on Signal Processing*, June 2008.

[96] K. Takao, H. Fujita, and T. Nishi, "An adaptive arrays under directional constraint," *IEEE Trans. Ant. Prop.,* vol. AP-21, pp. 662–669, Sept. 1976.

[97] A. Tkacenko and P. P. Vaidyanathan, "Iterative greedy algorithm for solving the FIR paraunitary approximation problem" *IEEE Trans. on Signal Processing,* Volume 54, Issue 1, pp. 146–160, Jan. 2006.

[98] C. Y. Tseng and L. J. Griffiths, "A unified approach to the design of linear constraints in minimum variance adaptive beamformers," *IEEE Trans. Ant. Prop.,* vol. 40, pp. 1533–1542, Dec. 1992.

[99] B. D. Van Veen, "Minimum variance beamforming with soft response constraints," *IEEE Trans. Sig. Proc.,* vol. 39, pp. 1964–1972, Sept. 1991.

[100] H. L. Van Tree, *Detection, Estimation, and Modulation Theory, Part I,* Wiley-Interscience, 2001.

[101] H. L. Van Trees, *Optimum Array Processing: Part IV of Detection Estimation and Modulation Theory,* New York: Wiley Interscience, 2002.

[102] S. Vorobyov, A. B. Gershman, and Z.-Q. Luo, "Robust adaptive beamforming using worst-case performance optimization: A solution to the signal mismatch problem," *IEEE Trans. Sig. Proc.,* vol. 51, pp. 313–324, Feb. 2003.

[103] A. M. Vural, "A comparative performance study of adaptive array processors," *Proc. IEEE Int. Conf. Acoustic, Speech Sig. Proc.,* May 1977.

[104] J. Ward, "Space-Time Adaptive Processing for Airborne Radar," Technical Report 1015, Lincoln Laboratory, Dec. 1994.

[105] X. Wen, A. Wang, L. Li, and C. Han, "Direct Data Domain Approach to Space-Time Adaptive Signal Processing," *Proc. of the ICARCV,* vol. 3, pp. 2070–2075, Dec. 2004.

[106] M. Willem, *Minimax Theorems,* Birkhäuser Boston, 1997.

[107] S. Q. Wu and J. Y. Zhang, "A new robust beamforming method with antennae calibration errors," *in Proc. IEEE Wireless Commun. Networking Conf.,* vol. 2, New Orleans, LA, pp. 869–872, Sept. 1999.

[108] Y. Yang and R. S. Blum, "MIMO Radar Waveform Design Based on Mutual Information and Minimum Mean-Square Error Estimation," *IEEE Trans. on Aerospace and Electronic Systems*, Vol. 43, Issue 1, pp. 330–343, Jan. 2007.

[109] Y. Yang and R. S. Blum, "Minimax Robust MIMO Radar Waveform Design," *IEEE Journal of Selected Topics in Signal Processing*, Vol. 1, Issue 1, pp. 147–155, June 2007.

[110] J. Yeh, *Real analysis. Theory of measure and integration,* World Scientific Publishing Company, 2006.

[111] Q. Zhang and W. B. Mikhael, "Estimation of the Clutter Rank in the Case of Subarraying for Space-Time Adaptive Processing," *Electronics Letters,* vol. 33, Issue 5, pp. 419–420, 27 Feb. 1997.

[112] http://www.systems.caltech.edu/cyc/amb-fun.htm